1 **Title**

2

3 Locally confined IFNγ production by CD4+ T cells provides niches for murine cytomegalovirus

4 replication in the salivary gland

5

6

7 **Authors**

8

9 Josua Oderbolz[1], Nathan Zangger[1*], Lea Zimmermann[2*], Ioana Sandu[1,3], Jörn Starruß[4], Frederik

10 Graw[2] & Annette Oxenius[1]

11

12 [1]Institute of Microbiology, ETH Zurich, 8093 Zurich, Switzerland

13 [2]BioQuant - Center for Quantitative Biology, Heidelberg University, 69120 Heidelberg, Germany

14 [3]Institute of Molecular Systems Biology, ETH Zurich, 8093 Zurich, Switzerland

15 [4]Center for Information Services and High Performance Computing, TU Dresden, 01062 Dresden,

16 Germany

17

18

19 J.O. and A.O designed the experiments. J.O, N.Z. and L.Z. performed the experiments. J.O., N.Z.

20 and L.Z. analyzed the data. L.Z. and F.G. developed and analyzed the mathematical model, J.S.

21 implemented additional model elements and provided modeling expertise, I.S. provided essential

22 tools. J.O., F.G. and A.O. wrote the manuscript.

23

24 * contributed equally to this work

25

26 All the authors declare no competing interests.

27

28 Correspondence and requests for materials should be addressed to A. O. Institute of Microbiology,

29 ETH Zürich, Vladimir-Prelog-Weg 4, 8093 Zürich, Switzerland. Phone number: +41 44 632 33 17.

30 Email: aoxenius@micro.biol.ethz.ch

31

32

33

34

Abstract

Cytomegalovirus (CMV) has evolved a unique virus-host relationship in the salivary glands (SGs) to sustain prolonged viral replication and hence chances for horizontal transmission. Previous reports have established a decisive role for IFNγ producing CD4⁺ T cells to control murine CMV (MCMV) infection in the SGs; however, micro-anatomical information regarding their mode of action is largely missing. Here, we provide a spatiotemporal analysis of defined antiviral immune actions that eventually culminate in control of lytic MCMV replication in this preferred mucosal niche. CXCR3-mediated guidance of CD4⁺ T cells towards CXCL9 and CXCL10 expressing cells resulted in discrete clusters close to infection foci where they reported TCR engagement and produced IFNγ. Of note, these clusters occasionally contained CD11c⁺ antigen-presenting cells with engulfed virus-associated remnants, most likely apoptotic bodies derived from previously infected cells, enabling antigen presentation to CD4⁺ T cells. The induced IFNγ production within these CD4⁺ T cell accumulations triggered IFNγR signaling in a confined perimeter, thereby inducing local, but not organ-wide protection, and allowing MCMV replication to continue at not yet protected sites. Combining experimental data with a mathematical model of the spatiotemporal dynamics of infection and CD4⁺ T cell dynamics revealed a scenario, in which ultimate MCMV control is achieved through accumulating sites of regionally-confined tissue protection.

Key words: MCMV, salivary glands, CD4⁺ T cells, IFNγ

Introduction

Cytomegalovirus (CMV), a member of the herpesvirus family, is an opportunistic pathogen causing severe clinical outcomes in immunocompromised individuals[1,2]. Owing to many shared similarities with human CMV (HCMV), including the genetic make-up, the high degree of species specificity and the biological characteristics in their natural habitat such as the huge repertoire of immune evasion mechanisms, infection of mice with murine CMV (MCMV) is a robust infection model to study CMV pathogenesis in an animal setting[3,4]. Although primary MCMV infection is controlled in most visceral organs within a few days, the salivary glands (SGs) are a peripheral glandular tissue where lytic viral replication is continuing for several weeks[5]. The sustained high viral loads in the SGs facilitate horizontal transmission via saliva. While control of lytic MCMV replication in most tissues is mediated by MCMV-specific CD8⁺ T cells, this is not the case for the SGs[6–8]. MCMV-encoded MHC class I immune evasion genes (i.e. *m04*, *m06* and *m152*) are particularly potent in

69   avoiding recognition of infected cells by cytotoxic CD8^{+} T cells[9,10], as deletion of these immune

70   evasion genes restores CD8^{+} T cell recognition of MCMV harboring cells, consequently leading to

71   CD8^{+} T cell-mediated immune control of MCMV infection in the SGs[11]. Therefore, under normal

72   circumstances, control of MCMV infection in the SGs completely relies on CD4^{+} T cells that exert

73   their protective effector functions primarily through the secretion of the pro-inflammatory cytokines

74   interferon gamma (IFNγ) and tumor necrosis factor alpha (TNFα)[12,13]. In this regard, we have

75   previously shown that sensing of CD4^{+} T cell-produced IFNγ by non-hematopoietic cells in the

76   SGs is required for eventual control of lytic viral replication[11]. However, it remains unclear how

77   long-lasting productive virus infection is maintained in this peripheral organ in face of marked

78   infiltration of functional MCMV-specific CD4^{+} T cells early upon infection and the prompt

79   generation of tissue-resident memory T cells[14,15]. One important aspect that has so far not received

80   much attention is information about micro-anatomical conditions and constraints in the SGs during

81   MCMV infection. This includes spatial information about infection foci, distribution of infiltrating

82   virus-specific CD4^{+} T cells, sites of antigen recognition and IFNγ production, and the range of IFNγ

83   sensing. In the current study, we used advanced microscopy methods to visualize key

84   components of the antiviral immune response with high spatiotemporal resolution. By combining

85   previous knowledge with our experimental data, we further generated a mathematical model that

86   simulates the CD4^{+} T cell-mediated immune control of MCMV infected SGs. We propose a

87   scenario in which MCMV antigens in the SGs are sensed by virus-specific CD4^{+} T cells only in a

88   delayed and indirect manner, after remnants of previously infected cells had been engulfed by

89   local antigen-presenting cells (APCs). This leads to a locally confined IFNγ secretion, affording

90   protection only in this restricted area. However, non-protected areas of the SGs continue to be

91   permissive for infection and replication, evidenced by long-term maintenance of high viral loads in

92   the SGs. Eventual control occurs if local IFNγ-concentrations are sufficiently effective to allow

93   agglomeration of protected sites, and thus restriction of viral spread. Thereby, accumulation of

94   virus-specific CD4^{+} T cells by APCs potentiates IFNγ concentrations of otherwise limited IFNγ -

95   release by individual CD4^{+} T cells, which enables prolonged protection of local areas and

96   eventually leading to viral control within the tissue.

97

98

99

100

101

102

Results

**Virus-specific CD4$^+$ T cells infiltrate MCMV-infected SGs and show an activated phenotype**

In a first set of experiments, we set out to longitudinally analyze the abundance and phenotype of MCMV-specific CD4$^+$ T cells in the SGs upon MCMV infection. As opposed to SGs of naïve mice, which hardly contain any T cells, MCMV infection leads to a substantial infiltration of CD4$^+$ and CD8$^+$ T cells **(Suppl. Fig. 1a)**. To specifically focus on antigen-specific CD4$^+$ T cells, we employed T cell receptor (TCR) transgenic (tg) CD4$^+$ T cells that specifically recognize the immunodominant MCMV-epitope M25$_{411-425}$ in the context of MHC class II (referred to as M25 CD4$^+$ T cells) in adoptive transfer experiments[16–18]. M25 CD4$^+$ T cells were on a CD45.1 background, allowing the distinction from endogenous CD45.2$^+$ CD4$^+$ T cells **(Suppl. Fig. 1b)**. M25 CD4$^+$ T cells were adoptively transferred one day prior to infection with recombinant green fluorescent protein (GFP)-expressing MCMV (MCMV-GFP), quantified and phenotypically characterized 8, 14 and 30 days post infection (dpi) in the SGs, spleen and lung **(Fig. 1a)**. M25 CD4$^+$ T cells expanded and were present in all organs of infected mice, whereas adoptive transfer (AT) of M25 CD4$^+$ T cells into naïve or latently MCMV infected mice resulted in low M25 CD4$^+$ T cell counts in the SGs **(Suppl. Fig. 1c)**. As expected, systemic infection with MCMV-GFP resulted in increasing viral loads in the SGs over time, but not in the spleen and lung where control happened in the first week **(Suppl. Fig. 1d)**. We detected the highest percentages and total numbers of M25 CD4$^+$ T cells at 8 dpi, followed by a successive reduction over time **(Fig. 1b)**. The continuous reduction of SG-resident M25 CD4$^+$ T cells from day 8 onwards was accompanied by increasing viral titers and stable numbers of endogenous CD4$^+$ T cells **(Suppl. Fig. 1e)**. SG-infiltrating M25 CD4$^+$ T cells displayed an antigen-experienced CD44^{high}CD62L^{low} phenotype and expressed the surface markers LFA-1 (heterodimeric integrin composed of CD11a and CD18) and CD49d, typical features that had been reported previously for MCMV-specific CD4$^+$ T cells **(Fig. 1c)**[19–21]. Most of the endogenous CD4$^+$ T cells were also CD44^{high}LFA-1$^+$CD49d$^+$, suggesting that the majority of them were also MCMV-specific. Moreover, a considerable fraction of SG-located M25 CD4$^+$ T cells expressed the surface markers CD69 and PD-1 8 dpi, associated with an activated status **(Suppl. Fig. 1f)**. Interestingly, CXCR3 (being associated with a Th1 phenotype) was almost completely absent in SG- and lung-residing CD4$^+$ T cells compared to those in spleen, submandibular lymph node and blood **(Fig. 1d, suppl. Fig. 1g)**[22,23].

Next, we asked the question whether M25 CD4$^+$ T cells sense their cognate antigen in the SGs. To this end, M25 CD4$^+$ T cells harboring a Nur77GFP reporter gene were used (referred to as M25xNur77GFP CD4$^+$ T cells) in which TCR engagement via cognate antigen results in GFP

138   expression[24,25]. M25xNur77GFP CD4^{+} T cells were adoptively transferred one day prior to MCMV-

139   GFP infection and GFP expression in the transferred cells was analyzed 8 and 14 dpi in SGs,

140   spleen and lung. Despite huge differences in viral loads between SGs, spleen and lung, we

141   observed large frequencies of Nur77GFP positive M25 CD4^{+} T cells at 8 dpi with a subsequent

142   decrease at 14 dpi in all organs **(Fig. 1e, suppl. Fig. 1d).** These data suggest that viral loads are

143   not a good proxy for the amount of antigen sensed by M25-specific CD4^{+} T cells. Similar results

144   were obtained when a recombinant mcherry-expressing MCMV strain (MCMV-3DR) was used for

145   the infection, which caused higher viral loads in the SGs within the first two weeks after infection

146   compared to the MCMV-GFP mutant **(Suppl. Fig. 1h and i).** Taken together, these results indicate

147   that SG-infiltrating M25 CD4^{+} T cells have an activated, antigen-experienced phenotype with

148   substantial exposure to cognate antigen during early stage of MCMV infection in the SGs.

149

150

151

152

153

154

155

156

157

158

159

160

161

162

163

164

165

166

167

168

169

170

171

Figure 1
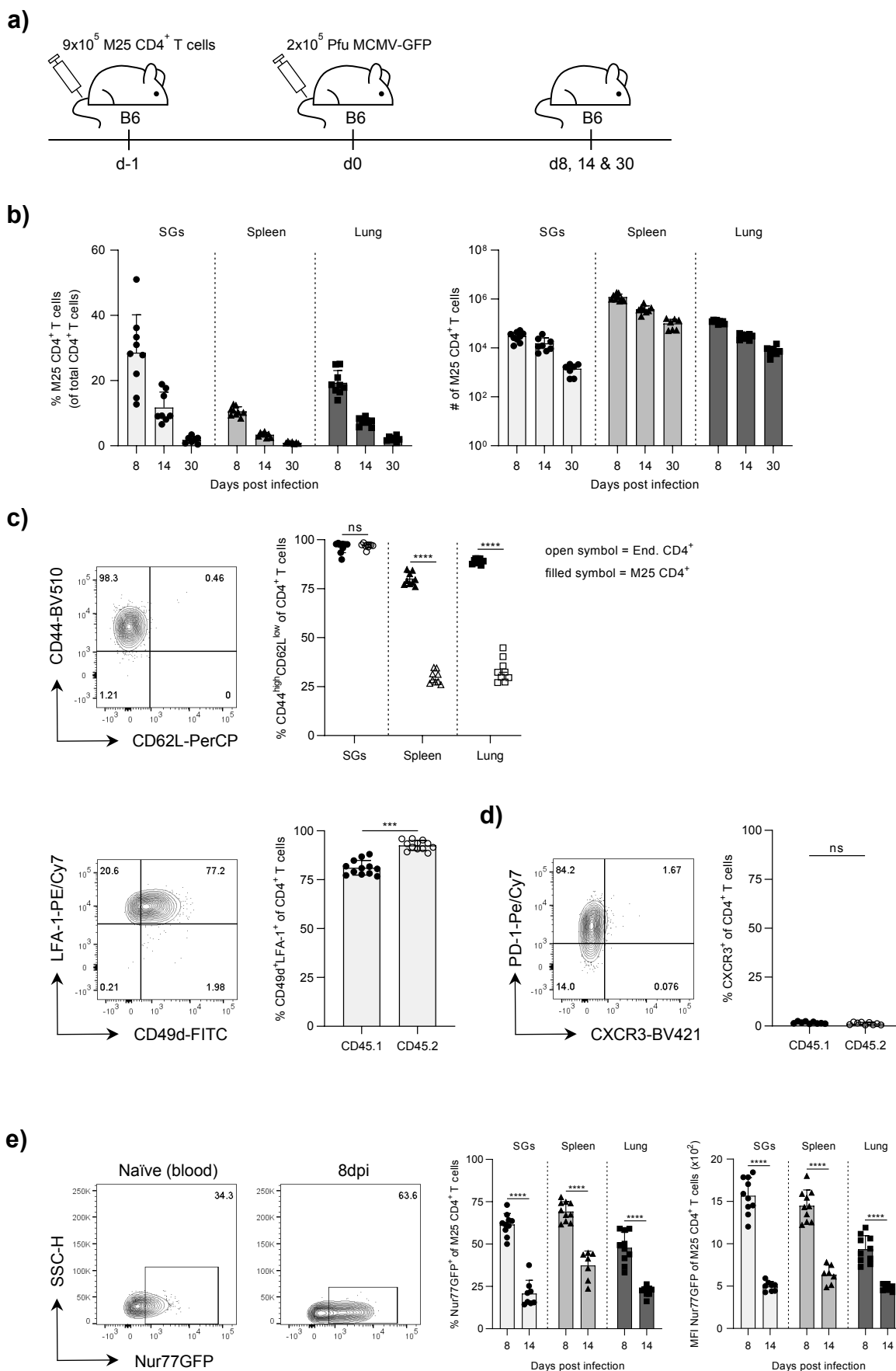
173 **Figure 1**: **Kinetics and phenotypic characterization of M25 CD4$^+$ T cells. a)** Experimental
174 approach. $9*10^5$ MACS purified M25 CD4$^+$ T cells were adoptively transferred into naïve WT B6
175 mice one day prior MCMV-GFP infection and analyzed in various organs at indicated time points.
176 **b)** Percentage and total number of M25 CD4$^+$ T cells in the SGs, spleens & lungs at indicated time
177 points. **c)** Upper row: Representative flow cytometry contour plot of CD44^{high}CD62L^{low} M25 CD4$^+$
178 T cells in the SGs (left) and percentage of CD44^{high}CD62L^{low} CD4$^+$ T cells in the SGs, spleens and
179 lungs (right). Lower row: Representative flow cytometry contour plot of CD49d$^+$LFA-1$^+$ M25 CD4$^+$
180 T cells (left) and percentage of CD49d$^+$LFA-1$^+$ CD4$^+$ T cells in the SGs (right). **d)** Representative
181 flow cytometry contour plot of CXCR3$^+$ M25 CD4$^+$ T cells in the SGs (left) and percentage of
182 CXCR3$^+$ CD4$^+$ T cells in the SGs (right). **e)** Representative flow cytometry contour plot of
183 Nur77GFP$^+$ M25 CD4$^+$ T cells in the blood of naïve M25xNur77GFP mice and in MCMV-GFP
184 infected SGs (left). Percentage of Nur77GFP$^+$ M25 CD4$^+$ T cells and MFI of Nur77GFP on M25
185 CD4$^+$ T cells in the SGs, spleens and lungs (right). **c and d)** Representative flow cytometry contour
186 plots and analyses from 8 dpi. Filled symbol = CD45.1$^+$ M25 CD4$^+$ T cells, open symbol = CD45.2$^+$
187 endogenous CD4$^+$ T cells. Data in **b – e** are shown as mean + SD of n = 7 – 12 mice pooled from
188 two independent experiments. Each symbol represents an individual mouse. Statistical
189 significance was determined using single **(c: lower row and d)** or multiple **(c: upper row and e)**
190 unpaired two-tailed t test. *P<0.05, ***P<0.001, ****P<0.0001, ns = not significant.
191
192
193
194
195
196
197
198
199
200
201
202
203
204
205
206
207

208 ***In vivo* M25 peptide challenge leads to pronounced IFNγ production by SG-localized M25**
209 **CD4+ T cells in a TCR-dependent manner**

210

211 Previous studies investigated the pro-inflammatory cytokine secretion profile of MCMV-specific
212 CD4+ T cells upon *ex vivo* exposure to a defined pool of peptides or lysate of MCMV-infected
213 cells[16,18,19]. To evaluate the potential of SG-residing M25 CD4+ T cells to produce the pro-
214 inflammatory cytokines IFNγ and TNFα, we systemically challenged mice that had received M25
215 CD4+ T cells with the cognate M25 peptide at day 8 or 21 post MCMV infection and harvested the
216 SGs and spleen three hours later **(Fig. 2a)**[20]**.** The majority of M25 CD4+ T cells in both organs
217 upregulated the early T cell activation marker CD69 upon *in vivo* M25 peptide administration
218 compared to the DMSO control injection **(Fig. 2b).** Moreover, a considerable proportion of M25
219 CD4+ T cell expressed IFNγ and a surprisingly low percentage co-expressed IFNγ and TNFα in
220 the SGs **(Fig. 2c)**. Notably, comparable frequencies of M25 CD4+ T cells upregulated CD69 and
221 produced IFNγ upon *in vivo* M25 peptide challenge at 8 and 21 dpi **(Fig. 2d).** Next, we validated
222 that IFNγ production was due to TCR engagement. We used M25xNur77GFP CD4+ T cells for the
223 AT, followed by MCMV infection and M25 peptide challenge at 8 dpi. Over 90% of M25 CD4+ T
224 cells in the SGs and spleen turned Nur77GFP positive upon M25 peptide administration **(Fig. 2e).**
225 Furthermore, IFNγ+ cells were all Nur77GFP+, revealing that indeed the IFNγ production is the
226 result of TCR-based antigen recognition and downstream signaling **(Fig. 2f)**. Of note, the reduced
227 percentage of Nur77GFP+ M25 CD4+ T cells at day 8 post MCMV infection in the SGs and spleen
228 compared to results shown in Figure 1 **(Fig. 1e and suppl. Fig. 1i)** is due to the paraformaldehyde
229 (PFA)-based fixation procedure. These data show that M25 CD4+ T cells can be locally triggered
230 in the SGs after systemic administration of the cognate peptide, and that 10 - 40% of M25 CD4+
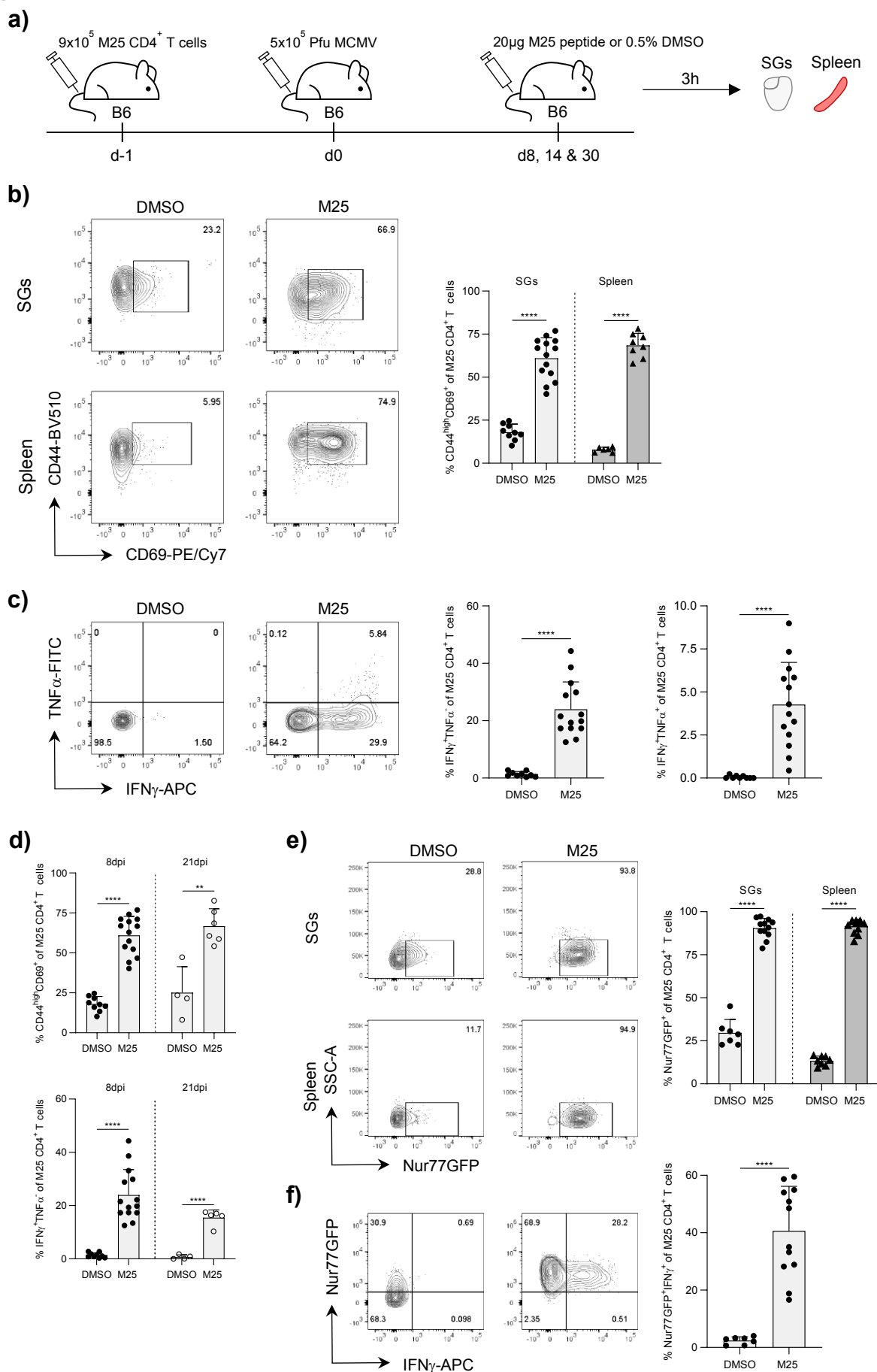231 T cells produce IFNγ in a TCR-dependent manner.

232
233
234
235
236
237
238
239
240
241

Figure 2

a)

b)

c)

d)

e)

f)

242

243 **Figure 2: IFNγ production by SG-localized M25 CD4$^+$ T cells. a)** Experimental approach. 10^6

244 MACS purified M25 (Nur77GFP) CD4$^+$ T cells were adoptively transferred into naïve WT B6 mice

245 one day prior MCMV infection and subsequently challenged for 3h with i.v. administered cognate

246 M25 peptide or 0.5% DMSO as control at day 8 or 21 post MCMV infection. **b)** Representative

247 flow cytometry contour plots (left) and quantification (right) of early activated CD44^{high}CD69$^+$ M25

248 CD4$^+$ T cells in the SGs and spleens 3h post M25 peptide or DMSO administration at day 8 post

249 MCMV infection. **c)** Representative flow cytometry contour plots (left) and quantification (right) of

250 IFNγ and TNFα expression levels by M25 CD4$^+$ T cells in the SGs 3h post M25 peptide or DMSO

251 administration at day 8 post MCMV infection. **d)** Percentage of CD44^{high}CD69$^+$ (top) and IFNγ^+

252 (bottom) M25 CD4$^+$ T cells 3h post M25 peptide or DMSO administration at day 8 and 21 post

253 MCMV infection. **e)** Representative flow cytometry contour plots (left) and quantification (right) of

254 Nur77GFP$^+$ M25 CD4$^+$ T cells in the SGs and spleens 3h post M25 peptide or DMSO challenge

255 at day 8 post MCMV infection. **f)** Representative flow cytometry contour plots (left) and

256 quantification (right) of Nur77GFP$^+$IFNγ^+ M25 CD4$^+$ T cells in the SGs 3h post M25 or DMSO

257 challenge at day 8 post MCVM infection. Data in **b – f** are shown as mean + SD of n = 4 – 14 mice

258 pooled from two (b: spleen and d: 21dpi) or three independent experiments. Each symbol

259 represents an individual mouse. Statistical significance was determined using single **(c and f)** or

260 multiple **(b, d and e)** unpaired two-tailed t test. **P<0.01, ****P<0.0001.

261

262

263

264

265

266

267

268

269

270

271

272

273

274

275

276

277

278 **Entire cross section analysis of acutely MCMV-infected SGs reveals micro-anatomical**

279 **localization of early infiltrating CD4+ T cells**

280

281 Next, we studied the micro-anatomical localization of M25 and endogenous CD4+ T cells in acutely

282 MCMV infected SGs by adding another layer of information and resolution. For this purpose, we

283 transferred traceable RFP-expressing M25 CD4+ T cells (referred to as M25xRFP CD4+ T cells)

284 and subsequently infected mice with MCMV-GFP. Eight days post MCMV-GFP infection, we

285 harvested the SGs and performed whole slide imaging (WSI), followed by in-depth spatial relation

286 studies between SG-infiltrating CD4+ T cells and large actively infected (GFP+) cells (sites of

287 infectious virus production) using the quantitative image analysis software HALO **(Fig. 3a).** To

288 prevent tissue damage, we carefully dissected, cut and imaged the tightly connected

289 submandibular -and sublingual glands (SMGs and SLGs, respectively) together. Differences in

290 structural features enabled the separation of the SGs into SMGs and SLGs **(Suppl. Fig. 2a).** By

291 applying four-color entire cross section (ECS) analyses, we simultaneously visualized

292 endogenous CD4+ and M25 CD4+ T cells, along with sites of viral replication. M25 CD4+ T cells

293 were readily identified by their co-expression of cytoplasmic RFP and the cell membrane CD4

294 marker, whereas endogenous CD4+ T cells were only positive for the latter. Sites of viral replication

295 were identified by their "Owl's eye" appearance of well-known inclusion bodies (enlarged cells that

296 are bright for the virus-encoded fluorescent reporter) **(Fig. 3b)**[26]. First, we analyzed total numbers

297 of M25 CD4+ T cells in the SMGs and SLGs and detected the majority of M25 CD4+ T cells in the

298 SMGs **(Fig. 3c)**. However, this was not surprising since the SMGs encompass an approximately

299 six times larger surface area than the SLGs **(Suppl. Fig. 2b)**. Nevertheless, normalizing for the

300 surface area also showed a higher density of M25 CD4+ T cells in the SMGs **(Fig. 3c)**. Next, we

301 quantified the sites of viral replication across the sections and observed considerable

302 heterogeneity, ranging from one to twelve sites of viral replication per SMG cross section **(Fig.**

303 **3d)**. As CD4+ T cell density and number of infected cells were higher in the SMGs, we focused

304 the ensuing spatial analyses to this part of the SGs. In this regard, we quantified distances

305 between sites of viral replication and endogenous or M25 CD4+ T cells by extracting data of

306 interest from raw images and employing nearest neighbor analysis. Based on the distribution of

307 measured distances, we quantified the frequencies of endogenous CD4+ and M25 CD4+ T cells

308 residing within a defined radius from the next site of viral replication **(Suppl. Fig. 2c).** Proximity

309 analyses revealed that most of the endogenous CD4+ and M25 CD4+ T cells were located 600 μm

310 and more away from the next site of viral replication. However, the percentage of M25 CD4+ T

311 cells in relative close proximity to these infection foci (≤ 300 μm) was significantly higher than the

312 ones of the endogenous CD4+ T cell compartment **(Fig. 3e).** Given the considerable differences

313   in numbers of viral replication sites per SMG section and the rather random distribution of M25

314   CD4$^+$ T cells at 8 dpi, we expected a correlation between the proportion of M25 CD4$^+$ T cells

315   residing within a radius of 300 μm to the nearest site of viral replication and the total counts of

316   sites of viral replication per ECS. Indeed, we discovered a tendency that the number of infection

317   foci strongly influenced this frequency **(Fig. 3f)**. However, a few tissue sections showed signs of

318   virus-associated T cell clustering, noticeable by the high frequency of M25 CD4$^+$ T cells within 300

319   μm to a relatively low number of sites of viral replication **(Fig. 3f & g).** We further quantified the

320   Euclidean distance between two closest endogenous CD4$^+$ and M25 CD4$^+$ T cells and observed

321   slightly shorter distances between M25$^+$ CD4$^+$ T cells compared to the endogenous CD4$^+$ T cells

322   **(Fig. 3e)**. Generally, both CD4$^+$ T cell populations appeared to be distributed quite randomly and

323   rarely showed signs of accumulation close to infection foci. Therefore, the variation in the average

324   distances between two M25 CD4$^+$ T cells is mostly due to differences in cell densities, thus

325   indicating that the total number of M25 CD4$^+$ T cells per tissue section has a stronger impact on

326   the distances between these cells than distinct accumulation characteristics **(Fig. 3h).** Finally, *in*

327   *vivo* short-term intravenous (i.v.) antibody labeling revealed that M25 CD4$^+$ T cells do not reside

328   in close proximity to the circulation **(Suppl. Fig. 2d).** In summary, these results indicate that M25

329   and endogenous CD4$^+$ T cells are not preferentially found in close proximity to sites of infection,

330   but rather distribute randomly across the tissue of acutely MCMV-GFP infected SGs.

331

332

333
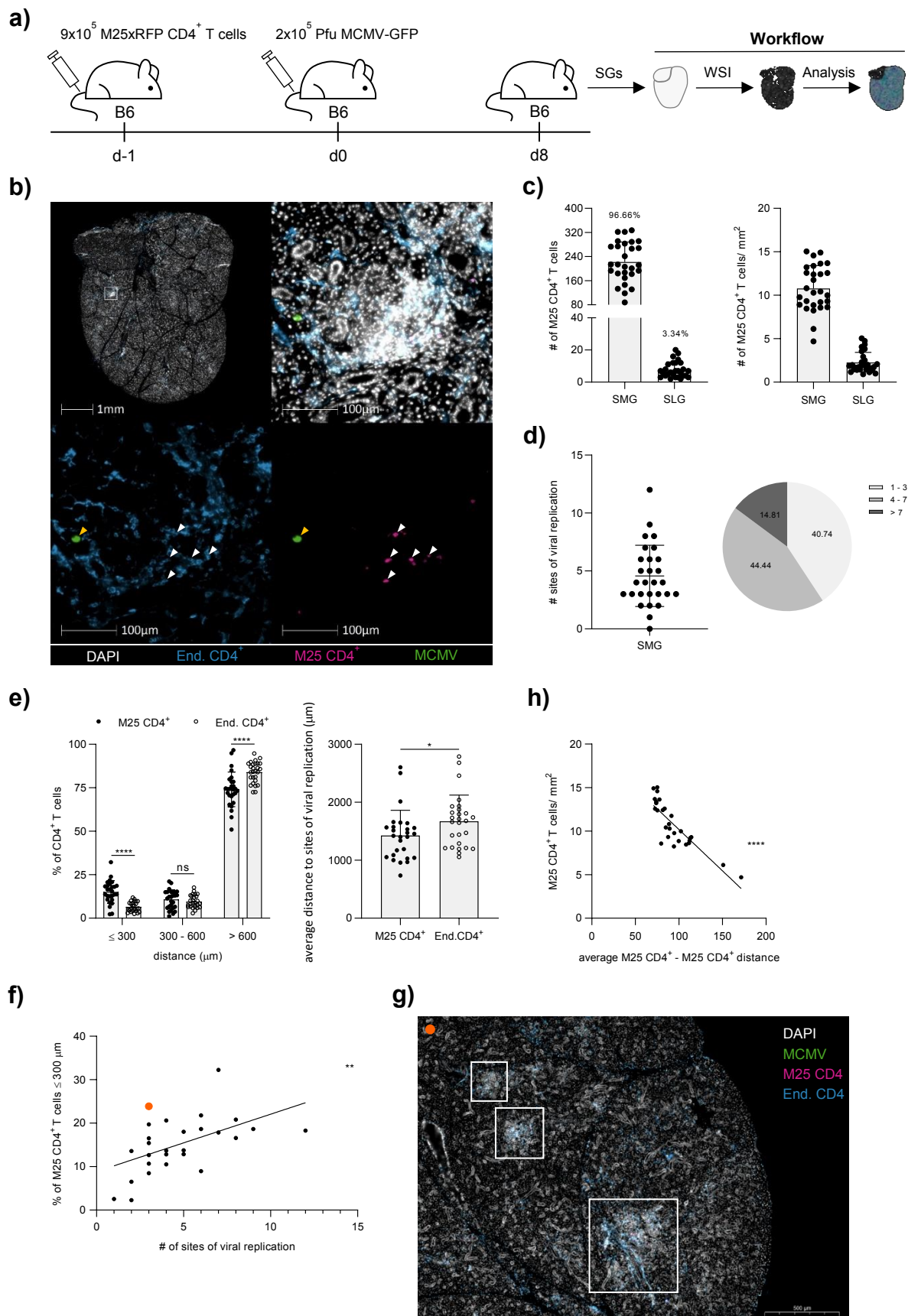
334

335

336

337

338

339

340

341

342

343

344

345

346

Figure 3

348 **Figure 3. Spatial localization of endogenous CD4$^+$ and M25 CD4$^+$ T cells in acutely MCMV**

349 **infected SGs. a)** Experimental approach. 9*10^5 MACS purified RFP traceable M25 CD4$^+$ T cells

350 were adoptively transferred into naïve WT B6 mice one day prior MCMV-GFP infection. 8 days

351 post MCMV-GFP infection, 10μm thin tissue sections of the SGs were sliced and subjected to

352 whole slide imaging (WSI), followed by quantitative image analysis using the HALO$^®$ software. **b)**

353 Example of an entire cross section (ECS) of the right SG lobe (upper left) with indicated magnified

354 region (upper right). Endogenous CD4$^+$ T cells are shown in cyan (bottom left), M25 CD4$^+$ T cells

355 are shown in magenta (bottom right, white arrowheads), and a site of viral replication is shown in

356 green (bottom, yellow arrowhead). **c)** Total M25 CD4$^+$ T cell counts (left) and cell density (right) in

357 the SMG and SLG. **d)** Number of sites of viral replications in the SMG (left) with the percental

358 distribution (pie chart, right). **e)** Percentage of endogenous CD4$^+$ and M25 CD4$^+$ T cells located

359 within a defined distance to the nearest infection foci (left) and summarized average distances of

360 the endogenous CD4$^+$ and M25 CD4$^+$ T cells to these sites (right). **f)** Correlation between the

361 number of infection foci per ECS and the percentages of M25 CD4$^+$ T cells located within 300 μm

362 away from the nearest infection foci. **g)** Cutout of an ECS of a B6 mouse-derived SG 8 days post

363 MCMV-GFP infection. White frames highlight sites of T cell accumulations close to sites of active

364 viral replication. Data point represented by the orange dot in **f)** corresponds to the cutout of the

365 ECS in **g). h)** Correlation between the cell densities of M25 CD4$^+$ T cells and the average in

366 between distances per ECS. Data in **c – f & h** are shown as mean + SD of n = 5 mice (2 -11 ECS

367 per SG, total 28 ECS) pooled from two independent experiments. Each dot represents an

368 individual ECS. Total 275'359 endogenous CD4$^+$ and 6'218 M25 CD4$^+$ T cells were analyzed.

369 Statistical significance was determined using single (**e, right**) multiple (**e, left**) unpaired two-tailed

370 t test, or two-tailed Pearson correlation (**f & h**). **P<0.01, ****P<0.0001, ns = not significant. Scale

371 bar in **b** = 100 μm and in **g** = 500 μm. SMG = Submandibular gland, SLG = Sublingual gland.

372

373

374

375

376

377

378

379

380

381

382

**CD4+ T cells represent the major cellular source of IFNγ production in MCMV infected SGs**

The pro-inflammatory cytokine IFNγ was previously shown to be a crucial component of the antiviral control mechanism in MCMV infected SGs[12]. Therefore, we evaluated next which immune cell type present in the MCMV-infected SGs would preferentially produce the pivotal cytokine IFNγ. To this end, we made use of the IFNγ reporter mouse GREAT, which expresses the enhanced yellow fluorescence protein (EYFP) under the control of the IFNγ promoter[27]. In doing so, we investigated cell-specific and spatial IFNγ production in MCMV-3DR infected SGs. We infected GREAT mice with MCMV-3DR and determined which cell types were EYFP+ (i.e. IFNγ producing) at 14 dpi. Compared to naïve GREAT mice, we observed significantly elevated EYFP signal levels upon MCMV-3DR infection **(Fig. 4a, suppl. Fig. 3a).** We then characterized the cell types within the EYFP positive cell fraction and identified CD3+ cells as the primary cellular source of IFNγ production in MCMV infected SGs. A minor proportion was assigned to NK1.1+ natural killer (NK) cells **(Fig. 4b, suppl. 3b)**. Further classification of the EYFP+CD3+ cell population revealed that ¾ of these cells were CD4+ T cells **(Fig. 4c, suppl. Fig. 3c).** Additionally, we measured EYFP signal intensities in total CD4+, CD8+ and NK1.1+ cells. Again, CD4+ T cells showed the highest percentage of EYFP+ cells, followed by NK cells and CD8+ T cells **(Fig. 4d, suppl. Fig. 3d).** Next, we aimed to study IFNγ producing cells *in situ* by applying confocal microscopy. We therefore performed microscopic analyses of MCMV-3DR infected SGs to reveal spatial relations between IFNγ-producing CD4+ and CD8+ T cells and sites of viral replication. We simultaneously recorded CD4+, CD8+ and EYFP+ cells in various field of views (FOVs) of MCMV-3DR infected SGs containing at least one site of viral replication, and attributed each EYFP+ cell to its corresponding cell type **(Fig. 4e & f).** In line with the flow cytometry analyses, CD4+ T cells were the major cellular source of IFNγ production **(Fig. 4g)**. Moreover, spatial analyses revealed that CD4+ T cells tended to accumulate in dense clusters at 14 dpi, whereas CD8+ T cells showed a more dispersed distribution, despite higher abundance **(Suppl. Fig. 3e)**. Of note, additional microscopic analyses of MCMV-3DR-infected SGs from Nur77GFP mice further identified dense CD4+ T cell clusters in vicinity to infectious virus production. This implies that accumulations of CD4+ T cells close to sites of viral replication represent primary sites of antigen recognition, identifiable by a remarkable fraction of GFP expressing CD4+ T cells. **(Fig. 4h & suppl. Fig. 3f & g)**. Interestingly, we sometimes detected small structures containing the mcherry signal from the MCMV-3DR strain within these CD4+ T cell accumulations, congruent with a high abundance of mainly EYFP+ IFNγ producing CD4+ T cells **(Fig. 4i).** In this regard, further microscopic analyses identified CD11c+ APC as primary cell type harboring these small mcherry+ remnants of MCMV-infected cells,

417   whereas active lytic viral replication was predominantly found within E-Cadherin+ epithelial cells

418   **(Suppl. Fig. 4a & b)**. These results strongly confirm previous findings from our lab, that the

419   presentation of phagocytosed remnants (presumably apoptotic bodies containing viral proteins)

420   from previously infected cells by CD11c+ APCs lead to local CD4+ T cell activation[11]. Thus, CD4+

421   T cells rather recognize apoptotic cell-derived viral structures presented by APCs than directly

422   infected epithelial cells. Taken together, these findings show that CD4+ T cells are the major

423   cellular source of IFNγ production in MCMV-infected SGs, and that IFNγ-producing CD4+ T cells

424   are found in dense clusters at 14 dpi, usually in close proximity to sites of active viral replication.

425   Furthermore, local TCR triggering and IFNγ production is often associated with the presence of

426   CD11c+ cells containing mcherry+ inclusions - most likely remnants from infected cells, serving as

427   antigen source for the activation of CD4+ T cells.

428

429

430

431

432

433

434

435

436

437

438

439

440

441

442

443

444

445

446

447

448

449

450

451

Figure 4
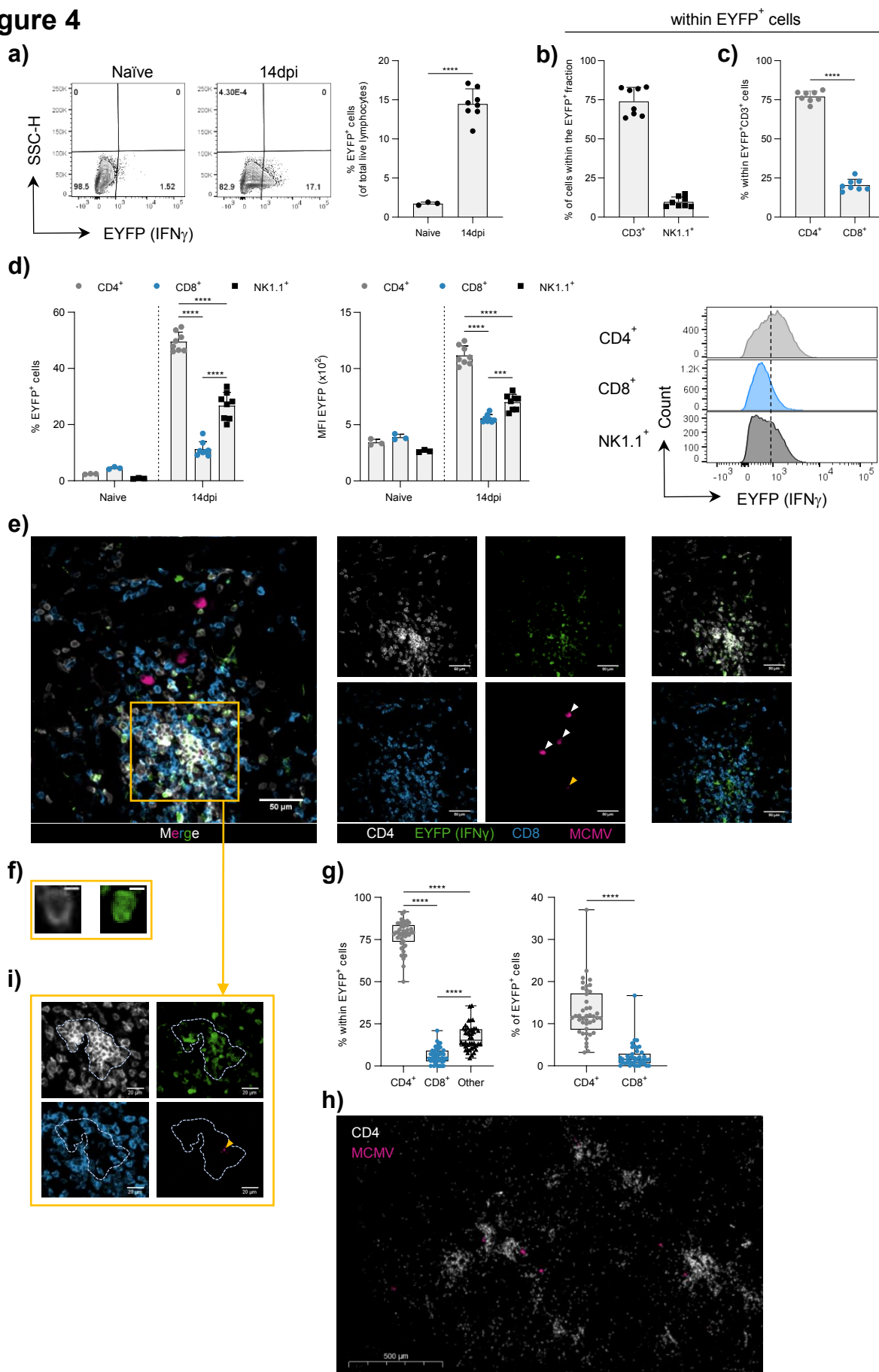
Figure 4. IFNγ production by CD4$^+$ T cells in MCMV infected SGs. a) Representative flow cytometry contour plots of naïve and MCMV-3DR infected Great mice (left) and percentage of total EYFP$^+$ cells (right), **b)** percentage of CD3$^+$ and NK1.1$^+$ cells within EYFP$^+$ cells, and **c)** percentage of CD4$^+$ and CD8$^+$ T cells within CD3$^+$EYFP$^+$ cells. **d)** Percentage of EYFP$^+$ cells within the indicated cell types (left) and the MFI of the EYFP signal (middle). Representative histograms of the EYFP expression profile in the indicated cell types 14dpi (right). Dashed line defines threshold for positive signal. **e)** Example of a four color FOV of a Great mouse-derived SG 14 days post MCMV-3DR infection (left). Single color channel images (middle), merged two color CD4/EYFP (right, upper row) and CD8/EYFP (right, lower row) images. **f)** Magnified IFNγ$^+$ CD4$^+$ T cell (cytosolic EYFP and cell membrane CD4 signal). **g)** Quantification of microscopic analyses. Percentage of cell types within total counted EYFP$^+$ cells (left) and the frequency of EYFP$^+$ cells within CD4$^+$ and CD8$^+$ T cells (right) per FOV of MCMV-3DR infected SGs 14dpi. **h)** Cutout of an ECS of a Nur77GFP mouse-derived SG 14 days post MCMV-3DR infection. **i)** Magnified region split in four single color channel images. Dashed line demarcates dense accumulation of preferentially IFNγ$^+$ CD4$^+$ T cells in close proximity to faint mcherrry signal (yellow arrowhead). Data in **a – d** and are shown as mean ± SD of n = 3 naïve and n = 8 infected Great mice pooled from 2 independent experiments. Data in **g** are shown as box and whiskers showing all points from Min. to Max. (n = 42 FOVs with n > 6 per mice) of n = 3 mice from one independent experiment. Each symbol in **a – d** represents one individual mouse and in **g** one individual FOV. Statistical significance was determined using single unpaired two-tailed t test **(a – c** and **g: right)**, or 2-way Anova with post hoc Tukey's multiple comparisons test **(d and g: left)**. ***P<0.001, ****P<0.0001. Scale bar in **e** = 50 µm, in **f** = 5 µm, in **h** = 100 µm and in **i** = 20 µm. White and yellow arrowheads in **e** and **i** indicate infection foci and presumably cargo/ remnants of infected cells, respectively. FOV = Field of view.

3D confocal imaging provides a new level of information regarding the CD4+ T cell - MCMV interaction

Classical FOV analyses along with the WSI approach allowed us to investigate antiviral immune responses in MCMV infected SGs in two dimensions; however, organs are intrinsically built up in three dimensions. Moreover, the considerable heterogeneity of number of sites of viral replication, together with their anatomical location and complex interrelation with CD4+ T cells, required a more profound three-dimensional (3D) examination of the tissue sample. Furthermore, dense clusters of CD4+ T cells surrounding virus-associated small structures needed to be confirmed and explored in more detail. For this purpose, we elaborated a clearing-based 3D confocal microscopy pipeline for 200 µm thick tissue sections **(Fig. 5a)** [28,29]. In doing so, PFA fixed MCMV-3DR infected SGs were first embedded in agarose and subsequently sliced at appropriate thickness using a vibrating microtome. Tissue sections were then stained, optically cleared, and imaged using an inverted confocal microscope. Finally, 3D reconstructions composed of sequentially acquired 2D-stacked images were processed and visualized, followed by in-depth spatial analyses. As proof, tissue clearing with the histodenz-based refractive index (RI) matching solution (RIMS) substantially increased imaging depth up to 200 µm, allowing the precise identification of several sites of viral replication and the truthful evaluation of CD4+ T cell counts **(Fig. 5b & Suppl. Video 1).** Furthermore, and in line with observations from the 2D images, specific FOVs at different z-planes revealed the emergence and disappearance of accumulating CD4+ T cells around small virus-associated structures, whereas closely situated large infection foci seemed to be ignored **(Fig. 5c).** Nearest neighbor analysis further confirmed the observation that a relevant number of CD4+ T cells are in close proximity to many of these small mcherry+ remnants, which presumably represent apoptotic bodies released from previously infected cells **(Fig. 5d, Suppl. Fig. 4c & Video 2).** Image segmentation of actively MCMV-3DR-infected cells and small virus-associated structures derived from infected cells revealed different morphological appearances (**Fig. 5e & suppl. Fig. 4c**). As previously indicated **(Suppl. Fig. 4a & b),** small mcherry+ virus-associated remnants were frequently found within CD11c+ APCs (≈ 30%), most likely as a result of phagocytic activity **(Suppl. Video 3)**. In contrast, large actively infected cells were only assigned to E-Cadherin+ epithelial cells, again confirming previous knowledge that acinar glandular epithelial cells represent the preferred cell type in the SGs for infectious virus production **(Fig. 5f & g)**. Importantly, unassigned mcherry signals of small volumes might be cell-free (not yet phagocytosed) or found within other cell types, for instance in CD11b+ cells **(Suppl. Fig. 4d)** In summary, 3D confocal imaging confirmed that dense accumulations of CD4+ T cells

522   are often associated with APCs that harbor cargo from previously virus-infected cells, likely

523   remnants or apoptotic bodies **(Suppl. Video 4)**.

524

525

526

527

528

529

530

531

532

533

534

535

536

537

538

539

540

541

542

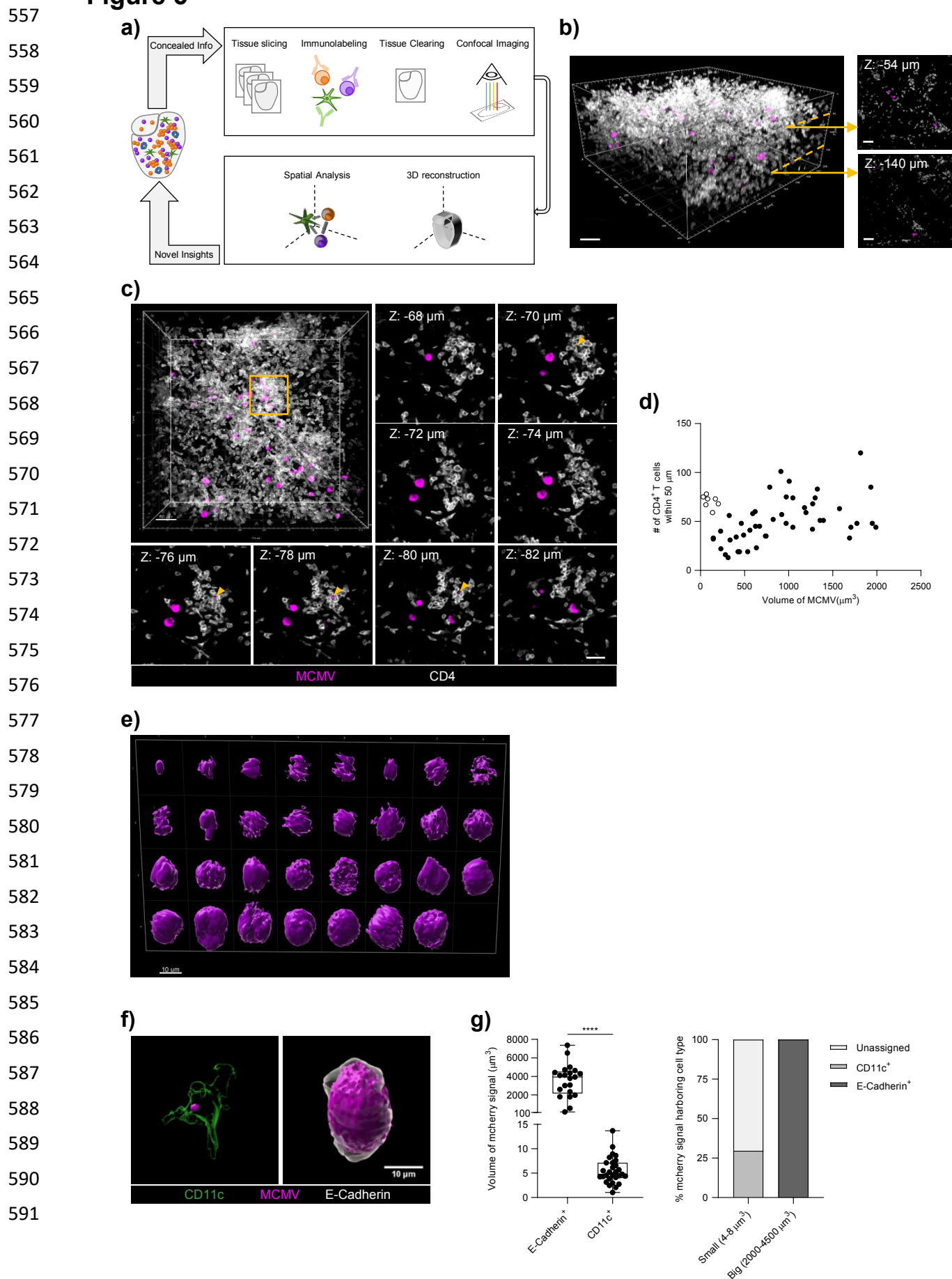543

544

545

546

547

548

549

550

551

552

553

554

555

556

Figure 5

557
558
559
560
561
562
563
564
565
566
567
568
569
570
571
572
573
574
575
576
577
578
579
580
581
582
583
584
585
586
587
588
589
590
591

a) Concealed Info — Tissue slicing, Immunolabeling, Tissue Clearing, Confocal Imaging; Spatial Analysis, 3D reconstruction; Novel Insights

b) Z: -54 μm; Z: -140 μm

c) Z: -68 μm; Z: -70 μm; Z: -72 μm; Z: -74 μm; Z: -76 μm; Z: -78 μm; Z: -80 μm; Z: -82 μm; MCMV; CD4

d) # of CD4+ T cells within 50 μm; Volume of MCMV(μm^3)

e) 10 um

f) CD11c; MCMV; E-Cadherin; 10 μm

g) Volume of mcherry signal (μm^3); ****; E-Cadherin+; CD11c+; % mcherry signal harboring cell type; Unassigned; CD11c+; E-Cadherin+; Small (4-8 μm^3); Big (2000-4500 μm^3)

592   **Figure 5. 3D Imaging of MCMV-infected SGs. a)** Schematic overview of our 3D imaging pipeline.

593   **b)** Confocal imaging depth of an optically cleared SG sample. **c)** 3D global view (450 μm x 450

594   μm x 200 μm) of a 200 μm thick SG section (left, top) with magnified 2D sections at indicated z-

595   positions from the outlined FOV (yellow frame). Yellow arrowheads show MCMV-3DR-associated

596   faint mcherry signal. **d)** MCMV-3DR volume plotted against the number of CD4$^+$ T cells within 50

597   μm to each mcherry signal. Dashed circle demarcates potential remnants of previously MCMV-

598   3DR infected cells with high abundance of CD4$^+$ T cells (open dots) **e)** Morphological variability of

599   MCMV-3DR-associated mcherry signals from FOV represented in **c**, ordered by volume from top

600   left to down right. **f)** 3D reconstructions of MCMV-3DR-associated mcherry signal within a CD11c$^+$

601   and an E-Cadherin$^+$ cell 14 dpi. **g)** Volume of MCMV-3DR-associated mcherry signal in E-

602   Cadherin$^+$ and CD11c$^+$ cells 14 dpi (left). Percentage of E-Cadherin$^+$ and CD11c$^+$ cells harboring

603   small (4-8 μm^3) and big (2000-4500 μm^3) volumes of MCMV-3DR-associated mcherry signal 14

604   dpi (right). Data in **d** are shown as dots of n = 54 MCMV-3DR reporting mcherry signal pooled

605   from 2 FOVs of one independent experiment. Data in **g** are shown as dots of MCMV-3DR reporting

606   mcherry signals in n = 21 E-Cadherin$^+$ cells and n = 28 in CD11c$^+$ cells and as percentage of n =

607   103 small and n = 21 big MCMV-3DR reporting mcherry signals pooled from 9 FOVs of 3

608   independent experiments. Statistical significance was determined using single unpaired two-tailed

609   t test **(g)**. ****P<0.0001. Scale bar in **b** = 50 μm, in **c** = 50 μm (3D global view) and 30 μm

610   (magnified 2D FOVs), in **e** = 10 μm and in **f** = 10 μm. FOV = Field of view.

611

612

613

614

615

616

617

618

619

620

621

622

623

624

625

626

627 **The chemokines CXCL9 and CXCL10 act as chemoattractants in guiding CXCR3-**

628 **competent T cells to site of infection**

629

630 In-depth confocal imaging analysis revealed a preferred clustering behavior of CD4$^+$ T cells in

631 vicinity to sites of infection, and identified further remnants from virus-infected cells as primary

632 antigenic source for IFNγ production. To determine the range in which secreted IFNγ would be

633 sensed in this glandular tissue in order to induce an antiviral state, we analyzed the expression of

634 the known IFNγ-inducible chemokines CXCL9 and CXCL10 upon MCMV infection using the

635 CXCR3-ligand reporter mouse Rex3[30]. In Rex3 mice, CXCL9 and CXCL10 positive cells can

636 simultaneously be detected by concomitant expression of the RFP and blue fluorescent protein

637 (BFP), respectively. Firstly, we i.v. infected Rex3 mice with MCMV-GFP. 60% of CD45.2$^+$

638 hematopoietic cells expressed CXCL10 in naïve SGs, which unexpectedly remained constant

639 following viral infection **(Fig. 6a)**. In contrast, only CD31$^+$ blood vessel constituting endothelial cells

640 from the CD45.2$^-$ non-hematopoietic cell fraction significantly upregulated CXCL10 in response to

641 MCMV-GFP infection, whereas CXCL10 expression levels by CD326$^+$ duct forming epithelial cells

642 and CD31$^-$CD326$^-$ stromal cells were hardly affected by the infection **(Fig 6a, suppl. Fig. 5a-c)**.

643 Furthermore, 70-80% of SGs-resident and half of spleen-localized CD11c$^+$MHCII$^+$ APCs were

644 single CXCL10 positive, and only a minority co-expressed CXCL9 and CXCL10 **(Suppl. Fig. 5d)**.

645 Additionally, most APCs in the SGs were positive for the macrophage-specific marker F4/80

646 **(Suppl. Fig. 5e)**. Next, we performed microscopic analysis to uncover the spatial relationship

647 between SG-infiltrating CD4$^+$ T cells, sites of viral replication, and the presence of CXCL9 and

648 CXCL10 positive cells. Of particular importance, CD4$^+$ T cells were frequently found in small

649 discrete clusters along with CXCL9 and CXCL10-expressing cells. As observed before, these

650 accumulations were not localized in immediate vicinity to sites of viral replication, but rather within

651 close proximity **(Fig. 6b)**. To elucidate whether CXCL9 and CXCL10 served as proxy for IFNγ

652 downstream signaling or as chemoattractants, or both, we followed two approaches. In a first

653 experiment, we examined CXCL9 and CXCL10 expression as potential readout for IFNγ sensing.

654 For this purpose, we adoptively co-transferred either IFNγ-competent (IFNγ$^{+/+}$) CD4$^+$ and CD8$^+$ T

655 cells or IFNγ-deficient (IFNγ$^{-/-}$) CD4$^+$ and IFNγ-competent CD8$^+$ T cells into T cell-deficient Rex3

656 mice (Rex3 x TCRβ^{KO}) one week prior to MCMV-GFP infection and harvested the SGs and

657 spleens 14 or 45 dpi **(Suppl. Fig. 5f)**. Fourteen days post MCMV-GFP infection, we observed

658 similar numbers of SG-infiltrating CD4$^+$ and CD8$^+$ T cells **(Suppl. Fig. 5g)**. Although CD4$^+$ T cells

659 account for nearly 80% of all IFNγ producing cells in MCMV-infected SGs **(Fig. 4c & g)**, transfer

660 of IFNγ$^{-/-}$ CD4$^+$ T cells did not significantly alter CXCL9 and CXCL10 expression levels in diverse

661   non-hematopoietic cell types in the SGs as well as in CD11c$^+$MHCII$^+$ APCs in the SGs and spleens

662   **(Suppl. Fig. 6a & b)**. Moreover, IFNγ$^{-/-}$ CD4$^+$ T cells still assembled together with CXCL9 and

663   CXCL10 expressing cells, developing distinct clusters **(Fig. 6c).** The lack of IFNγ$^{+/+}$ CD4$^+$ T cells

664   resulted only in a slight increase in viral loads 14 days post MCMV-GFP infection with no

665   significant difference at 45 dpi, shortly after the peak of the infection in the SGs **(Fig. 6d, suppl.**

666   **Fig. 1h)**. In a second experiment, we explored the role of CXCL9 and CXCL10 as possible

667   chemoattractants for CXCR3 expressing T cells. By using a competitive model, we investigated

668   the infiltration and localization properties of CXCR3-competent (CXCR3$^{+/+}$) versus CXCR3-

669   deficient (CXCR3$^{-/-}$) CD4$^+$ T cells in the SGs upon MCMV infection. For this purpose, we adoptively

670   co-transferred CD45.2$^+$CXCR3$^{-/-}$ and CD45.1$^+$CXCR3$^{+/+}$ CD4$^+$ T cells together with

671   CD45.1$^+$CXCR3$^{+/+}$ CD8$^+$ T cells into Rex3 x TCRβ^{KO} mice. Seven days post T cell transfer, we i.v.

672   infected mice with MCMV and examined the SGs *in situ* at 14 dpi **(Suppl. Fig. 6c)**. In line with

673   previous results **(Fig. 6b and c)**, CD4$^+$ T cells were predominantly found in clearly visible

674   accumulations, showing a very strong colocalization with CXCL9 and CXCL10 expressing cells

675   **(Fig. 6e)**. Of note, distinction between CXCR3$^{+/+}$ and CXCR3$^{-/-}$ CD4$^+$ T cells based on the congenic

676   marker CD45.1 demonstrated that predominantly CXCR3$^{+/+}$CD4$^+$ T cells were present within these

677   "CXCL9 and CXCL10 hotspots", whereas CXCR3$^{-/-}$ CD4$^+$ T cells appeared to be rather randomly

678   distributed **(Fig. 6f)**. This suggests that CXCR3 enables migration of T cells towards CXCL9 and

679   CXCL10 positive cells within the SGs. However, CXCR3 expression was not a prerequisite for the

680   entry into MCMV-infected SGs, and did not have an impact on the phenotype of CD4$^+$ T cells

681   **(Suppl. Fig. 6d & e).** This latter observation confirms previous findings that showed a redundant

682   role of CXCR3 expression for T cell infiltration into MCMV-infected SGs[31]. Together, these data

683   indicate that CXCL9 and CXCL10-expressing cells in MCMV-infected SGs possess a crucial role

684   in guiding and positioning CXCR3 expressing T cells, and that the presence of IFNγ-deficient CD4$^+$

685   T cells neither compromise expression levels of these chemokines nor have an impact on virus

686   control around the peak of viral load in the SGs 45 dpi.

687

688

689

690

691

692

693

694

695

Figure 6

696
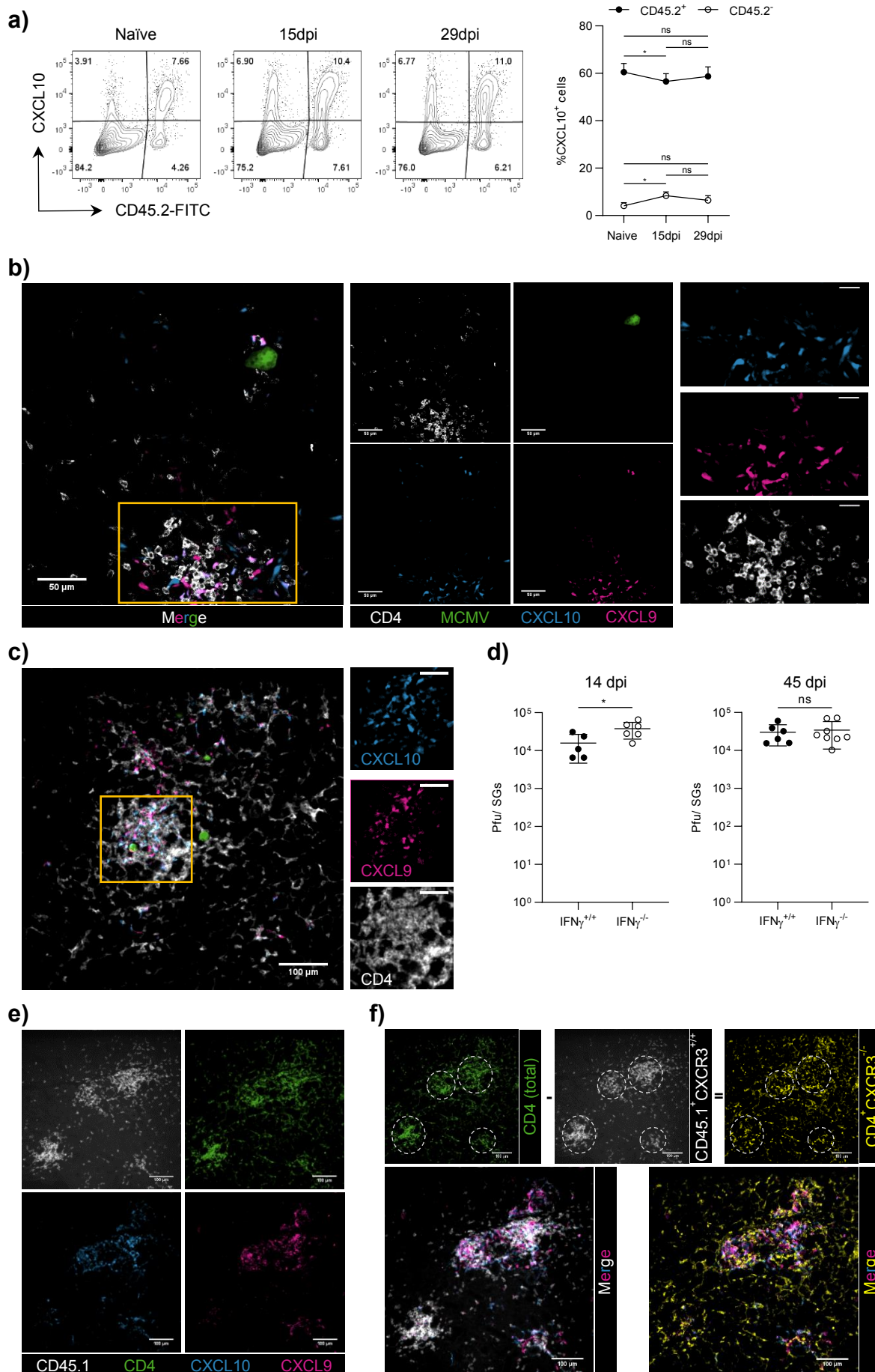
Figure 6. CXCL9 and CXCL10 expression in MCMV-infected SGs. a) Representative flow cytometry contour plots of naïve and MCMV-GFP infected Rex3 mice (left) and percentage of CXCL10$^+$ hematopoietic (CD45.2$^+$) and non-hematopoietic (CD45.2$^-$) cells at indicated days post MCMV-GFP infection (right). **b)** Example of a four color FOV of a Rex3 mouse-derived SG 15 days post MCMV-GFP infection (left). Four single color channel images (middle) and magnified region (yellow frame) split in three single color channel images (right). **c)** Example of a four color FOV of a Rex3 x TCRβ$^{-/-}$ mouse-derived SG harboring IFNγ$^{-/-}$ CD4$^+$ T cells 14 days post MCMV-GFP infection (left) with magnified region (yellow frame) split in three single color channel images (right). **d)** Virus loads in the SGs of TCRβ$^{-/-}$ mice harboring IFNγ competent (IFNγ$^{+/+}$) or IFNγ deficient (IFNγ$^{-/-}$) CD4$^+$ T cells 14 and 45 dpi. **e)** Example of a four single color FOV of a Rex3 x TCRβ$^{-/-}$ mouse-derived SG harboring CXCR3 competent (CD45.1$^+$CXCR3$^{+/+}$) and CXCR3 deficient (CD45.2$^+$CXCR3$^{-/-}$) CD4$^+$ T cells. **f)** Upper row: Image subtraction. Lower row: Merged three color CD45.1$^+$CXCR3$^{+/+}$/CXCL9/CXCL10 (left) and CD4$^+$CXCR3$^{-/-}$/CXCL9/CXCL10 (right) images. Data in **a** are shown as mean + SD of n = 6 - 8 Rex3 mice pooled from two independent experiments. Data in **d** are shown as mean ± SD of n = 5 - 6 TCRβ$^{-/-}$ mice pooled from two independent experiments. Each dot represents either the mean of pooled mice (**a**) or one individual mouse (**d**). Statistical significance was determined using 2-way Anova with post hoc Tukey's multiple comparisons test (**a**) or single unpaired two-tailed t test (**d**). *P<0.05, ns = not significant. Scale bar in **b** = 50 μm (left and middle) and 20 μm (right), in **c** = 100 μm (left) and 50 μm (right), in **e** and **f** = 100 μm.

Mathematical modeling supports eventual viral control by confined local IFNγ production of CD4⁺ T cells in the SGs

To determine if locally confined IFNγ release by CD4⁺ T cells can eventually lead to area-wide control of MCMV infection in the SGs, we combined experimental data with a mathematical model that simulates the interaction of immune and infection processes. Using a cellular Potts modeling framework that allows us to follow the dynamics and motility of individual cells over time, we recapitulated the tissue structure and main cell types within the SMG. The multi-scale model considers the turnover and infection of epithelial cells, including intracellular viral replication and extracellular viral spread, as well as the infiltration, migration and locally confined IFNγ production by endogenous CD4⁺ and M25 CD4⁺ T cells **(Fig. 7a & b)**. Depending on the IFNγ concentration in their surrounding, viral replication of infected cells is inhibited and infected cells are lost. Individual processes and model components were parameterized according to previous data from the literature and adapted to the experimental data. Simulating a total area of 800×800 μm^2, our model represents roughly 1/30 of a 2D cross section of the SMG. For a detailed description of the model and its parameterization please refer to **Materials & Methods** and the detailed **Supp. Information Text S1 – Mathematical model**.

Our simulations show that after an initial increase in the number of infected cells and total viral load, peaking around 20-30 dpi, local IFNγ secretion by infiltrating CD4⁺ T cells can eventually control viral infection in the SGs 45-60 dpi **(Fig. 7c & d)**, similar to the experimental data. In this regard, a model that includes attraction of CD4⁺ T cells to CXCL9 and CXCL10 positive tissue areas populated with APCs, which engulf remnants of previously infected cells, contributes to reduced pathology and faster immune control of the MCMV infection. In contrast, a scenario that does not consider this chemical gradient-mediated migration behavior of CD4⁺ T cells, but rather assumes an undirected motion of CD4⁺ T cells (i.e. w/o APCs), is associated with an elevated and less controlled viral burden. The former scenario leads to increased clustering properties of CD4⁺ IFNγ⁺ T cells **(Fig. 7e)**, with the majority of M25 CD4⁺ T cells accumulating in close proximity to actively MCMV infected cells **(Fig. 7f)**. However, IFNγ-producing CD4⁺ T cells are not directly located next to sites of active viral replication, which is in line with the experimental observations **(Fig. 4e & 7g)**. Of note, IFNγ producing CD4⁺ T cells do not show signs of clustering and are more heterogeneously distributed if the relevant contribution of APCs is ignored **(Fig. 7e)**. Next, clustering of CD4⁺ T cells by APCs enables a concerted release of IFNγ by several CD4⁺ T cells, which leads to increased local cytokine concentrations **(Fig. 7h)**. In doing so, the accumulation of IFNγ−protected sites over time finally leads to viral control in the entire simulated tissue section.

766   As our model assumes a restricted effective range for IFNγ released by CD4$^+$ T cells with a at

767   least 10%-chance to inhibit viral replication up to a radius of roughly ~30 μm around the cell,

768   individual CD4$^+$ T cells are less effective in controlling active viral replication. Therefore, in case

769   of not provoking accumulations of CD4$^+$ T cells by APCs, IFNγ concentrations are generally lower

770   and more transient, mediating less efficient control of the infection **(Fig. 7c, d & h)**.

771   Thus, our model shows that accumulations of CD4$^+$ T cells by CXCL9/CXCL10 chemotactic

772   gradients increases the efficiency of confined IFNγ release by individual CD4$^+$ T cells, which confer

773   improved regional-confined tissue protection and eventual viral control.

774

775

776

777

778

779

780

781

782

783

784

785

786

787

788

789

790

791

792

793

794

795

796

797

798

799

800

Figure 7
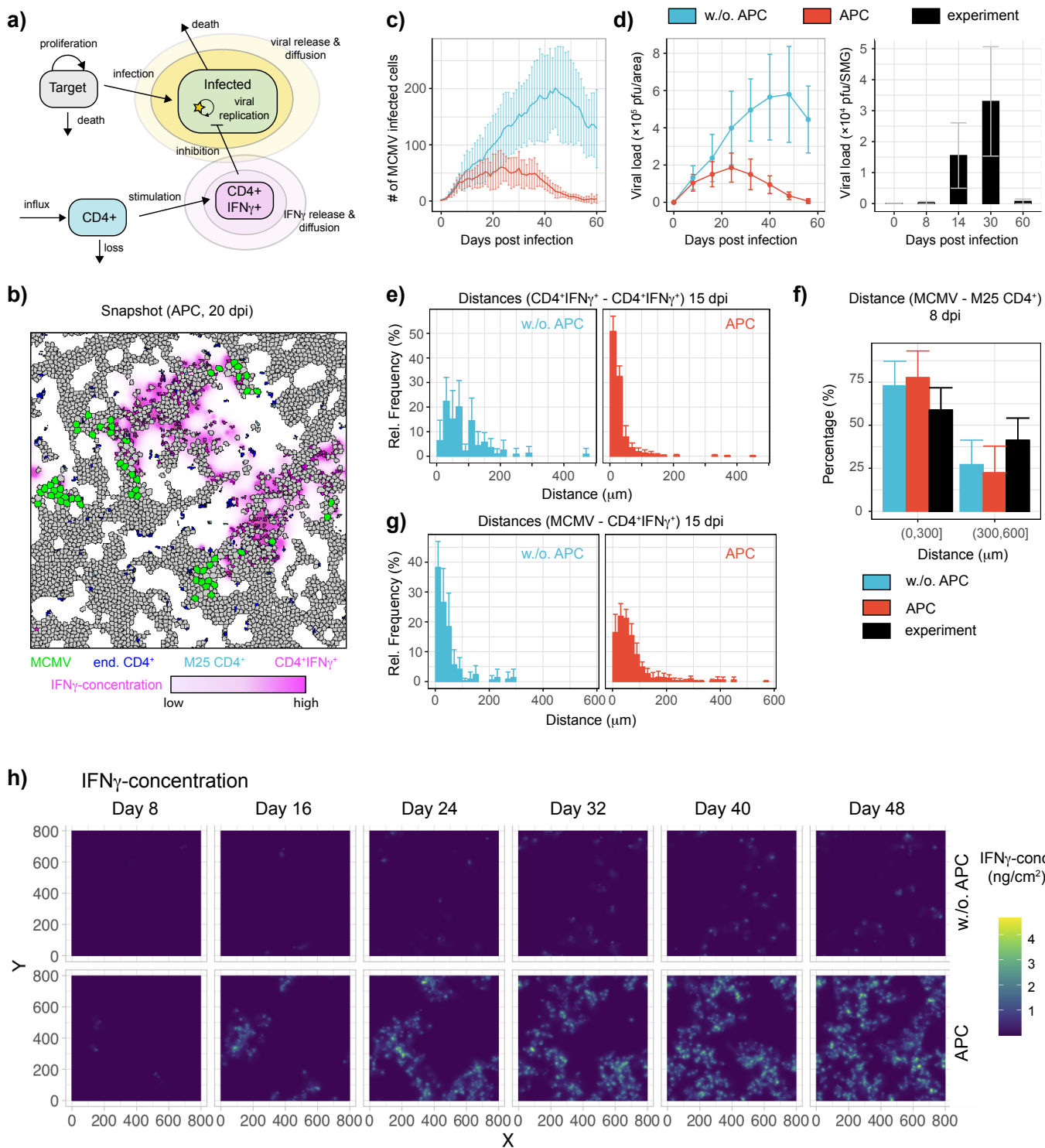
Figure 7. Mathematical modeling of viral-immune interactions in the SGs. a) Sketch of the main processes considered within the mathematical model. **b)** Snapshot of the modeled SMG tissue area of 800×800 μm^2 at 20 dpi considering APC related guidance of CD4$^+$ T cells. The plot indicates the non-duct areas with uninfected (grey) and active MCMV harboring (green) epithelial cells, as well as endogenous CD4$^+$ (blue) and M25 CD4$^+$ T cells (light blue). CD4$^+$ IFNγ$^+$ T cells are shown in pink with IFNγ$^+$ concentrations indicated by the same, gradient color. **c and d)** Dynamics of the number of infected (MCMV$^+$) cells **(c)** and viral load **(d)** for scenarios with (red) and without (blue) APC-associated CXCL9/CXCL10 attraction of CD4$^+$ T cells. Experimental data show the viral load for the whole SMG (n= 8-9 mice, mean+/-SD). **e)** Clustering of CD4$^+$ IFNγ$^+$ T cells indicated by the distance of one IFNγ producing CD4$^+$ T cell to its nearest neighbor. **f)** Distances of M25 CD4$^+$ T cells to the nearest MCMV infected cell. **g)** Distances of IFNγ producing CD4$^+$ T cells to the nearest MCMV infected cell. **h)** Dynamics of the IFNγ concentration within the simulated tissue section of 800×800 μm^2 over the progression of infection. For each scenario, i.e., w./o. and with APC, one representative simulation out of ten replicates is shown. All simulations were run over 60 days in total. Results in panel **(c-g)** are based on ten replicates for each scenario, with the mean and standard deviation (error bars) indicated. Please note that simulations are generally run with higher infection dynamics than observed experimentally for computational efficiency to account for the small simulated grid size (see Materials & Methods). Therefore, viral loads can only be qualitatively compared to experimental data.

Discussion

Infection of mice with MCMV induces an acute infection with lytic viral replication, followed by persistence of latent viral genomes from which sporadic reactivation events can occur. While acute infection is controlled in most organs within one to two weeks, the SGs represent a unique mucosal niche with sustained viral replication and hence persistence over several weeks[32]. Despite the marked infiltration of functional T cells, latency in this peripheral glandular tissue is only achieved two months post viral trigger. One key contribution to this delayed immune control is CMV's interference with antigen presentation that prevents the recognition of infected cells by CD8^{+} T cells, and in less documented circumstances by CD4^{+} T cells too[33–39]. Since the decreased expression or the complete lack of MHC class I on affected cells would induce a "missing self" signal and hence render virally infected cells susceptible to NK cell-mediated killing, CMV encodes for a MHC class I homolog, serving as surrogate MHC class I molecule preventing NK cell attack[40]. Moreover, MCMV mutants lacking the m157 gene and having a functional version of MCK2 gene product, reveal enhanced dissemination and virulence properties[41–47]. Therefore, the acquisition of beneficial virus-specific *in vivo* characteristics that allow MCMV to persist preferentially in the SGs are responsible for the negligible role of NK and CD8^{+} T cells to control MCMV infection in the SGs, and further highlight a superior contribution of CD4^{+} T cells in viral control[7,8].

In the present study, we investigated the crucial antiviral effector functions by CD4^{+} T cells upon CMV infection in murine salivary glands. Although previous studies have already identified an indispensable role of IFNγ producing CD4^{+} T cells in controlling MCMV infection in the SGs, relevant spatiotemporal information was missing that might help to explain the overall slow process of CD4^{+} T cell-mediated viral control[12,13].

Here, we combined experimental data together with mathematical models to provide a mechanistic understanding of the dynamics of viral spread and immune protection on a cellular level. By generating detailed micro-anatomical information about the tissue localization of infected cells, CD4^{+} T cells, sites of antigen recognition and IFNγ production, and inclusion of these data into mathematical models, we propose a scenario that explains the delayed control of MCMV infection in the SGs.

We found that M25-specific CD4^{+} T cells successfully infiltrated MCMV infected SGs early upon infection, displayed an activated phenotype, and produced considerable amounts of the key pro-inflammatory cytokine IFNγ upon encountering the cognate M25 antigen. However, with gradually increasing viral loads in the SGs, decreasing numbers of M25 CD4^{+} T cells, together with reduced TCR signaling events over time, suggested a negligible contribution to early MCMV control. Possible reasons might be the temporal shift from early dominant M25-specific CD4^{+} T cells to

905   M09-specific CD4^{+} T cells at later time points[17], and possibly a role for CD4^{+} T cells with other

906   MCMV-specificities, given the large MCMV genome containing more than 200 open reading

907   frames with antigenic potential[32,48]. However, we have previously shown that the adoptive transfer

908   of *in vivo* activated M25 CD4^{+} T cells into sublethally irradiated mice conferred immune protection

909   in various organs in an IFNγ-dependent manner, indicating that M25-specific cells are able to

910   contribute to MCMV control in immunocompromised mice[19]. Focusing on the abundant

911   endogenous CD4^{+} T cell population within the MCMV infected SGs, we demonstrated that CD4^{+}

912   T cells are the primary cellular source of IFNγ production, in accordance to elevated TCR

913   downstream signaling, indicative of antigen recognition. Moreover, *in situ* analysis of MCMV

914   infected SMGs revealed that IFNγ expressing CD4^{+} T cells were mostly found in vicinity to sites of

915   lytic viral replication, in dense clusters surrounding CD11c^{+} cells that contained small inclusions

916   of cellular cargo from previously infected cells. Clearly, these CD11c^{+} cells were not actively

917   infected with MCMV, as this would have resulted in presence of the reporter fluorochrome within

918   the entire cytoplasm and not within confined small areas as observed. We thus speculate that this

919   cargo represents apoptotic cell bodies from previously infected cells[11]. In this regard, Stahl et al.

920   made a similar observation in infected neonatal lungs, where infection with MCMV attracted

921   myeloid cells, leading to the generation of morphologically unique "nodular inflammatory foci (NIF)"

922   (multiple juxta-positioned MCMV infected cells and associated immune cell infiltrates). Within NIF,

923   which were required for efficient containment of the infection, they characterized few small

924   mcherry-containing apoptotic bodies within myeloid cells, revealing the possible uptake of cell

925   debris derived from previously infected cells by these cells[49]. As we observed discrete

926   accumulations of CD4^{+} T cells around CD11c^{+} APCs, with some of them revealing cargo of MCMV

927   infected cells, in combination with local TCR triggering and IFNγ production, we were wondering

928   which signals are required for the recruitment of these cells into regions of antigen presentation.

929   We specifically investigated the role of the CXC chemokines CXCL9 (MIG) and CXCL10 (IP-10)

930   in this process. These two chemokine ligands share the common receptor CXCR3, which is

931   predominantly expressed on effector T cells[22,23]. Whereas IFNγ signaling strongly induces CXCL9

932   expression, CXCL10 can also be upregulated by type I interferons (IFNα/β)[50,51]. CXCR3 is

933   important for directional migration of CD4^{+} and CD8^{+} T cells in various infectious settings[52–54].

934   However, a clear role of CXCR3 expression in MCMV-specific T cells has so far not been

935   demonstrated. Although this chemokine receptor promoted the recruitment of antigen-specific

936   CD8^{+} T cells to MCMV infected liver[55], the lack of CXCR3 expression on CD8^{+} T cells did not

937   interfere with their ability to infiltrate into the SGs upon MCMV infection[31]. In our study, we

938   confirmed that CXCR3 expression on CD4^{+} T cells is dispensable for SG infiltration, however, it

939   played a decisive role for the spatial localization within MCMV infected SGs. We show that

940   CXCR3-competent CD4$^+$ T cells are specifically recruited to sites of CXCL9 and CXCL10

941   expression, leading to the formation of distinct CD4$^+$ T cell clusters surrounding APCs. In contrast,

942   despite similar infiltration capacity and phenotypic characteristics of CXCR3-deficient CD4$^+$ T

943   cells, these cells rather distributed randomly. Since we identified TCR engagement and IFNγ

944   production mainly within these dense aggregations of T cells, this observation suggests that

945   CXCR3-deficient CD4$^+$ T cells might have reduced chances for antigen encounter and hence

946   ability to produce IFNγ. Interestingly, surface expression of CXCR3 was almost completely absent

947   on SG-residing CD4$^+$ T cells, most likely due to ligand engagement and receptor internalization,

948   as shown in a recent publication[56].

949   Finally, by feeding our experimental data into mathematical models, we developed a simulation

950   scenario of the CD4$^+$ T cell-mediated MCMV control in the SGs. In doing so, we could show that

951   a local rather than long-range protection capability of IFNγ producing CD4$^+$ T cells leads to

952   eventual infection control in the SGs. Individual small areas, defined by IFNγ−producing

953   and sensing cells, provide site-specific antiviral protection, and allow MCMV to spread and

954   replicate at spots that have not yet been yet exposed to IFNγ. Furthermore, due to the indirect

955   antigen recognition on CD11c$^+$ APCs that have engulfed cargo of previously infected cells, effector

956   CD4$^+$ T cell responses occur in a delayed manner, i.e. only after a virus-infected cell has already

957   ceased to produce new virions. This indirect antigen recognition enables ongoing viral replication

958   over several weeks in the SGs. However, the accumulation of effector CD4$^+$ T cell responses by

959   APCs potentiates the IFNγ concentration within local regions, leading to larger areas of IFNγ−

960   mediated protection and faster viral control in comparison to scenarios without APC mediated

961   clustering of CD4$^+$ T cells. Ultimate control of the lytic infection and the transition into a latent state

962   would hence only happen after continued accumulation of locally protected areas, finally resulting

963   in an organ-wide protection. Pursuing the idea of a short-range diffusion property of IFNγ, Müller

964   et al. revealed a few years ago a confined action radius of IFNγ that induced potent protection

965   mechanisms beyond the immunological synapse, in (bystander) cells located more than 80 μm

966   away from the T cell-APC interaction[57]. These would imply that within the vicinity of IFNγ producing

967   CD4$^+$ T cells, depending on the number of IFNγ producing CD4$^+$ T cells and the amount of per-

968   cell produced IFNγ, surrounding cells being maximally eight cell layers away from the IFNγ source

969   should be able to sense the secreted IFNγ and thus being protected from MCMV infection.

970   In this context, our mathematical model provides first mechanistic insights into the dynamics of

971   MCMV infection and clearance in the SGs by combining different types of experimental data and

972   measurements. Although the model only captures a small fraction of the SMG, and therefore

973   considers a higher infection level than observed experimentally, it provides a qualitative

974   representation of the observed infection dynamics, as well as quantitative analysis of the

975   spatiotemporal relationships of individual cells. With the results shown above relying on

976   parameterizations that favor local viral spread[58], eventual viral control is also achieved by locally

977   mediated IFNγ protection if MCMV would spread more heterogeneously within the tissue given

978   higher viral diffusion, but would require larger local IFNγ perimeters. In general, the ability and

979   rapidness of viral control depends on the extension and duration of local IFNγ concentrations,

980   which is considerably enhanced by APC-mediated clustering of CD4$^+$ T cells. More detailed and

981   time-resolved measurements, as e.g. on the stability and longevity of APC-formed CD4$^+$ T cell

982   clusters, or on the dynamics of IFNγ secretion by individual CD4$^+$ T cells, will help to improve the

983   parameterization of the model and validate previous parameter choices.

984

985

986

987

988

989

990

991

992

993

994

995

996

997

998

999

Materials & Methods

Ethics Statement

This study was conducted in accordance to the guidelines of the animal experimentation law (SR 455.163; TVV) of the Swiss Federal Government. The protocols were approved by the Cantonal Veterinary Office of the canton Zürich, Switzerland (animal experimental permissions: 146/2014 and 114/2017).

Mice

Eight to twelve-weeks old age -and sex-matched mice were used for each experiment described in this study. C57BL/6J mice were purchased from Janiver Elevage and referred to as WT B6 mice. C57BL/6N-Tg(TCRaM25,TCRbM25)424 Biat (M25-III) (M25xLy5.1) mice harbor TCR tg CD4$^+$ T cells specific for the M25$_{411-425}$ peptide on the CD45.1 congenic background. The congenic CD45.1 WT B6 mice were bred in house. Nur77GFP (JAX stock # 016617), DssRed.T3 (JAX stock # 006051), Great (JAX stock # 017580), IFNγ$^{-/-}$ (JAX stock # 002287) and TCRβ$^{-/-}$ (JAX stock # 002118) mice were obtained from the Jackson Laboratory. CXCR3$^{-/-}$ (JAX stock # 005796) mice were obtained from the Swiss immunological mouse repository (SwimmR). M25xNur77GFP and M25xRFP CD4$^+$ T cells were generated by crossing the M25xLy5.1 mice to the Nur77GFP -and DssRed.T3 mice, respectively. Rex3 mice were kindly provided by Prof. Matteo Iannacone (IRCCS San Raffaele Scientific Institute, Milan, Italy) in agreement with Prof. Andrew D. Luster (Massachusetts General Hospital, Massachusetts, USA), and crossed to TCRβ$^{-/-}$ mice for the development of the Rex3 x TCRβ$^{-/-}$ mice. CD11cYFP-Prox1mOrange2 mice were kindly provided by Prof. Cornelia Halin Winter (Swiss Federal Institute of Technology Zurich, Zurich, Switzerland). All mice were bred and housed under specific pathogen-free conditions in animal facilities at the Swiss Federal Institute of Technology in Zurich, Hönggerberg. Mice were exposed to a 12:12 h light-dark cycle with unrestricted access to water and food.

Viruses and infections

All recombinant MCMVs were deficient in m157 protein expression (Δm157) and had a functional version of the MCK2 gene product (MCK2$^+$). MCMV-GFP expresses green fluorescent protein (GFP) under the m157 promoter and MCMV-3DR expresses the red fluorescent protein mcherry under the major immediate-early promoter[59–61]. MCMV-3DR was obtained from Prof. Martin Messerle (Hannover Medical School, Hannover, Germany) in agreement with Prof. Reinhold

1030 Förster and Dr. Stephan Halle (Hannover Medical School, Hannover, Germany). The non-
1031 fluorescence encoding MCMV strain was kindly provided by Prof. Luka Cicin-Sain (Helmholtz
1032 Centre for Infection Research, Braunschweig, Germany) in agreement with Prof. Stipan Jonjić
1033 (University of Rijeka, Rijeka, Croatia) and referred to as MCMV[62]. MCMV strains were propagated
1034 on M2-10B4 cells and subsequently purified by ultracentrifugation on a 15% sucrose cushion as
1035 previously described[3]. Viral titers were determined by standard plaque assay on M2-104 cells with
1036 centrifugal enhancement. Mice were infected with 2×10^5 or 5×10^5 plaque forming units (Pfu) of
1037 the respective MCMV mutant by i.v. tail injection.

Adoptive transfers

1039 CD4$^+$ T cells from naïve M25xLy5.1, M25xNur77GFP, M25xRFP, IFNγ$^{-/-}$, CXCR3$^{-/-}$ or CD45.1 WT
1040 B6 mice, and CD8$^+$ T cells from naïve CD45.1 or CD45.2 WT B6 mice, were purified from spleens
1041 by positive selection using anti-CD4 or anti-CD8α magnetic activated cell sorting (MACS) beads
1042 (Miltenyi Biotech, Bergisch Gladbach, Germany) according to the manufacturer's instructions. Cell
1043 viability was assessed by trypan blue exclusion and confirmed to be greater than 90%. Flow
1044 cytometric cell analyses indicated >95% purity of the isolation procedures. 9×10^5 or 10^6 M25 CD4$^+$
1045 T cells were adoptively transferred into naïve recipient WT B6 mice one day prior MCMV or
1046 MCMV-GFP infection. 3×10^6 or 3.5×10^6 CD4$^+$, and 10^6 CD8$^+$ T cells were adoptively transferred
1047 into naïve recipient Rex3 x TCRβ$^{-/-}$ or TCRβ$^{-/-}$ mice seven days prior MCMV or MCMV-GFP
1048 infection. Cell transfers were executed by i.v. tail injection.

***In vivo* peptide stimulations & intravascular antibody labeling**

1050 10^6 MACS isolated M25 CD4$^+$ or M25xNur77GFP CD4$^+$ T cells were adoptively transferred one
1051 day prior MCMV infection into naïve recipient WT B6 mice. M25 peptide (amino acid sequence:
1052 NHLYETPISATAMVI) was purchased from EMC microcollections (Tübingen, Germany) and 20
1053 µg of the M25 peptide in 0.5% DMSO in 1x PBS solution were injected i.v. at day 8 or 21 post
1054 MCMV infection. Three hours post M25 peptide challenge, SGs and spleens were harvested in
1055 complete cell culture medium (RPMI1640 supplemented with 10% FCS, 2mM L-Glutamine, 1x
1056 penicillin/streptomcyin) with additional 10 µg/ml Brefeldin A. Following digestion or meshing of
1057 organs was performed in further presence of 5 µg/ml Brefeldin A.
1058 Intravascular labeling was performed by i.v. administration of 3 µg of fluorophore-conjugated anti-
1059 CD45.1 antibody 3 min prior euthanasia with CO_2 as described previously[63]. Organs were
1060 subsequently perfused with 10 ml of 1x PBS and harvested for subsequent lymphocyte isolation
1061 and flow cytometric analysis.

Lymphocyte isolation and Flow cytometry

Mice were euthanized by CO_2 inhalation, and the SGs and lungs were subsequently perfused via the right heart ventricle with 10 ml ice-cold 1x PBS to remove circulating blood. Single-cell suspensions of spleens and lungs were prepared as previously described with slight modifications[64]. Briefly, spleens were passed through metal grids using syringe plungers. The SGs and lungs were cut into small pieces and digested in complete cell culture medium containing 2.4 mg/ml collagenase type I and 0.2 mg/ml DNaseI for 2 x 20 min at 37°C on a thermomixer. Additionally, they were flushed through 18G and 21G needles in between and after the second round of digestion, respectively, and subjected to centrifugation over a 30% Percoll gradient. Prior to fluorophore-conjugated antibody labeling, cells were treated with a hypotonic ammonium-chloride-potassium lysis buffer for 5 - 10 min at room temperature (RT) to remove remaining erythrocytes. Cells were washed and cell surface staining was executed for 20 min at RT in the dark. In case of continuing intracellular cytokine staining, cells were fixed and permeabilized in 2 × FACS BD Lysis Solution (BD Biosciences) with 0.08% Tween20 in ddH_2O for 10 min at RT in the dark. Subsequent intracellular staining for IFNγ and TNFα was performed for 35 min at RT in the dark. Dead cells were excluded by applying a LIVE/DEAD fixable Near-IR staining (ThermoFisher Scientific). All staining and washing steps were performed in FACS buffer (2% FCS and 5mM EDTA in 1x PBS). Fluorescently labeled antibodies were purchased from Biolegend (Lucerna Chem AG) or BD Biosciences, and are summarized in **Table 1**. Multi-parametric flow cytometric analysis was performed using LSRII flow cytometer (BD Biosciences, Allschwil, Switzerland) with FACSDiva software. Data were analyzed using FlowJo software (Version 10.4.2, Tree Star).

Plaque forming assay

Viral loads in organs were determined on M2-104 cells as described previously[65]. Briefly, 50'000 M2-10B4 were added to each well of a 24-well plate one day prior organ-derived virus exposure. Freshly harvested or in -80°C stored organ in 1 ml complete cell culture medium was homogenized using a metal bead at 25 Hz for 1 - 1.5 min by TissueLyser (Qiagen, Hilden, Germany). After centrifugation at 3500g for 5 min, virus containing supernatant was taken and transferred to a new Eppendorf tube. A 10x serial dilution of the supernatant in complete cell culture medium was performed using round-bottom 96-well plates. Medium of the previous day cultivated M2-10B4 cells was aspirated and replaced by the diluted supernatant. The 24-well plates were centrifuged for 30 min at 535g and subsequently incubated for 1h at 37°C. Medium was aspirated and

1095 replaced by 2.2 % Methylcellulose (4000 centipoise) in ddH$_2$O supplemented with 1x MEM, 10%
1096 FCS, 2mM L-Glutamine, 1% penicillin-streptomcyin and 10mM HEPES/sodium bicarbonate
1097 solution. Plates were incubated for four days at 37°C. After four days of incubation, 500 µl of 25%
1098 Formaldehyde solution in ddH$_2$O was added on top of the methylcellulose layer and plates were
1099 left for 3h at RT. Next, plates were inverted to remove viscous medium and carefully washed three
1100 to four times with 1x PBS. Crystal violet solution was added to the wells and plates were incubated
1101 for 20 min at RT. Finally, plates were washed with ddH$_2$O, air-dried, and plaques were counted
1102 using an inverted microscope. With the exception of the 1h incubation period at 37°C, all steps
1103 were carried out at 4°C. Detection limit was set to 100 Pfu.

1104 **2D Immunohistochemistry - Tissue preparation & Staining**

1105 1x PBS-perfused SGs were fixed in methanol-free 4% formaldehyde solution for 4 - 6 h at 4°C.
1106 After a short wash in 1x PBS, organs were cryoprotected in 30% sucrose in 1x PBS overnight
1107 (o/n) at 4°C, followed by an embedding in optimal cutting temperature (O.C.T) compound and a
1108 snap-freezing in liquid nitrogen. The SG samples were stored at -80°C until further usage. Frozen
1109 tissue sections of 10 µm thickness were generated by a cryostat-microtome, 2 - 3 hours air-dried,
1110 and stored at -20°C if not directly used. Completely air-dried thin tissue sections of the SGs were
1111 washed with 1x PBS to remove remaining O.C.T compound and marked with an hydrophobic
1112 barrier PAP pen (H-4000, Vector Laboratories). Tissue sections were blocked in 1x PBS
1113 containing 10% normal goat serum (NGS), 1% Bovine serum albumin (BSA) and 0.1% TritonX-
1114 100, for 1h at RT. Subsequent staining steps with unlabeled and/or fluorochrome-conjugated
1115 antibodies were executed for 1h at RT or o/n at 4°C in the dark. Slides were washed in between
1116 three times for 7 min in 1x PBS. Finally, sections were washed again in 1x PBS and carefully
1117 rinsed with ddH$_2$O, before counterstained with 4',6'-diamidino-2-phenylindole (DAPI) for 5 min at
1118 RT and mounted in home-made Mowiol-DABCO solution (see CSH protocols; RI: 1.45 - 1.52).
1119 Slides were stored at RT for one to two days in the dark before microscopic investigation.
1120 Immunolabeling was performed in 1x PBS containing 3% BSA and 0.1% TritonX-100 in a humidity
1121 chamber. Antibodies were purchased from Biolegend (Lucerna Chem AG), Life Technologies
1122 (Thermo Fisher Scientific), BD Biosciences, Clontech Laboratories and Rockland
1123 Immunochemicals, and are summarized in **Table 2**.

1124 **2D Immunohistochemistry - Imaging & Analysis**

1125 Images of thin tissue slices were acquired with an inverted confocal microscope (Axiovert 200m
1126 microscope, Carl Zeiss, Inc., Zurich, Switzerland), equipped with an CSU-X1 spinning-disk

1127   confocal unit (Yokogawa), a 20x (Nummerical aperture (NA): 0.5, Immersion: Air) or a 10x (NA:

1128   0.3, Immersion: Air) magnification phase contrast objective, a solid state laser unit with 4 laser

1129   lines (405, 488, 561, 647, Toptica) and two Evolve 512 EMCCD cameras (Photometrics).

1130   Detection and spectral separation of excited fluorophores were achieved through the usage of

1131   specific emission bandpass filters (450/50, 525/50, 605/52 and 700/75). Images with sequential

1132   fluorophore excitation and with z-stacks sizes of 1 μm were recorded and analyzed using

1133   imageJ/Fiji software (Version 1.51). An initial brightness/contrast enhancement was performed

1134   with subesequent quantitative analysis of IFNγ producing (EYFP$^+$) cells using the cell counter

1135   plugin.

1136   **Whole slide Imaging & Analysis**

1137   10 μm thin frozen tissue sections of MCMV infected SGs were prepared and stained according to

1138   the 2D immunohistochemistry part. However, only SG sections, which do not show any signs of

1139   processing-mediated artifacts (e.g. tissue distortions, air bubbles or folds), were subjected to

1140   whole slide scanning using Slide Scanner Pannoramic 250 Flash III (3D Histech, Budapest,

1141   Hungary) to realize faithful data for further downstream analysis. Images with a z-stack size of 0.6

1142   μm were acquired using a 20x magnification objective (NA: 0.8, Immersion: Air). Recorded mrxs

1143   files were directly imported into the HALO® software (https://indicalab.com/halo/; Version

1144   3.0.311.373; Indica Labs, Albuquerque, New Mexico, USA) for quantitative image analysis. In

1145   doing so, we first applied tissue annotation to delimit our spatial analysis to the SMG. We then

1146   performed a categorization of diverse tissue types (i.e. endogenous CD4$^+$ and M25 CD4$^+$ T cells,

1147   sites of viral replication, duct cells, other cells and background) using tissue classifier (Random

1148   Forest). We next exerted Highlex FL module (Version 3.1.0.0) for the simultaneous detection of

1149   various cell types based on fluorescence marker intensities in the different cellular compartments

1150   (i.e. nucleus, cytoplasm and cell membrane). In this regard, we first identified and segmented all

1151   DAPI$^+$ cells, irrespective of cell type (Nuclear contrast threshold = 0.5, Minimum Nuclear Intensity

1152   = 0.1, Nuclear Segmentation Aggressiveness = 0.8 and Minimum Nuclear Roundness = 0).

1153   Afterwards, endogenous CD4$^+$ and M25 CD4$^+$ T cells were defined within DAPI$^+$ cells based on

1154   fluorescence signal intensities in the previously mentioned cellular compartments (see table

1155   below). In this regard, endogenous CD4$^+$ T cells expressed only cell membrane marker CD4 (=

1156   DAPI$^+$CD4$^+$ cells) whereas M25 CD4$^+$ T cells were additionally positive for the cytoplasmic RFP

1157   signal (= DAPI$^+$CD4$^+$RFP$^+$ cells). Finally, quantitative spatial tissue analysis was executed using

1158   nearest neighbor analysis in conjunction with proximity analysis to determine the relative spatial

1159   distribution of cells and sites of viral replication across the tissue section. Micro-anatomical

1160   localization of sites of viral replication was provided by the tissue classifier.

1161   Tresholding (signal intensities):

Fluorescent label (marker)	Nucleus	Cytoplasm	Cell membrane
DAPI	1	-1	-1
AF568 (RFP)	40	40	0
AF647 (CD4)	35	35	0

1162   Signal range: 0 (= no signal) - 255 (= highest intensity)

1163

1164   **3D Immunohistochemistry - Tissue preparation & Staining**

1165

1166   1x PBS perfused SGs were fixed in methanol-free 4% formaldehyde solution for 4 - 6 h at 4°C.

1167   After a short wash in 1x PBS, organs were embedded in low-melting 4% agarose in 1x PBS, and

1168   subsequently cut in 200 µm thick tissue sections using a Compresstome® (Precisionary,

1169   Greenville, USA). Slices were collected in 6-well plates pre-filled with 0.1% PBST and incubated

1170   for 24 h at RT. PBST was aspirated and sections were incubated overnight in blocking buffer (1x

1171   PBS containing 10% NGS, 1% BSA and 0.1% TritonX-100) at 4°C. Blocking buffer was removed

1172   and sections were stained in 6, 12 or 24-well plates with primary fluorochrome-conjugated

1173   antibodies diluted in 3% BSA in 1x PBS for three to four days at 4°C or RT (**Table 2).** Next, slices

1174   were washed three to four times with 1x PBS during a 24 h period at 4°C. 1x PBS was removed,

1175   and a home-made RIMS with RI = 1.47 (45 g Histodenz in 30 ml 1x PBS) was added to the

1176   sections. The samples were incubated in the dark on a rotator for 6 h at RT. Finally, SG sections

1177   were mounted using fresh RIMS and appropriate 200 µm thick iSpacer® (SunJin Lab, Hsinchu,

1178   Taiwan). Tissue samples were stored one to two days at RT in the dark prior confocal imaging.

1179

1180   **3D Immunohistochemistry - Imaging & Analysis**

1181

1182   Images of 200 µm thick tissue sections were acquired with an inverted confocal microscope (Leica

1183   TCS SP8 MP), using a 25x magnification objective (NA: 0.95, Immersion: Water), a laser unit with

1184   AOBS system (405, 488 (Argon Laser), 561, 633), and internal detection with 1 PMT detector and

1185   2 Leica Hybrid detectors, operated by the Leica LAS X 3.5.5. Images were acquired with

1186   sequential fluorophore excitation, z-stacks sizes of 2 µm and a scan format of 512x512 pixels.

1187 Image analysis was performed using imageJ/Fiji software (Version 1.51), Imaris 9.5 (Bitplane,

1188 Zurich, Switzerland) and RStudio (Version 1.1.463). Using Imaris, several processing steps were

1189 applied to the images (**Table 3**). The acquired signals were attributed to each individual cell

1190 (surface creation), or its location was determined without accurate segmentation of cell bodies by

1191 the generation of spherical objects centered on any pixels with signal above a user set threshold

1192 (spots creation) (**suppl. Fig 4c**). For the CD4 channel, gamma was adjusted to 1.35, and

1193 Gaussian smoothing was used with a width of 0.32 μm. Finally, surfaces and spots were created

1194 according to the parameters in **Table 4**. Appeared extra-cellular and likely represented imaging

1195 artefacts were not selectively removed from analysis to avoid introducing user bias.

1196

1197 ***Ex vivo* live imaging**

1198

1199 Mice were euthanized by CO_2 inhalation, and the SGs were harvested in complete cell culture

1200 medium (RPMI1640 supplemented with 10% FCS, 2mM L-Glutamine, 1x penicillin/streptomycin).

1201 The organs were embedded in 4% agarose in 1x PBS, and subsequently cut in 200 μm thick

1202 tissue sections using a Compresstome® (Precisionary, Greenville, USA). Slices were collected in

1203 6-well plates filled with live imaging medium (RPMI 1640 without phenol red supplemented with

1204 10% FCS, 2mM L-Glutamine, 1x penicillin/streptomycin, 1M Hepes, 50 mM *β*-Mercaptoethanol,

1205 100x Sodium Pyruvate, 100x Minimum Essential Medium Non-Essential Amino Acids). Next,

1206 slices were mounted using live imaging medium and 200 μm thick iSpacer® (SunJin Lab, Hsinchu,

1207 Taiwan). Finally, images were acquired using the 40x magnification objective (NA: 1.1, Immersion:

1208 Water) from the Leica TCS SP8 MP system described above. Time lapses of 5-10 min were

1209 acquired with a time interval of approximatively 25 sec and a scan format of 512x512 pixels. A

1210 brightness/contrast enhancement was performed using imageJ/Fiji.

1211

1212 **Mathematical model of viral-immune interactions in the SGs**

1213

1214 For a detailed description of the mathematical model and its parameterization to analyze the

1215 infection and immune dynamics in the SG please refer to **Supp. Information – Mathematical**

1216 **model**. In brief, a multi-scale cellular Potts model (CPM) for the SMG was developed using the

1217 software Morpheus (http://morpheus.gitlab.io)[66]. The modeling framework allows us to follow the

1218 dynamics and motility of individual cells while accounting for intra- and extracellular processes.

1219 Recapitulation of the tissue structure was achieved by segmenting microscopy images of cross

1220 sections of the SMG using Ilastik Version1.3.3.pos3 (https://www.ilastik.org)[67]. Duct structures

1221 extracted as binary masks were considered as background and non-duct areas later populated by

1222 epithelial cells within Morpheus. The model considers the cellular turnover and infection of
1223 immobile epithelial cells, intracellular viral replication within infected cells, as well as export and
1224 diffusion of extracellular virus. Endogenous CD4$^+$ and M25 CD4$^+$ T cells are able to infiltrate the
1225 tissue and release IFNγ upon encounter of APC or infected cells dependent on the scenario,
1226 thereby inhibiting viral replication within infected cells. All processes of cell proliferation, death,
1227 infection and infiltration follow stochastic processes, which were parameterized according to
1228 experimental data from the literature or current observations within this study. For processes
1229 where reliable measurements are missing, parameter sweeps were performed with model results
1230 challenged against the experimental data to evaluate reasonable parameterizations. Sensitivity of
1231 results with regard to selected parameter combinations were performed. For computational
1232 efficiency, only a small section of 800×800 μm^2 of the SMG tissue was simulated, with the actually
1233 observed 2D-tissue cross sections being 31-34-fold larger (e.g. ~20-22 mm^2). Therefore, our
1234 simulations generally provide a semi-quantitative representation of the experimentally observed
1235 dynamics. Due to the relatively small tissue area simulated, higher infection rates were considered
1236 in order to still be able to characterize spatial relationships of infected and immune cells.
1237 Otherwise, approximately only 1 in 10 simulations would contain one infected cell around day 8
1238 post infection.

1239

1240 **Statistical analysis**

1241

1242 Statistical significance was determined by two-tailed unpaired t test, 2-way Anova with post hoc
1243 Tukey's multiple comparisons test, or two-tailed Pearson correlation using GraphPad Prism
1244 (Version 8.2, La Jolla, CA, USA) with *P< 0.05, **P< 0.01, ***P< 0.001 and ****P< 0.0001.

1245

1246 **Acknowledgment**

1247

1256 supported by the state of Baden-Württemberg through bwHPC (MLS-WISO) and the German

1257 Research Foundation (DFG) through grant INST 35/1134-1 FUGG.

1258

1259 **Table 1**: Flow cytometry antibody list (Surface & **Intracellular staining**)

Marker	Fluorochrome	Manufacturer	Clone	Catalog #	RRID	Conc
B220	PE-Cy7	Biolegend	RA3-6B2	103222	AB_313005	0.4 µg/ml
B220	BV510	Biolegend	RA3-6B2	103247	AB_2561394	1 µg/ml
B220	FITC	Biolegend	RA3-6B2	103206	AB_312991	1 µg/ml
B220	PE	Biolegend	RA3-6B2	103208	AB_312993	0.4 µg/ml
B220	APC	Biolegend	RA3-6B2	103212	AB_312997	0.4 µg/ml
CD11a/CD18 (LFA-1)	PE-Cy7	Biolegend	H155-78	141011	AB_2564307	1 µg/ml
CD11c	FITC	Biolegend	N418	117306	AB_313775	2.5 µg/ml
CD279 (PD-1)	PE-Cy7	Biolegend	29F.1A12	135215	AB_10696422	1 µg/ml
CD3	PE-Cy7	Biolegend	145-2C11	100320	Ab_312685	1 µg/ml
CD3	FITC	Biolegend	145-2C11	100306	AB_312671	1 µg/ml
CD31	PE-Cy7	Biolegend	390	102418	AB_830757	0.3 µg/ml
CD326 (EpCAM)	AF647	Biolegend	G8.8	118212	AB_1134101	0.8 µg/ml
CD4	BV421	Biolegend	RM4-5	100544	AB_11219790	1 µg/ml
CD4	BV605	Biolegend	RM4-5	100548	AB_2563054	1 µg/ml
CD44	BV510	Biolegend	IM7	103044	AB_2650923	1 µg/ml
CD45.1	PE	Biolegend	A20	110708	AB_313497	0.4 µg/ml
CD45.1	APC	Biolegend	A20	110714	AB_313503	0.4 µg/ml
CD45.2	FITC	Biolegend	104	109806	AB_313443	0.4 µg/ml
CD49d	FITC	Biolegend	R1-2	103606	AB_313037	2.5 µg/ml
CD62L	PerCP	Biolegend	MEL-14	104430	AB_2187124	1 µg/ml
CD69	PE-Cy7	Biolegend	H1.2F3	104512	AB_493564	1 µg/ml
CD69	FITC	BD Biosciences	H1.2F3	55326	.	2.5 µg/ml
CD8a	PerCP	Biolegend	53-6.7	100732	AB_893423	1 µg/ml

CD8a	APC	Biolegend	53-6.7	100712	AB_312751	1 µg/ml
CXCR3	BV421	Biolegend	CXCR3-173	126521	AB_10900974	1 µg/ml
F4/80	AF647	Biolegend	BM8	123122	AB_893480	2.5 µg/ml
I-A/I-E (MHCII)	PerCP	Biolegend	M5/114.15.2	107624	AB_2191073	0.4 µg/ml
NK1.1	PE	Biolegend	PK136	108708	AB_313395	1 µg/ml
NK1.1	PE-Cy7	Biolegend	PK136	108714	AB_389364	1 µg/ml
IFNγ	**APC**	**Biolegend**	**XMG1.2**	**505810**	**AB_315404**	**1 µg/ml**
TNFα	**FITC**	**Biolegend**	**MP6-XT22**	**506304**	**AB_315425**	**5 µg/ml**

1260

1261   **Table 2**: Microscopy antibody list (primary & **secondary**)

Marker	Fluorochrome	Manufacturer	Catalog #	Clone	Concentration
CD4	AF647	Biolegend	100530	RM4-5	5 µg/ml
CD4	-	BD Biosciences	550280	RM4-5	2.5 µg/ml
CD8	BV421	Biolegend	100738	53-6.7	4 µg/ml
E-Cadherin	AF647	BD Biosciences	560062	36/E-Cadherin	n/a, 1/125 dilution
CD11b	-	BD Biosciences	557394	M1/70	5 µg/ml
GFP/ EYFP	-	Clontech Laboratories	632592	n/a	n/a, 1/200 dilution
RFP	-	Rockland Immunochemicals	600-401-379	n/a	n/a, 1/200 dilution
CD45.1	AF647	Biolegend	A20	110720	5 µg/ml
Goat, anti-rat	**AF488**	**Thermo Fisher Scientific**	**A-11006**	**polyclonal**	**10 µg/ml**
Goat, anti-rat	**AF555**	**Thermo Fisher Scientific**	**A-21434**	**polyclonal**	**10 µg/ml**
Goat, anti-rat	**AF647**	**Thermo Fisher Scientific**	**A-21247**	**polyclonal**	**10 µg/ml**
Goat, anti-rabbit	**AF488**	**Thermo Fisher Scientific**	**A-11034**	**polyclonal**	**10 µg/ml**
Goat, anti-rabbit	**AF555**	**Thermo Fisher Scientific**	**A-21429**	**polyclonal**	**10 µg/ml**

1262

1263

1264 **Table 3**: General information to volumetric images

Dataset	Fig. 5b & 5e	Fig. 5c	Suppl. Fig. 4c
Description	FOV1 from SMG	FOV2 from SMG	FOV1 from SMG
Total imaged volume (mm^3)	0.0405	0.0405	0.0405
Number of channels	2	2	2
Number of CD4$^+$ T cells	5534	5442	5534
Number of MCMV associated sites	31	55	31

1265

1266

1267 **Table 4**: Technical information to volumetric images

Surface/ Spots creation parameters								
Surface/ Spots name	Source Channel	Smoothing: Surface details (µm)	Background Subtraction: Diameter of largest sphere	Absolute intensity threshold	Split touching objects: Split seed diameter (µm)	Quality threshold	Voxel number threshold	Diamers (spots)
Suppl. Fig. 7a								
MCMV surfaces	MCMV-3DR	0.3	9.00	11.6	7	3.29	19-1160	-
CD11c surfaces	CD11c eYFP	0.5	10	27.9	10	6.03	1075-10060	-
CD4 spots	CD4 AF647	-	true	-	-	2	-	5.5

1268

1269

1270

1271

1272

1273

1274

1275

1276

1277

1278

References

1. Emery, V. C. Investigation of CMV disease in immunocompromised patients. *J. Clin. Pathol.* **54**, 84–88 (2001).

2. Steininger, C. Clinical relevance of cytomegalovirus infection in patients with disorders of the immune system. *Clin. Microbiol. Infect.* **13**, 953–963 (2007).

3. Brune, W., Hengel, H. & Koszinowski, U. H. A mouse model for cytomegalovirus infection. *Curr. Protoc. Immunol.* 19.7.1-19.7.13 (2001) doi:10.1002/0471142735.im1907s43.

4. Hudson, J. B. The murine cytomegalovirus as a model for the study of viral pathogenesis and persistent infections. *Arch. Virol.* **62**, 1–29 (1979).

5. Campbell, A. E., Cavanaugh, V. J. & Slater, J. S. The salivary glands as a privileged site of cytomegalovirus immune evasion and persistence. *Med. Microbiol. Immunol.* **197**, 205–213 (2008).

6. Reddehase, M. J., Mutter, W., Münch, K., Bühring, H. J. & Koszinowski, U. H. CD8-positive T lymphocytes specific for murine cytomegalovirus immediate-early antigens mediate protective immunity. *J. Virol.* **61**, 3102–3108 (1987).

7. Jonjic, S., Mutter, W., Weiland, F., Reddehase, M. J. & Koszinowski, U. H. Site-restricted persistent cytomegalovirus infection after selective long-term depletion of CD4+ T lymphocytes. *J. Exp. Med.* **169**, 1199–1212 (1989).

8. Jonjić, S., Pavić, I., Lucin, P., Rukavina, D. & Koszinowski, U. H. Efficacious control of cytomegalovirus infection after long-term depletion of CD8+ T lymphocytes. *J. Virol.* **64**, 5457–5464 (1990).

9. Doom, C. M. & Hill, A. B. MHC class I immune evasion in MCMV infection. *Med. Microbiol. Immunol.* **197**, 191–204 (2008).

10. Hengel, H. *et al.* Cytomegaloviral control of MHC class I function in the mouse. *Immunol. Rev.* **168**, 167–176 (1999).

11. Walton, S. M. *et al.* Absence of cross-presenting cells in the salivary gland and viral immune evasion confine cytomegalovirus immune control to effector CD4 T cells. *PLoS Pathog.* **7**, e1002214 (2011).

12. Lucin, P., Pavić, I., Polić, B., Jonjić, S. & Koszinowski, U. H. Gamma interferon-dependent clearance of cytomegalovirus infection in salivary glands. *J. Virol.* **66**, 1977–1984 (1992).

13. Lucin, P. *et al.* Late phase inhibition of murine cytomegalovirus replication by synergistic action of interferon-gamma and tumour necrosis factor. *J. Gen. Virol.* **75**, 101–110 (1994).

14. Thom, J. T., Weber, T. C., Walton, S. M., Torti, N. & Oxenius, A. The Salivary Gland Acts as a Sink for Tissue-Resident Memory CD8+ T Cells, Facilitating Protection from Local

1314   Cytomegalovirus Infection. *Cell Rep.* **13**, 1125–1136 (2015).

1315   15.   Smith, C. J., Caldeira-Dantas, S., Turula, H. & Snyder, C. M. Murine CMV Infection

1316   Induces the Continuous Production of Mucosal Resident T Cells. *Cell Rep.* **13**, 1137–

1317   1148 (2015).

1318   16.   Walton, S. M. *et al.* The Dynamics of Mouse Cytomegalovirus-Specific CD4 T Cell

1319   Responses during Acute and Latent Infection. *J. Immunol.* **181**, 1128–1134 (2008).

1320   17.   Arens, R. *et al.* Cutting Edge: Murine Cytomegalovirus Induces a Polyfunctional CD4 T

1321   Cell Response. *J. Immunol.* **180**, 6472–6476 (2008).

1322   18.   Mandaric, S. *et al.* IL-10 Suppression of NK/DC Crosstalk Leads to Poor Priming of

1323   MCMV-Specific CD4 T Cells and Prolonged MCMV Persistence. *PLoS Pathog.* **8**,

1324   e1002846 (2012).

1325   19.   Jeitziner, S. M., Walton, S. M., Torti, N. & Oxenius, A. Adoptive transfer of

1326   cytomegalovirus-specific effector CD4+ T cells provides antiviral protection from murine

1327   CMV infection. *Eur. J. Immunol.* **43**, 2886–2895 (2013).

1328   20.   Verma, S. *et al.* Cytomegalovirus-Specific CD4 T Cells Are Cytolytic and Mediate Vaccine

1329   Protection. *J. Virol.* **90**, 650–658 (2016).

1330   21.   McDermott, D. S. & Varga, S. M. Quantifying Antigen-Specific CD4 T Cells during a Viral

1331   Infection: CD4 T Cell Responses Are Larger Than We Think. *J. Immunol.* **187**, 5568–5576

1332   (2011).

1333   22.   Sallusto, F., Lenig, D., Mackay, C. R. & Lanzavecchia, A. Flexible programs of chemokine

1334   receptor expression on human polarized T helper 1 and 2 lymphocytes. *J. Exp. Med.* **187**,

1335   875–883 (1998).

1336   23.   Bonecchi, R. *et al.* Differential expression of chemokine receptors and chemotactic

1337   responsiveness of type 1 T helper cells (Th1s) and Th2s. *J. Exp. Med.* **187**, 129–134

1338   (1998).

1339   24.   Moran, A. E. *et al.* T cell receptor signal strength in Treg and iNKT cell development

1340   demonstrated by a novel fluorescent reporter mouse. *J. Exp. Med.* **208**, 1279–1289

1341   (2011).

1342   25.   Ashouri, J. F. & Weiss, A. Endogenous Nur77 Is a Specific Indicator of Antigen Receptor

1343   Signaling in Human T and B Cells. *J. Immunol.* **198**, 657–668 (2017).

1344   26.   Ho, M. The history of cytomegalovirus and its diseases. *Med. Microbiol. Immunol.* **197**,

1345   65–73 (2008).

1346   27.   Reinhardt, R. L., Liang, H. E. & Locksley, R. M. Cytokine-secreting follicular T cells shape

1347   the antibody repertoire. *Nat. Immunol.* **10**, 385–393 (2009).

1348   28.   Richardson, D. S. & Lichtman, J. W. Clarifying Tissue Clearing. *Cell* **162**, 246–257 (2015).

1349   29.   Yang, B. *et al.* Single-cell phenotyping within transparent intact tissue through whole-body
1350   clearing. *Cell* **158**, 945–958 (2014).

1351   30.   Groom, J. R. *et al.* CXCR3 Chemokine Receptor-Ligand Interactions in the Lymph Node
1352   Optimize CD4+ T Helper 1 Cell Differentiation. *Immunity* **37**, 1091–1103 (2012).

1353   31.   Caldeira-Dantas, S. *et al.* The Chemokine Receptor CXCR3 Promotes CD8 + T Cell
1354   Accumulation in Uninfected Salivary Glands but Is Not Necessary after Murine
1355   Cytomegalovirus Infection. *J. Immunol.* **200**, 1133–1145 (2018).

1356   32.   Krmpotic, A., Bubic, I., Polic, B., Lucin, P. & Jonjic, S. Pathogenesis of murine
1357   cytomegalovirus infection. *Microbes Infect.* **5**, 1263–1277 (2003).

1358   33.   Del Val, M. *et al.* Cytomegalovirus prevents antigen presentation by blocking the transport
1359   of peptide-loaded major histocompatibility complex class I molecules into the medial-golgi
1360   compartment. *J. Exp. Med.* **176**, 729–738 (1992).

1361   34.   Kleijnen, M. F. *et al.* A mouse cytomegalovirus glycoprotein, gp34, forms a complex with
1362   folded class I MHC molecules in the ER which is not retained but is transported to the cell
1363   surface. *EMBO J.* **16**, 685–694 (1997).

1364   35.   Ziegler, H. *et al.* A mouse cytomegalovirus glycoprotein retains MHC class I complexes in
1365   the ERGIC/cis-Golgi compartments. *Immunity* **6**, 57–66 (1997).

1366   36.   Reusch, U. *et al.* A cytomegalovirus glycoprotein re-routes MHC class I complexes to
1367   lysosomes for degradation. *EMBO J.* **18**, 1081–1091 (1999).

1368   37.   Del Val, M., Münch, K., Reddehase, M. J. & Koszinowski, U. H. Presentation of CMV
1369   immediate-early antigen to cytolytic T lymphocytes is selectively prevented by viral genes
1370   expressed in the early phase. *Cell* **58**, 305–315 (1989).

1371   38.   Hengel, H., Brune, W. & Koszinowski, U. H. Immune evasion by cytomegalovirus -
1372   Survival strategies of a highly adapted opportunist. *Trends Microbiol.* **6**, 190–197 (1998).

1373   39.   Yunis, J. *et al.* Murine cytomegalovirus degrades MHC class II to colonize the salivary
1374   glands. *PLoS Pathog.* **14**, e1006905 (2018).

1375   40.   Farrell, H. E. *et al.* Inhibition of natural killer cells by a cytomegalovirus MHC class I
1376   homologue in vivo. *Nature* **386**, 510–514 (1997).

1377   41.   Fleming, P. *et al.* The Murine Cytomegalovirus Chemokine Homolog, m131/129, Is a
1378   Determinant of Viral Pathogenicity. *J. Virol.* **73**, 6800–6809 (1999).

1379   42.   Saederup, N., Aguirre, S. A., Sparer, T. E., Bouley, D. M. & Mocarski, E. S. Murine
1380   Cytomegalovirus CC Chemokine Homolog MCK-2 (m131-129) Is a Determinant of
1381   Dissemination That Increases Inflammation at Initial Sites of Infection. *J. Virol.* **75**, 9966–
1382   9976 (2001).

1383   43.   Jordan, S. *et al.* Virus Progeny of Murine Cytomegalovirus Bacterial Artificial

1384   Chromosome pSM3fr Show Reduced Growth in Salivary Glands due to a Fixed Mutation
1385   of MCK-2. *J. Virol.* **85**, 10346–10353 (2011).

1386   44.   Arase, H., Mocarski, E. S., Campbell, A. E., Hill, A. B. & Lanier, L. L. Direct recognition of
1387   cytomegalovirus by activating and inhibitory NK cell receptors. *Science (80-.).* **296**, 1323–
1388   1326 (2002).

1389   45.   Smith, H. R. C. *et al.* Recognition of a virus-encoded ligand by a natural killer cell
1390   activation receptor. *Proc. Natl. Acad. Sci. U. S. A.* **99**, 8826–8831 (2002).

1391   46.   Voigt, V. *et al.* Murine cytomegalovirus m157 mutation and variation leads to immune
1392   evasion of natural killer cells. *Proc. Natl. Acad. Sci. U. S. A.* **100**, 13483–13488 (2003).

1393   47.   Bubić, I. *et al.* Gain of Virulence Caused by Loss of a Gene in Murine Cytomegalovirus. *J.*
1394   *Virol.* **78**, 7536–7544 (2004).

1395   48.   Rawlinson, W. D., Farrell, H. E. & Barrell, B. G. Analysis of the complete DNA sequence
1396   of murine cytomegalovirus. *J. Virol.* **70**, 8833–8849 (1996).

1397   49.   Stahl, F. R. *et al.* Nodular Inflammatory Foci Are Sites of T Cell Priming and Control of
1398   Murine Cytomegalovirus Infection in the Neonatal Lung. *PLoS Pathog.* **9**, e1003828
1399   (2013).

1400   50.   Farber, J. M. A macrophage mRNA selectively induced by γ-interferon encodes a
1401   member of the platelet factor 4 family of cytokines. *Proc. Natl. Acad. Sci. U. S. A.* **87**,
1402   5238–5242 (1990).

1403   51.   Luster, A. D., Unkeless, J. C. & Ravetch, J. V. γ-Interferon transcriptionally regulates an
1404   early-response gene containing homology to platelet proteins. *Nature* **315**, 672–676
1405   (1985).

1406   52.   Sung, J. H. *et al.* Chemokine guidance of central memory T cells is critical for antiviral
1407   recall responses in lymph nodes. *Cell* **150**, 1249–1263 (2012).

1408   53.   Hickman, H. D. *et al.* CXCR3 chemokine receptor enables local CD8+ T cell migration for
1409   the destruction of virus-infected cells. *Immunity* **42**, 524–537 (2015).

1410   54.   Kohlmeier, J. E. *et al.* CXCR3 Directs Antigen-Specific Effector CD4 + T Cell Migration to
1411   the Lung During Parainfluenza Virus Infection. *J. Immunol.* **183**, 4378–4384 (2009).

1412   55.   Hokeness, K. L. *et al.* CXCR3-Dependent Recruitment of Antigen-Specific T Lymphocytes
1413   to the Liver during Murine Cytomegalovirus Infection. *J. Virol.* **81**, 1241–1250 (2007).

1414   56.   Maurice, N. J., McElrath, M. J., Andersen-Nissen, E., Frahm, N. & Prlic, M. CXCR3
1415   enables recruitment and site-specific bystander activation of memory CD8+ T cells. *Nat.*
1416   *Commun.* **10**, 1–15 (2019).

1417   57.   Müller, A. J. *et al.* CD4 + T Cells Rely on a Cytokine Gradient to Control Intracellular
1418   Pathogens beyond Sites of Antigen Presentation. *Immunity* **37**, 147–157 (2012).

1419   58.   Wirtz, N. *et al.* Polyclonal cytomegalovirus-specific antibodies not only prevent virus
1420   dissemination from the portal of entry but also inhibit focal virus spread within target
1421   tissues. *Med. Microbiol. Immunol.* **197**, 151–158 (2008).

1422   59.   Hasan, M. *et al.* Selective Down-Regulation of the NKG2D Ligand H60 by Mouse
1423   Cytomegalovirus m155 Glycoprotein. *J. Virol.* **79**, 2920–2930 (2005).

1424   60.   Marquardt, A. *et al.* Single cell detection of latent cytomegalovirus reactivation in host
1425   tissue. *J. Gen. Virol.* **92**, 1279–1291 (2011).

1426   61.   Stahl, F. R. *et al.* Mck2-dependent infection of alveolar macrophages promotes replication
1427   of MCMV in nodular inflammatory foci of the neonatal lung. *Mucosal Immunol.* **8**, 57–67
1428   (2015).

1429   62.   Hirche, C. *et al.* Systemic Virus Infections Differentially Modulate Cell Cycle State and
1430   Functionality of Long-Term Hematopoietic Stem Cells In Vivo. *Cell Rep.* **19**, 2345–2356
1431   (2017).

1432   63.   Anderson, K. G. *et al.* Intravascular staining for discrimination of vascular and tissue
1433   leukocytes. *Nat. Protoc.* **9**, 209–222 (2014).

1434   64.   Joller, N., Spörri, R., Hilbi, H. & Oxenius, A. Induction and protective role of antibodies in
1435   Legionella pneumophila infection. *Eur. J. Immunol.* **37**, 3414–3423 (2007).

1436   65.   Zurbach, K. A., Moghbeli, T. & Snyder, C. M. Resolving the titer of murine
1437   cytomegalovirus by plaque assay using the M2-10B4 cell line and a low viscosity overlay.
1438   *Virol. J.* **11**, (2014).

1439   66.   Starruß, J., De Back, W., Brusch, L. & Deutsch, A. Morpheus: A user-friendly modeling
1440   environment for multiscale and multicellular systems biology. *Bioinformatics* **30**, 1331–
1441   1332 (2014).

1442   67.   Berg, S. *et al.* ilastik: interactive machine learning for (bio)image analysis. *Nat. Methods*
1443   **16**, 1226–1232 (2019).
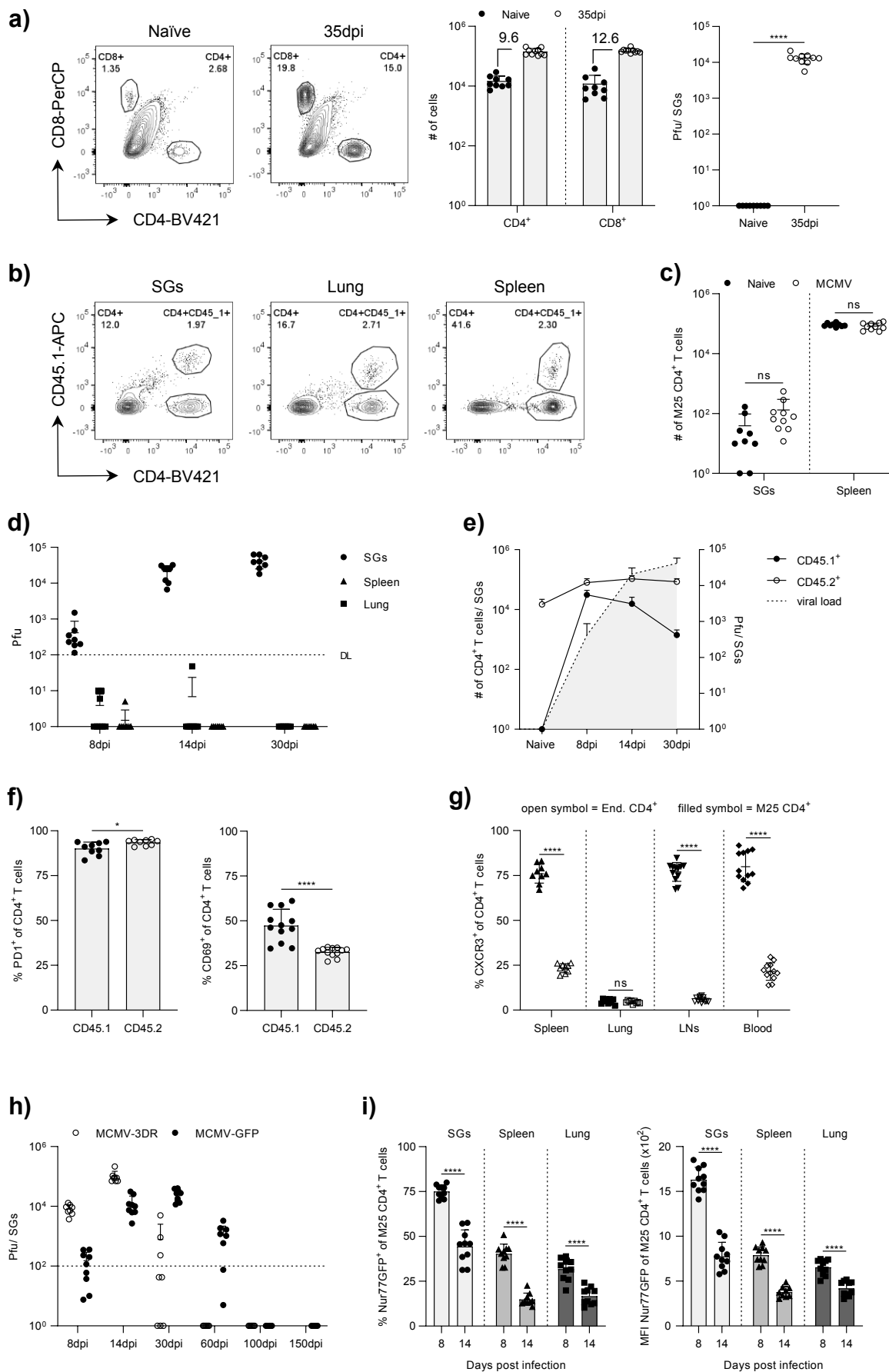
1444

1445

1446

1447

1448

1449

1450

1451

1452

Supplementary Figure 1

1453

1454   **Supplementary Figure 1**: **Kinetics and phenotypic characterization of M25 CD4⁺ T cells. a)**

1455   Representative flow cytometry contour plots showing frequency of SG-localized CD4⁺ and CD8⁺

1456   T cells in naïve WT B6 mice and upon MCMV-GFP infection (left) with total T cell counts (middle)

1457   and viral loads (right) in the SGs (n = 9 – 10 mice). **b)** Representative flow cytometry contour plots

1458   of the SGs, spleens and lungs showing endogenous CD45.2⁺ CD4⁺ T cells and adoptively

1459   transferred CD45.1⁺ M25 CD4⁺ T cells. **c)** Total numbers of M25 CD4⁺ T cell counts in the SGs

1460   and spleens one week post transfer into naïve or four weeks-infected B6 mice (n = 9 – 10 mice).

1461   **d)** Viral loads in the SGs, spleens and lungs at indicated time points post MCMV-GFP infection (n

1462   = 8 mice). **e)** Combined kinetics of SGs-infiltrating endogenous CD45.2⁺, adoptively transferred

1463   CD45.1⁺ M25 CD4⁺ T cells, and viral burden in the SGs (n = 7 – 9 mice). **f)** Percentage of PD-1⁺

1464   and CD69⁺ CD4⁺ T cells in the SGs (n = 9 mice). **g)** Percentage of CXCR3⁺ CD4⁺ T cells in various

1465   organs at day 8 post MCMV-GFP infection (n = 9 – 12 mice). **h)** Kinetics of viral loads in the SGs

1466   upon MCMV-3DR or MCMV-GFP infection (n = 8 – 9 mice). **i)** Percentage of Nur77GFP⁺ M25

1467   CD4⁺ T cells (left) and MFI of Nur77GFP on M25 CD4⁺ T cells (right) in SGs, spleens and lungs

1468   at day 8 and 14 post MCMV-3DR infection (n = 9 – 10 mice). Data in **a** and **c – i** are shown as

1469   mean + SD pooled from two independent experiments. Each symbol represents an individual

1470   mouse. Statistical significance was determined using single (**a and f**) or multiple (**c, g and i**)

1471   unpaired two-tailed t test. ****P<0.0001, ns = not significant.

1472

1473   .

1474

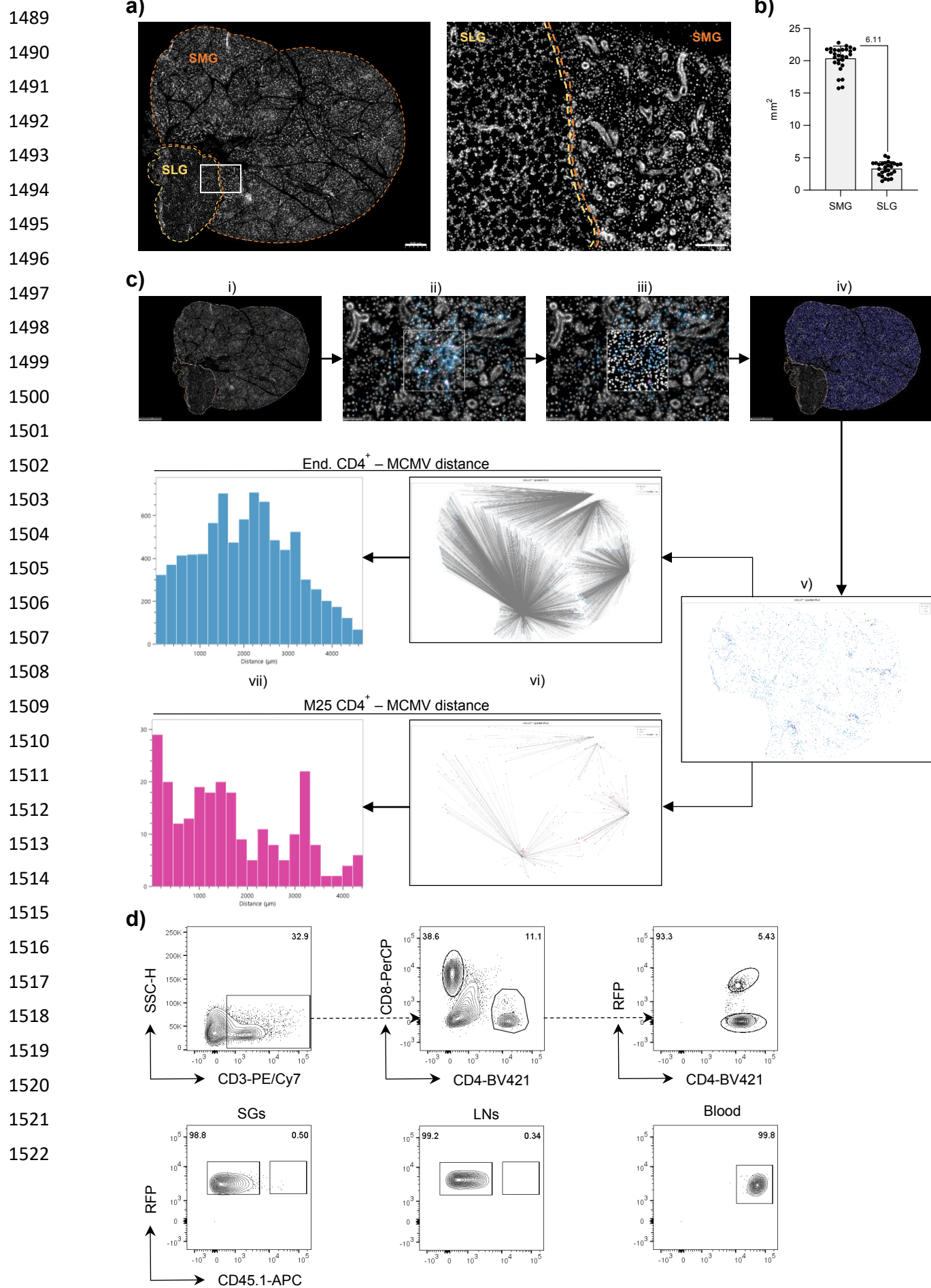1475

1476

1477

1478

1479

1480

1481

1482

1483

1484

1485

1486

1487

1488

Supplementary Figure 2

Supplementary Figure 2. Spatial localization of endogenous CD4$^+$ and M25 CD4$^+$ T cells in the SGs. **a)** Example of the right SG lobe with magnified region; perimeters of the submandibular and sublingual gland, SMG and SLG respectively, are indicated by dotted lines. **b)** Area of SMGs and SLGs. **c)** Image processing procedure: i) Tissue Annotation (i.e. SMGs and SLGs), ii) unmodified, original FOV within the SMGs and iii) after applying cell segmentation and phenotypic characterization (HighPlex FL module), iv) application of the HighPlex FL module to the whole annotation layer (i.e. SMGs), v) "Reduced" image consisting of extracted endogenous CD4$^+$ and M25 CD4$^+$ T cells from total cells together with infection foci, vi) Nearest neighbor analyses between endogenous CD4$^+$ or M25 CD4$^+$ T cells and infection foci and vii) representative histogram of overall distances between endogenous CD4$^+$ and M25 CD4$^+$ T cells and infection foci. **d)** I.v. labeling of M25 CD4$^+$ T cells in various organs. MACS purified, RFP expressing M25 CD4$^+$ T cells were adoptively transferred into naïve WT B6 one day prior MCMV-GFP infection. At day 8 post MCMV-GFP infection, 3 µg of anti-CD45.1 antibody was injected i.v. 3 min prior harvest. M25 CD4$^+$ T cells were identified by the RFP signal. Upper row: Gating strategy, lower row: Representative flow cytometry contour plots of SGs, SG draining LNs and blood. Plots are representative of n = 5 mice from one experiment. Scale bar in **b** = 500 µm (left) and 100 µm (right).

Supplementary Figure 3

CD4   GFP (Nur77)   CD8   MCMV

1558
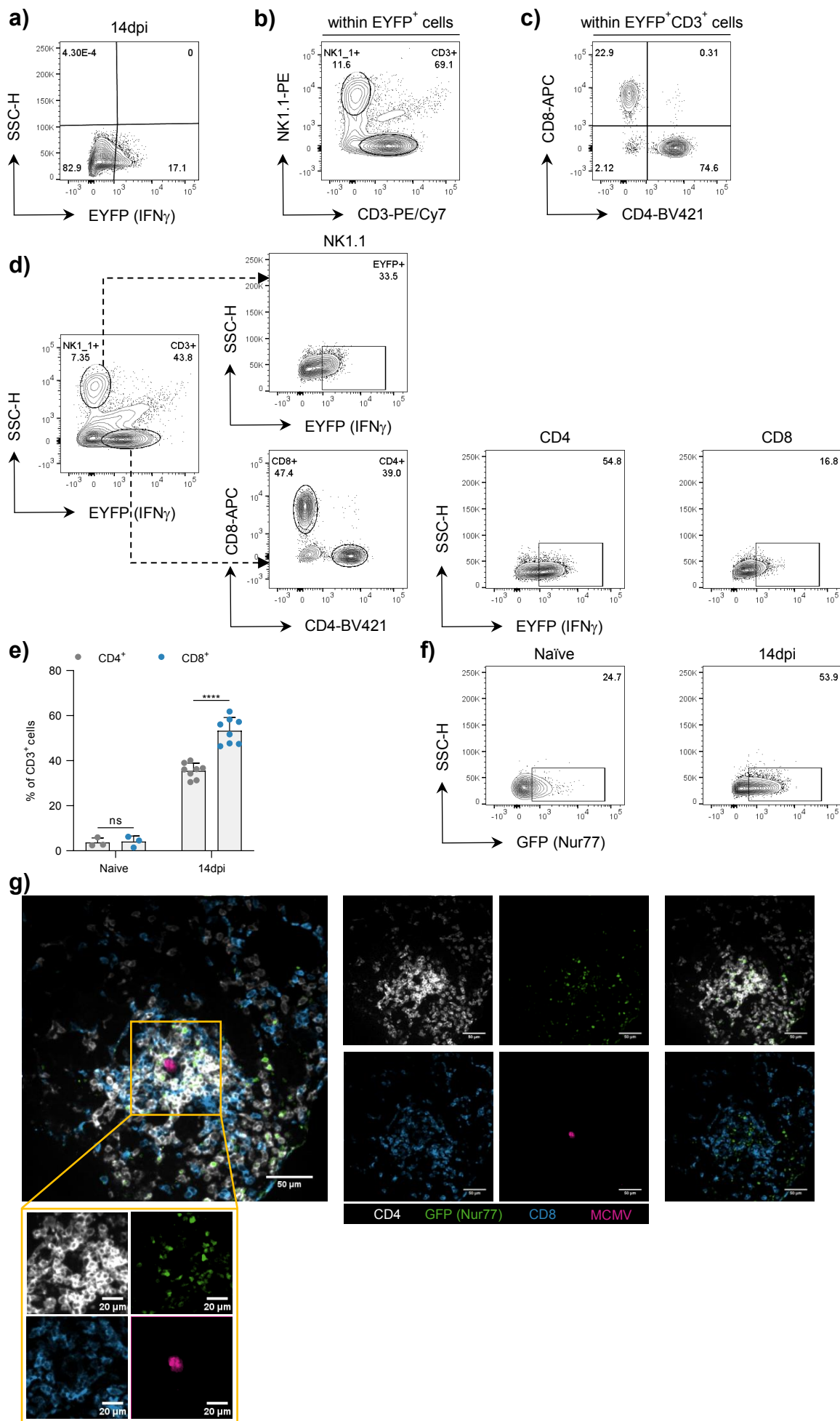
1559 **Supplementary Figure 3. IFNγ production by CD4$^+$ T cells in MCMV-3DR-infected SGs**. **a –**
1560 **c)** Representative flow cytometry contour plots showing gating strategy. **a)** Frequencies of EYFP$^+$
1561 cells upon MCMV-3DR infection. **b and c)** Further subgating of the EYFP$^+$ cell fraction. **d)**
1562 Representative flow cytometry contour plots of MCMV-3DR infected SGs showing gating strategy
1563 to determine the percentage of EYFP$^+$ cells within CD4$^+$, CD8$^+$ and NK1.1$^+$ cells. **e)** Percentage
1564 of CD4$^+$ and CD8$^+$ T cells within CD3$^+$ cells in naïve and MCMV-3DR infected Great mice. **f)**
1565 Representative flow cytometry contour plots of Nur77GFP expression in SG-residing CD4$^+$ T cells
1566 in naïve and MCMV-3DR infected Nur77GFP mice. **g)** Example of a four color FOV of a Nur77GFP
1567 mouse-derived SG 14 days post MCMV-3DR infection (left). Single color channel images (middle),
1568 merged two color CD4/GFP (right, upper row) and CD8/GFP (right, lower row) images. Magnified
1569 region (yellow frame) region split in four single color channel images. Data in **e)** are shown as
1570 mean + SD of n = 3 and n = 8 infected Great mice pooled from 2 independent experiments.
1571 Statistical significance in **e)** was determined using multiple unpaired two-tailed t test.
1572 ****P<0.0001, ns = not significant. Scale bar in **g** = 50 µm or 20 µm (magnified region).
1573
1574
1575
1576
1577
1578
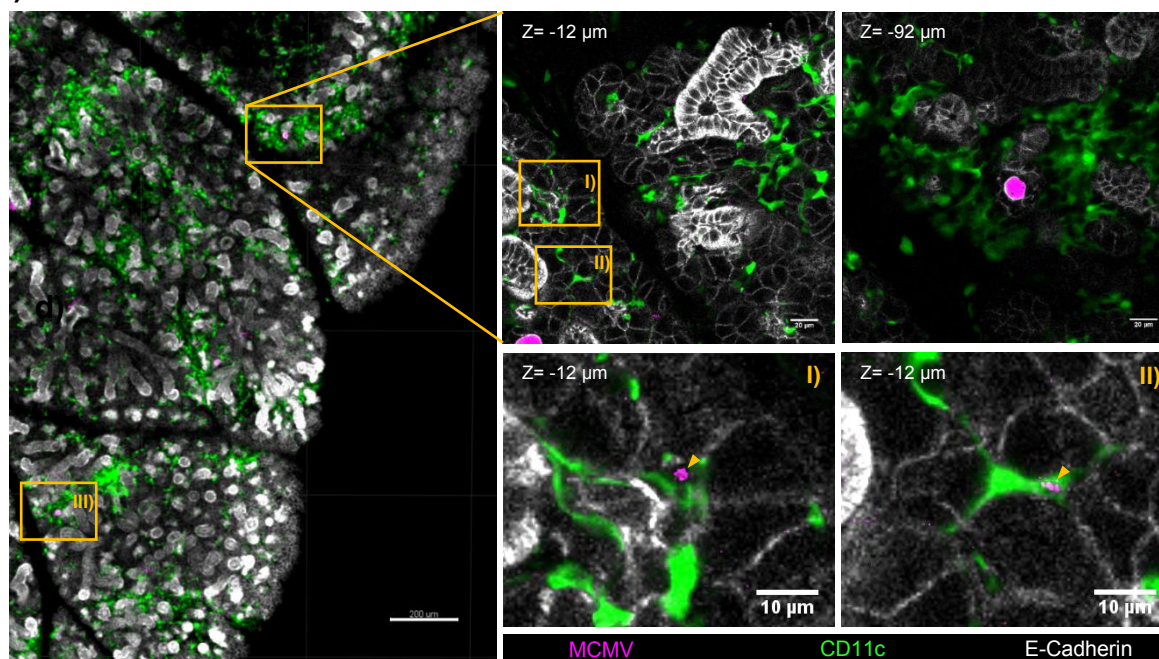1579
1580
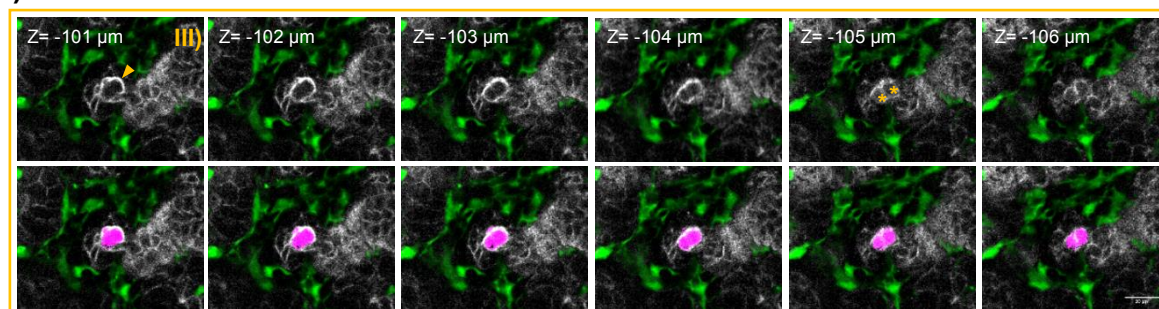1581
1582
1583
1584
1585
1586
1587
1588
1589
1590
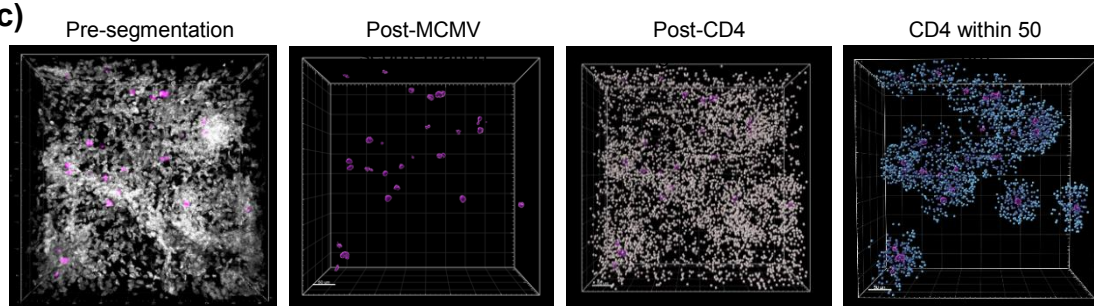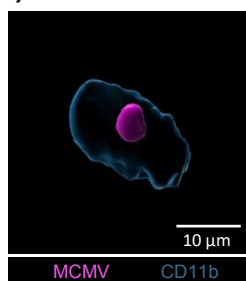1591
1592
1593

Supplementary Figure 4

1594

1595 **Supplementary Figure 4: Processing and assignment of MCMV-3DR signals in the SGs. a)**

1596 Example of a three color FOV of a CD11cYFP-Prox1morange mouse-derived SG 14 days post

1597 MCMV-3DR infection (left, scale bar = 200 µm) with magnified regions (right, scale bar = 20 µm

1598 (top) and 10 µm (bottom)) at indicated z-positions. **b)** Magnified region of **a** (yellow frame: III) at

1599 sequential z-planes without (upper row) and with (lower row) MCMV-3DR encoding mcherry signal

1600 (scale bar = 20 µm). Yellow arrowheads in **a** and **b** indicate engulfment of possible remnants of

1601 previously infected cells in CD11c^{+} cells and large actively infected E-Cadherin^{+} cells, respectively.

1602 Yellow asterisks in **b** show two neighboring MCMV-3DR infected E-Cadherin^{+} cells. **c)**

1603 Segmentation process for spatial analysis. From left to right: Unprocessed 3D reconstruction,

1604 post-segmentation of MCMV signal as surfaces, post-segmentation of the CD4 signal as spots

1605 and CD4^{+} T cells within 50 µm to next site of viral replication. Scale bar = 50 µm. **d)** 3D

1606 reconstructions of MCMV-3DR-associated mcherry signal within a CD11b^{+} cell 8 dpi. Scale bar =

1607 10 µm.

1608

1609

1610

1611

1612

1613

1614

1615

1616

1617

1618

1619

1620

1621

1622

1623

1624

1625

1626

1627

1628

Supplementary Figure 5
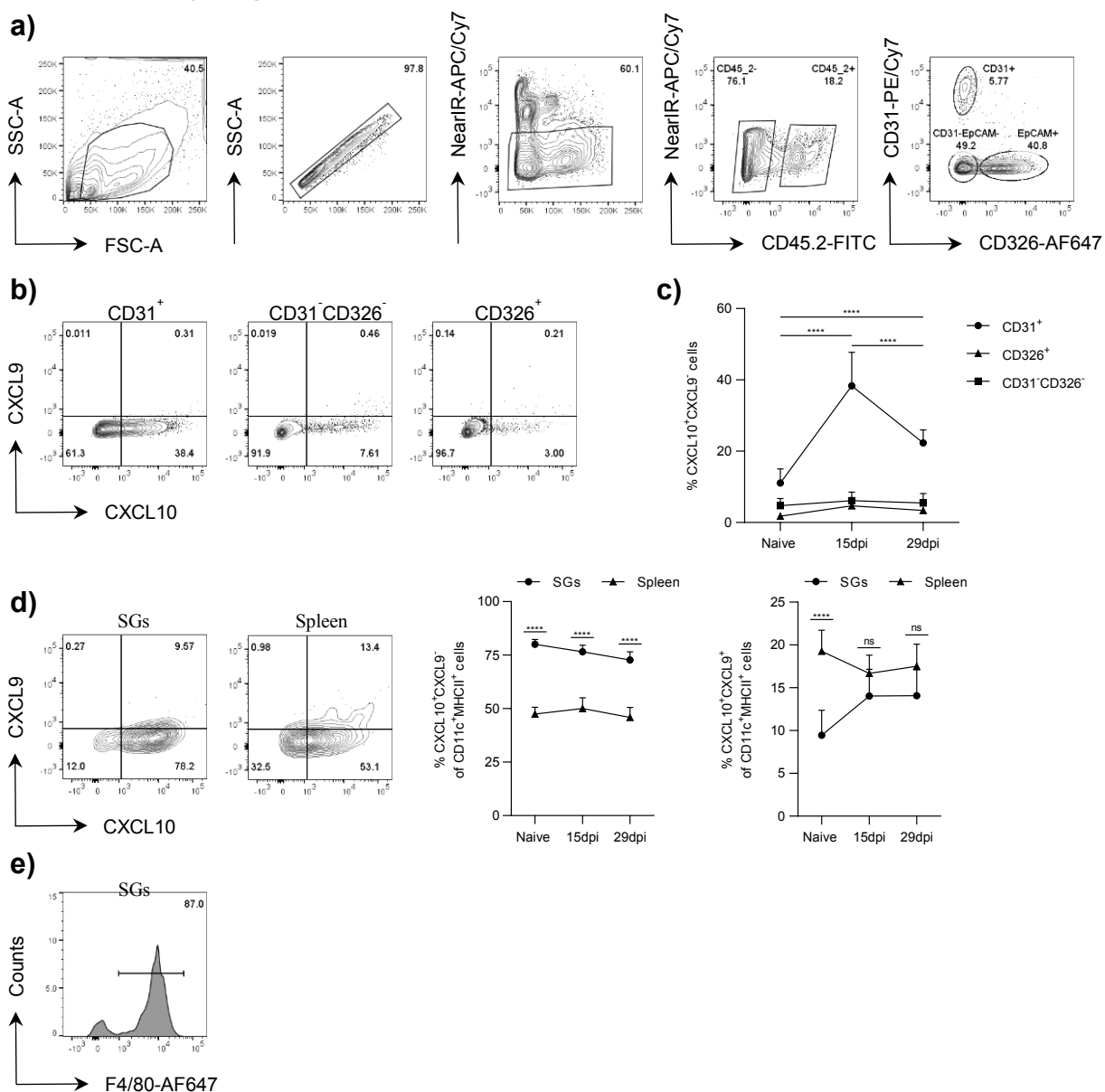
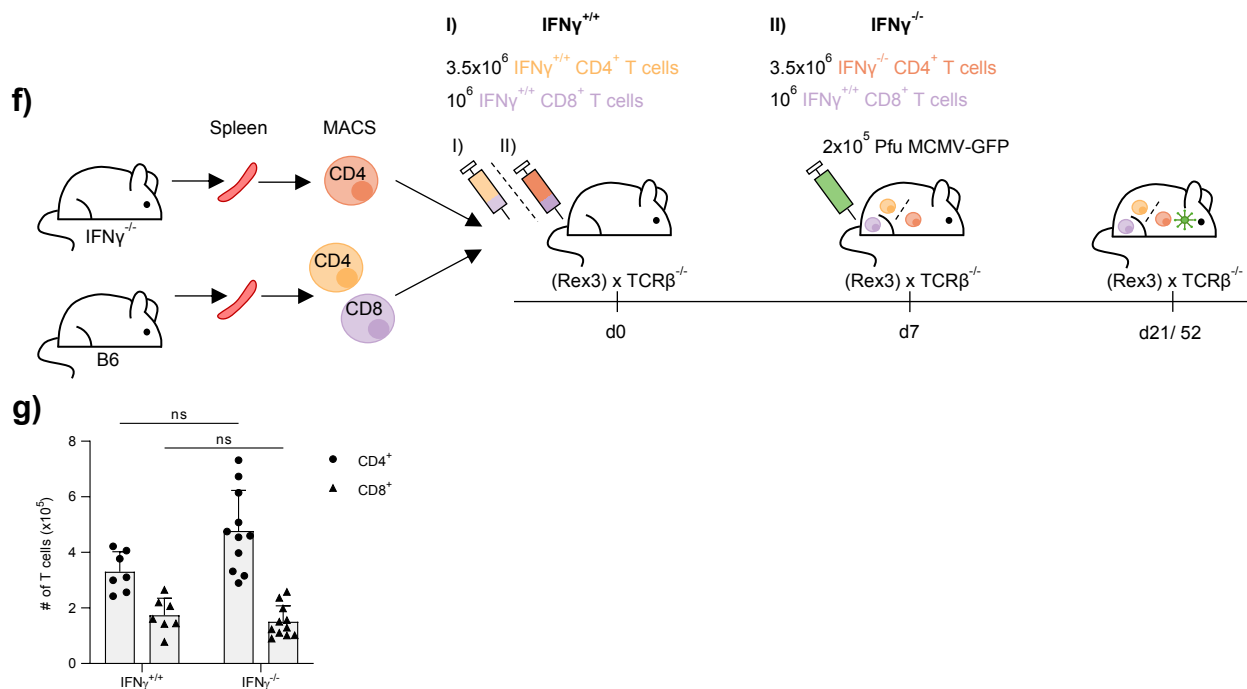**Supplementary Figure 5. CXCL9 and CXCL10 expression and their role in MCMV-infected SGs. a and b)** Representative flow cytometry contour plots showing gating strategy of non-hematopoietic cells **(a)** and CXCL9 and CXCL10 expression levels **(b)** in defined non-hematopoietic cell compartments 15 days post MCMV-GFP infection **c)** Percentage of indicated CXCL10$^+$ non-hematopoietic cells at indicated time points. **d)** Representative flow cytometry contour plots (left) and percentages (middle & right) of CXCL9 and CXCL10$^+$ CD11c$^+$MHCII$^+$ cells at indicated time points post MCMV-GFP infection in the SGs and spleen. **e)** Representative histogram of F4/80 expression levels in CD11c$^+$MHCII$^+$ cells of the SGs 15 days post MCMV-GFP infection. **f)** Experimental approach. T cells from spleens of naïve WT B6 (IFNγ$^{+/+}$) and IFNγKO (IFNγ$^{-/-}$) mice were purified using anti-CD4 or anti-CD8α MACS beads. 3.5x10^6 IFNγ competent (IFNγ$^{+/+}$) or IFNγ deficient (IFNγ$^{-/-}$) CD4$^+$ T cells and 10^6 IFNγ competent CD8$^+$ T cells were adoptively co-transferred into naïve Rex3 x TCRβ$^{-/-}$ or TCRβ$^{-/-}$ mice seven days prior MCMV-GFP infection. Flow cytometric and microscopic analyses of CXCL9 and CXCL10 expression were performed 14 dpi, viral burden was evaluated 14 and 45 dpi. **g)** Total numbers of CD4$^+$ and CD8$^+$ T cells in the SGs 14 dpi. Data in **c** and **d** are shown as mean + SD of n = 6 - 8 Rex3 mice pooled from two independent experiments. Each symbol in **c** and **d** represents the mean of pooled mice. Statistical significance was determined using 2-way Anova with post hoc Tukey's multiple comparisons test (**c**) or multiple unpaired two-tailed t test (**d & g**). ****P<0.0001, ns = not significant.
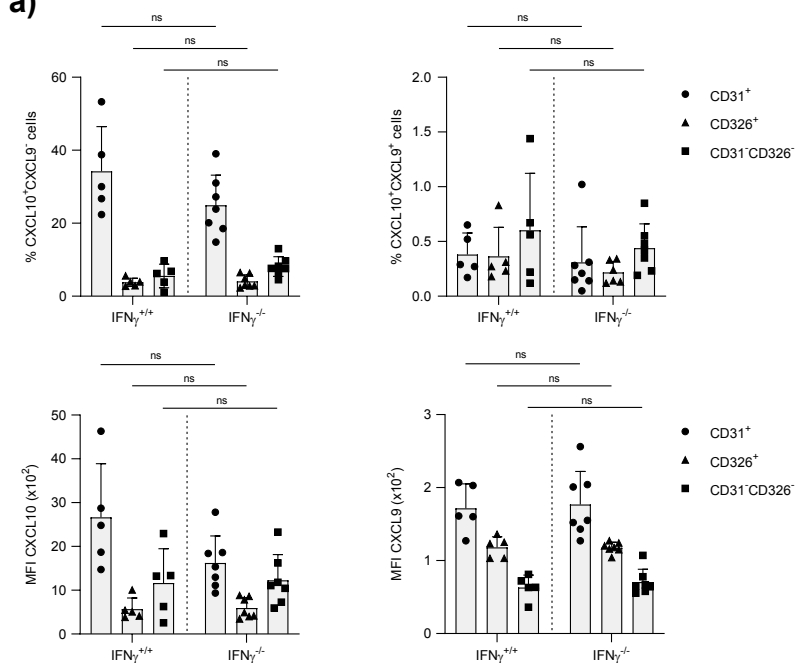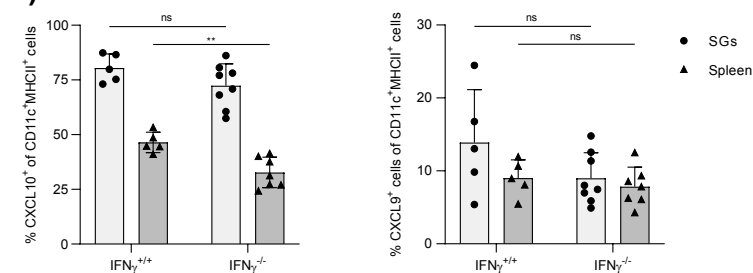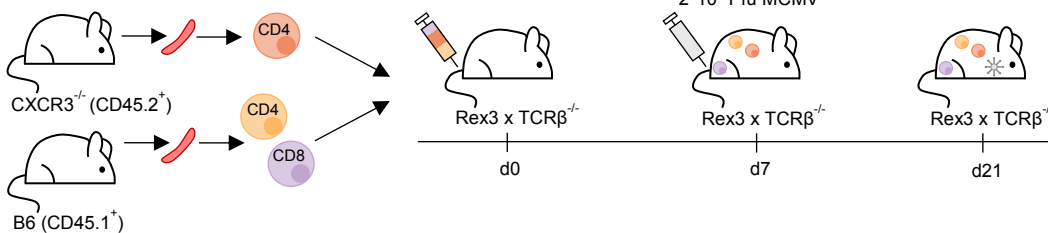
Supplementary Figure 6

1709 **Supplementary Figure 6. CXCR3-mediated recruitment of T cells to sites of CXCL9 and**
1710 **CXCL10 expression in MCMV-infected SGs. a)** Percentage (upper row) and MFI (lower row) of
1711 CXCL9 and CXCL10 expression in indicated non-hematopoietic cell types in the SGs 14 dpi. **b)**
1712 Percentage of CXCL9$^+$ and CXCL10$^+$ CD11c$^+$MHCII$^+$ cells in the SGs and spleen 14 dpi. **c)**
1713 Experimental approach. T cells from spleens of naïve WT B6 (CD45.1$^+$, CXCR3$^{+/+}$) and CXCR3$^{-/-}$
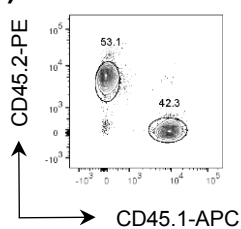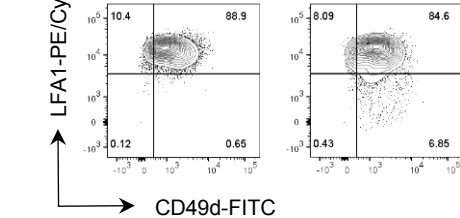1714 mice (CD45.2$^+$) were purified using anti-CD4 or anti-CD8α MACS beads. 3.*10^6 CXCR3
1715 competent (CD45.1$^+$CXCR3$^{+/+}$) and CXCR3 deficient (CD45.2$^+$CXCR3$^{-/-}$) CD4$^+$ T cells, together
1716 with CXCR3 competent CD8$^+$ T cells, were adoptively co-transferred into naïve Rex3 x TCR$\beta^{-/-}$
1717 mice seven days prior MCMV infection. Flow cytometric and microscopic analyses were performed
1718 14 dpi. **d)** Representative flow cytometry contour plots of CD45.1$^+$(CXCR3$^{+/+}$) and CD45.2$^+$
1719 (CXCR3$^{-/-}$) CD4$^+$ T cells and **e)** CD49d$^+$LFA-1$^+$ CD4$^+$ T cells in the SGs 14 dpi. Data in **a & b** are
1720 shown as mean + SD of n = 5 - 8 Rex3 x TCR$\beta^{-/-}$ mice pooled three independent experiments.
1721 Graphs in **d)** and **e)** are representative of n = 4 mice from one independent experiment.
1722 Each symbol in **a** and **b** represents an individual mouse. Statistical significance was determined
1723 using multiple unpaired two-tailed t test (**b**), or 2-way Anova with post hoc Tukey's multiple
1724 comparisons test (**c & d**). *P<0.05, ns = not significant.

1725
1726
1727
1728
1729
1730
1731
1732
1733
1734
1735
1736
1737
1738
1739
1740
1741
1742
1743

1744 **Supplementary Figure 7**

1745

1746 **a)** Cellular Potts Model

1747

1748 Cellular level

1749

1750 Viral concentration

1751

1752

1753 IFNγ concentration

1754

1755 CXCL9/CXCL10

1756

b) Individual Processes

1757 **c)** Cross section · Segmentation · Binarization · CPM

1758

1759

1760

1761

1762

1763 **d)** Extracell. Virus · Intracell. Virus   **e)** Endogenous CD4⁺ T cells · M25 CD4⁺ T cells

1764

1765

1766

1767

1768

1769

1770

1771 **f)** Arrest coefficient · Mean Inst. Velocity · Straightness   **g)** IFNγ-related MCMV reduction

1772

1773

1774

1775

1776

1777

Supplementary Figure 7. Mathematical modeling of viral-immune interactions in the SGs.
a) Sketch of the structure of the multi-scale cellular Potts model used to simulate viral-immune interaction in the SMG. Different interconnected layers account for the spatiotemporal dynamics of individual cells in interaction with CXCL9/CXCL10, IFNγ, and extracellular MCMV concentrations. **b)** Individual processes considered within the CPM that describe the turnover and infection of epithelial cells, intracellular viral replication, as well as the motility and stimulation of CD4$^+$ T cells, and diffusion of virus and IFNγ. Individual parameters are explained in detail within the **Supplemental Information - Text S1**. **c)** Representation of the ductal structure within the simulations by using 800×800 μm^2 areas selected from SMG cross section images that were segmented to distinguish ductal cells (*red*), M25 (*blue*) and endogenous (*green*) CD4$^+$ T cells, cell free areas (*yellow*), and remaining cells (purple) using *HALO* and *ilastik* software. Segmented images were converted to binary images to distinguish between ductal (*white*) and non-ductal (*black*) areas, with non-ductal areas later populated by epithelial cells within the CPM. **d)** Experimental data digitalized from (Misra et al., 1977) and best fit to describe MCMV viral replication dynamics based on Eq. (8). **e)** Infiltration dynamics of endogenous (upper panel) and M25 CD4$^+$ T cells (lower panel) using Eq. (9) and experimental data (see **Text S1**). **f)** CD4$^+$ T cell motility dynamics as predicted by fitting the CPM to the data of (Stolp et al., 2020) on CD8$^+$ T cell dynamics in the SG. The distributions of the arrest coefficient, mean instant velocity and straightness for the data (*blue*) and model predictions (*cyan*) following 300 T cells over 1h are shown, with model predictions based on the best parameterization obtained by the FitMultiCell approach. **g)** Dose-response curve for the effect of IFNγ on MCMV replication efficiency parameterized based on Eq. (10) and the data of (Lucin et al., 1994). Panels **(d)**, **(e)**, and **(g)** indicate experimental data (*black dots*), best model fits (*red line*) and 95%-prediction bands (*red shaded area*). All individual parameter estimates are shown in **Text S1**.

1812   **Supplementary Video 1. 3D visualization of CD4$^+$ T cells and MCMV-3DR-associated**

1813   **mcherry signals (sites of viral replication and small remnants).** 3D reconstruction of CD4$^+$ T

1814   cells (white) and MCMV-3DR-associated mcherry signals (magenta) in the SMG at 8 dpi. Small

1815   mcherry volumes represent remnants or apoptotic bodies and large mcherry volumes sites of

1816   infectious virus production.

1817

1818   **Supplementary Video 2. Quantitative analysis of CD4$^+$ T cells within 50 µm to each MCMV-**

1819   **3DR-associated mcherry signal.** Successive 3D processing of mcherry-expressing MCMV-3DR

1820   (magenta) as surfaces and CD4$^+$ T cells (white) as spots with further thresholding of these spots

1821   within 50 µm (cyan) to each MCMV-3DR-associated mcherry signal in the SMG. Major tick

1822   intervals = 50 µm.

1823

1824   **Supplementary Video 3. *Ex vivo* live imaging of CD11c$^+$ cell phagocytosing MCMV-3DR-**

1825   **derived small remnants.** Times series of CD11c$^+$ cell (green) phagocytosing surrounding MCMV-

1826   3DR-associated remnants (magenta) at 9 dpi. Scale bar = 3 µm. Time in hours: minutes: seconds:

1827   milliseconds.

1828

1829   **Supplementary Video 4. 3D reconstruction of accumulating CD11c$^+$ cells and CD4$^+$ T cells.**

1830   3D processing of MCMV-3DR-associated mcherry signals (magenta), CD4$^+$ T cells (white) and

1831   CD11c$^+$ cells (green) as surfaces in the SMG at 14 dpi. Zoom-in on small remnants within CD11c$^+$

1832   cells.

1833

1834

1835

1836

1837

1838

1839

1840

1841

1842

1843

1844

1845

1846 **Supplemental Information Text S1-**

1847

1848 **Mathematical model of MCMV infection and immune dynamics in the**
1849 **salivary glands**

1850 We developed a multi-scale mathematical model to study the spatiotemporal dynamics of MCMV
1851 infection and CD4$^+$ T cell dynamics in the salivary glands (SG). The model follows the dynamics
1852 and fate of individual cells while accounting for intra- and extracellular processes, such as
1853 intracellular viral replication and extracellular viral diffusion, respectively. It is built as a cellular
1854 Potts Model (CPM) using the software Morpheus (http://morpheus.gitlab.io;(Starruss et al., 2014)),
1855 which provides a 2D-representation of the observed tissue structure and accounts for individual
1856 cell morphology, motility and their spatial location. A CPM is a lattice-based model with individual
1857 cells defined by several connected lattice sites (Glazier and Graner, 1993; Graner and Glazier,
1858 1992). Each cell is characterized by a specific cell type, as well as a unique identifier w and the
1859 position within the grid, (*i,j*). The motility and dynamics of individual cells is then determined by
1860 stochastic events that regulate the interaction between grid sites (Glazier and Graner, 1993). Our
1861 model considers the turnover and infection of epithelial cells, the diffusion and clearance of
1862 extracellular virus, as well as the infiltration, migration and locally confined release of IFNγ of
1863 endogenous and M25-specific CD4$^+$ T cells. A sketch of the model and its structure is shown in
1864 **Figure S7a,b**. A detailed description of the individual model components, as well as their
1865 parameterization based on own experimental data and data from the literature is given in the
1866 following.

1867

1868 **The multi-scale mathematical model**

1869 **Epithelial cells and viral replication**

1870 The multi-scale model provides a 2D-representation of the tissue structure of the submandibular
1871 salivary glands (SMG) as observed in the experimental cross sections. Epithelial cells, which form
1872 the structure of the solid tissue, are immobile, and die and proliferate with probability p_λ and p_d,
1873 respectively. Hereby, p_λ is defined by

1874
$$p_\lambda = 1 - \exp\left(-\lambda\left(1 - \frac{N}{N_{max}}\right)\right) \qquad (1)$$

1875 with λ defining the maximal proliferation rate, N_{max}, the maximal cell density and N the current
1876 number of epithelial cells to ensure tissue homeostasis in response to cell turnover or tissue
1877 damage. Uninfected epithelial cells, i.e., target cells, get infected by MCMV dependent on the viral
1878 concentration, V, at the location of the cell. The probability of infection, p_β, is given by

1879

1880
$$p_\beta = 1 - \exp(-\beta V) \qquad (2)$$

1881 Hereby, the parameter β defines a scaling factor, which determines transmission of infection
1882 dependent on the extracellular viral concentration. Upon infection, epithelial cells will double in

1883   size (Munger et al., 2006) and start replication of intracellular viral RNA, R, which is modeled by a
1884   system of ordinary differential equations following logistic-growth with

1885

$$\frac{dR}{dt} = \begin{cases} \alpha_R R \left(1 - \dfrac{R}{R_{max}}\right) - \rho_R R & \text{during active viral replication} \\ -c_R R - \rho_R R & \text{after stop of viral replication} \end{cases} \tag{3}$$

1886   Hereby, R_{max} defines the maximal carrying capacity of the cell, and α_R, ρ_R and c_R the net-
1887   replication, viral export and intracellular viral clearance rate, respectively. The stop of viral
1888   replication, as e.g. mediated by IFNγ, is represented by the switch to the second case in Eq. (3)
1889   in which the virus gets degraded with rate c_R and is continued to be exported until intracellular
1890   virus vanishes (see also (Rand et al., 2012)). As MCMV suppresses cell cycle progression
1891   (Marcinowski et al., 2012), cell division of infected cells is not considered within the simulations,
1892   while death occurs with probability p_δ.
1893   Once exported, extracellular virus diffuses through the tissue with diffusion coefficient D_V. Thus,
1894   the concentration of extracellular virus is modeled by a reaction-diffusion system given by

1895

$$\frac{\partial V}{\partial t} = D_V \nabla^2 V + f(V)$$
$$f(V) = \frac{dV_{ij}}{dt} = \rho_R R_{ij} - c_R V_{ij} \tag{4}$$

1896   Hereby, $f(V)$, describes viral export, ρ_R, and viral degradation, c_R, at each specific lattice site (i,j)
1897   within the grid, with $R_{ij} = 0$ for all lattice sites that belong to uninfected cells. To determine the
1898   probability of an uninfected cell, ω, to get infected (Eq. (2)), the viral concentration is averaged
1899   over all lattice sites that belong to the uninfected cell, i.e, $V_\omega = 1/|\omega| \sum_{(i,j) \in \omega} V_{ij}$.
1900   Local concentrations of IFNγ can inhibit viral replication in infected cells with probability
1901 $p_{IFN\gamma}$ defined by

1902

$$p_{IFN\gamma} = 1 - \exp(-g(IFN)) \tag{5}$$

1903   with $g(IFN)$ determining the dose-response relationship for IFNγ given by

1904

$$g(IFN) = \frac{y_{max}}{1 + \left(\dfrac{ED_{50}}{IFN}\right)^n} \tag{6}$$

1905   Hereby define y_{max} the maximal inhibition efficacy, ED_{50} the effective dose at which 50% of cells
1906   are inhibited, and n a Hill-coefficient. Upon inhibition of intracellular viral replication, the
1907   concentration of intracellular viral RNA will follow the second case of Eq. (3). As the effect of IFNγ
1908   on the replication rate of MCMV infected cells was shown to be reversible (Kropp et al., 2011;
1909   Presti et al., 1998), infected cells can loose the replication inhibition without maintained IFNγ
1910   signaling. An infected cell is considered as an active, MCMV replicating cell (MCMV^{+}) and, thus,
1911   visible by light microscopy, if the intracellular viral load R is larger than a threshold of 100 (R>100).
1912
1913

1914

CD4⁺ T cells and IFNγ release

1915

1916 In contrast to epithelial cells, endogenous and M25 CD4⁺ T cells are considered as motile cells
1917 that enter and leave the tissue with time-dependent influx and efflux rates, σ_{in} and σ_{out}. Within the
1918 tissue, CD4⁺ T cells follow persistent motion modeled with persistent strength s_T and decay time
1919 τ_T. The movement of CD4⁺ T cells can be influenced by chemokine fields, e.g. CXCL9 and
1920 CXCL10 chemotactic gradients as mediated by antigen presenting cells (APC). The attraction of
1921 cells is defined by the chemotactic strength, CTX, that determines the strength at which the
1922 gradient can deviate the direction of the CD4⁺ T cell. Stimulation of CD4⁺ T cells leading to release
1923 of IFNγ depends on interaction of CD4⁺ T cells with APC or infected cells dependent on the
1924 scenario (see below). When stimulated, the CD4⁺ T cell becomes temporally immobile and will
1925 secrete IFNγ with rate σ_{IFN}. Analogously to the extracellular virus, the dynamics of the IFNγ
1926 concentration within the system is then described by

1927
$$\frac{\partial IFN}{\partial t} = D_{IFN}\nabla^2 IFN + f(IFN)$$
$$f(IFN) = \frac{dIFN_{ij}}{dt} = \rho_{IFN}IFN_{ij} - c_{IFN}IFN_{ij}$$
(7)

1928
1929 Hereby, D_{IFN} defines the 2D-diffusion coefficient of IFNγ, and $f(IFN)$ describes the release, ρ_{IFN},
1930 and extracellular clearance, c_{IFN}, of IFNγ at each specific lattice site *(i,j)*. To calculate the
1931 probability of inhibiting viral replication in infected cell ω_I according to Eq. (3) and (4), the IFNγ
1932 concentration is averaged over all lattice sites that belong to an infected cell, i.e., $IFN =$
1933 $1/|\omega_I|\sum_{(i,j)\in \omega_I} IFN_{ij}$.

1934

1935 # Parameterization and Model adaptation

1936 The individual components and processes of the model were parameterized based on own
1937 experimental data and data from the literature. For some of the processes where reliable
1938 measurements are missing, parameter sweeps were performed with model results challenged
1939 against the experimental data to evaluate reasonable parameterizations. Sensitivity of results with
1940 regard to selected parameter combinations were performed.

1941

1942 **SGM tissue structure**

1943 Recapitulation of the tissue structure was achieved by segmenting microscopy images of cross
1944 sections of the SMG using Ilastik Version1.3.3.pos3 (https://www.ilastik.org, (Berg et al., 2019)).
1945 Duct structures were extracted as binary masks and loaded as background into Morpheus. The
1946 images were then populated by immobile epithelial cells representing acinar glandular epithelial
1947 cells as the main target cells for MCMV (Fox, 2006; Walton et al., 2011). Duct areas were left
1948 empty (**Figure S7c**). The spatial localization of immune and infected cells was measured on 20-
1949 22 □m² cross sections, which is an unfeasible system size for the simulations. For computational
1950 efficiency, only small sections of 800×800 μm² of the SMG tissue were considered, with the
1951 actually observed 2D-tissue cross sections being 31-34-fold larger (e.g. ~20-22 mm²). Simulations
1952 were run with a scaling factor of 1 pixel (px) = 2 μm to allow simulation of larger areas. The cell

1953 area of target and infected cell was determined using microscopy images of the SG cross sections
1954 with labelled MCMV-GFP infected cells. The average diameter of infected cells was determined
1955 as ~17.54 μm leading to an average area of 241.6 μm². Target cells, i.e., uninfected epithelial
1956 cells, were set to half of the area of infected cells (Kwak et al., 2016; Munger et al., 2006), i.e.,
1957 120.8 μm² **(Table A)**.
1958 At the beginning of a simulation, ~2500 target cells were initialized within the grid defining the
1959 maximal population capacity of the system N_{max}. This corresponds to the average area of ~46%
1960 that was covered by non-immune and non-duct cells within the observed cross sections. With
1961 epithelial cells usually having a relatively long lifespan of 2-4 months (Aure et al., 2015; Schwartz-
1962 Arad et al., 1988), the probability of uninfected epithelial cells to die, p_d, is Γ-distributed with scale
1963 and shape parameters determined by k_T=40 and θ_T=55 leading to an expected lifespan of ~3
1964 months. With MCMV-infected cells observed to remain viable for 36-48h (Fox, 2006) cell death of
1965 infected cells, p_δ, was modeled analogously according to $\Gamma(k_l = 0.25, \theta_l = 170)$.

1966

1967 **Intracellular viral replication**

1968 The dynamics of intracellular viral replication and export as described in Eq. (3) was parameterized
1969 using *in vitro* experimental data on the viral synthesis in MCMV infected mouse embryo fibroblasts
1970 (MEF)(Misra et al., 1977)**.** In this experiment, MEFs in cell culture were infected with MCMV and
1971 the number of genome equivalents and pfu per cell were determined at frequent time points in
1972 between 0 and 22 hours post infection **(Figure S7d)**. The data allowed us to simultaneously
1973 estimate the net-viral replication rate, α_R, extracellular viral degradation, c, and viral export, ρ_R,
1974 using a single coherent data set. To analyze the data and estimate these parameters, the system
1975 in Eq. (3) was extended by

$$
\begin{aligned}
\frac{dR}{dt} &= \begin{cases} \alpha_R R \left(1 - \frac{R}{R_{max}}\right) - \rho_R R & \text{during active viral replication} \\ -c_R R - \rho_R R & \text{after stop of viral replication} \end{cases} \\
\frac{dV_1}{dt} &= -cV_1 \\
\frac{dV_2}{dt} &= \rho_R R - cV_2
\end{aligned}
\tag{8}
$$

1976

1977 which distinguishes between the extracellular viral load applied to the system at the start of the
1978 experiment, V_1, and the newly produced virions by the infected cells, V_2. Eq. (8) was fitted to the
1979 data using $V = V_1 + V_2$. Based on these analyses we estimated a net viral replication rate of α_R=
1980 0.41 h⁻¹ (0.38, 0.49), a maximal carrying capacity of R_{max}= 1060 genome equivalents (1020,
1981 1260), a viral export rate of ρ_R= 0.03 pfu/gen. equivalent h⁻¹ (0.02, 0.11) and a viral degradation
1982 rate of c = 0.45 h⁻¹ (0.20, 1.65), with numbers in brackets indicating 95%-confidence intervals of
1983 estimates. As the rates of intracellular viral replication and degradation could not be determined
1984 separately based on these experimental data, the rate of intracellular RNA degradation, c_R, was
1985 set to the extracellular degradation rate, $c_R = c$. The experimental data with model predictions and
1986 all parameter estimates are shown in **Figure S7d** and **Table A**, respectively. For technical details
1987 on the fitting procedure please see section ***Parameter fitting and estimation procedures***. While
1988 the model predicts saturation of the viral concentrations ~24 h corresponding to the assumed

1989   length of the replication cycle of MCMV (Misra et al., 1977), it slightly underestimates the lag time
1990   before the start of rapid viral replication leading to earlier viral export.

1991

1992   **MCMV spread and cell proliferation**

1993   There are three factors that influence the degree and extend of MCMV spread and tissue
1994   pathology within the salivary glands in the absence of any immune response: This includes (i) viral
1995   spread, as defined by the scaling factor β regulating the infection probability, p_β, dependent on
1996   the extracellular viral concentration, V (Eq. (2)), (ii) extracellular viral diffusion defined by the
1997   diffusion coefficient D_V (Eq. (4)), and (iii) tissue regeneration determined by the cell proliferation
1998   parameter λ (Eq. (1)). Individual assessment of the parameters β and λ is generally difficult due
1999   to their strong interdependency and the lack of appropriate experimental data. Therefore, we
2000   performed combined sweeps of β and λ to identify appropriate parameter combinations. Model
2001   simulations without the presence of immune responses were challenged against the following
2002   observations and assumptions to restrict parameter values:

2003   1.) As our data indicate high infection levels at 8 dpi, parameter β should be chosen to allow
2004   a considerable spread of the infection within the tissue already at 8 dpi. This is used to set
2005   a lower bound for β.

2006   2.) Even without the presence of CD4^{+} T cell immunity, we assumed that the virus is incapable
2007   of leading to the complete lysis of large tissue sections at 8 dpi. These comparisons
2008   allowed us to determine an upper boundary to β and a lower bound to λ.

2009   3.) MCMV indicates local spread within tissue (Wirtz et al., 2008) leading to infectious foci.
2010   This observation was used to balance the relationship between β and D_V that regulates
2011   the extent of viral spread.

2012   Previous measurements indicate a viral diffusion coefficient for MCMV in between D_V = 4.4 μm^2/s
2013   - 6.4 μm^2/s (Dick et al., 2015). However, given the long time period (~60 days) required for our
2014   simulations, we used an effective viral diffusion coefficient of D_V^{eff} = 64 μm^2/h in our model, which
2015   resulted in locally confined virus fields around the infected cell. As the choice of D_V^{eff} is
2016   compensated by the choice of the unknown scaling parameter β, this does not affect our analyses,
2017   but substantially increases computational efficiency. Otherwise simulation time would increase by
2018   ~100-fold, making it unfeasible for our analyses. Accounting for the observations in (1.) - (3.)
2019   mentioned above, we finally set λ= 0.204 h^{-1} and β= 1.5×10^{-3} pfu^{-1}h^{-1} to scale tissue regeneration
2020   and infection spread in our simulations. With these parameters we obtained preferential local
2021   spread of the infection as observed in (Wirtz et al., 2008), but also seeding of new infections at
2022   distant locations due to viral diffusion. In general, the maintenance of the tissue, as well as the
2023   dynamics of infection was sensitive to the choices of λ and β. More detailed measurements will
2024   be needed to appropriately curtail both values for future analyses.

2025

2026

CD4⁺ T cell infiltration dynamics

In agreement with the experimental data, our model distinguishes between endogenous and M25 CD4⁺ T cells. Both cell types are modeled with a targeted T cell area of ~50 μm^2 corresponding to a T cell diameter of ~8 μm which is at the lower bound of average T cell sizes.

To parameterize the infiltration dynamics of CD4⁺ T cells into the SMG during the time course of the infection, we used our experimental measurements. The numbers of endogenous and M25 CD4⁺ T cells were determined at 0, 8, 14 and 30 dpi for the total SMG, and for specified cross sections at 8 dpi. Based on the ratio of CD4⁺ T cells on the cross sections and the total SMG at 8 dpi, we calculated the expected density of endogenous and M25 CD4⁺ T cells in a defined area of 800×800 μm^2 as used for our simulations **(Table B)**. The population dynamics of CD4⁺ T cells in the SMG can then be described by the following system of ordinary differential equations to determine the net-flux and loss of cells in and out of the SMG,

$$\frac{dE}{dt} = -\sigma_{in}E$$
$$\frac{dT}{dt} = \sigma_{in}E - \sigma_{out}T$$

(9)

Hereby, *E* and *T* define the concentration of CD4⁺ T cells outside and within the SMG, respectively, and σ_{in} and σ_{out} the rate of influx and loss of cells. Eq. (9) was fitted separately for endogenous and M25 CD4⁺ T cells based on the experimental data shown in **Table B**. Best fits and 95%-confidence intervals are shown in **Table A** with experimental data and model predictions shown in **Figure S7e**. All parameters for endogenous cells were identifiable, while low cell counts slightly impaired parameter identifiability for M25 CD4⁺ T cells.

The estimates were then used to parameterize the appearance and loss of endogenous and M25 CD4⁺ T cells in our CPM. At each time step, a total number of $\sigma_{in}E(t)$ cells was randomly placed on the grid to simulate CD4⁺ T cell infiltration. In addition, a CD4⁺ T cell was removed from the tissue with probability $p_{out} = 1 - \exp(-\sigma_{out})$. For technical reasons, CD4⁺ T cells were initialized at the positions of ductal structures and moved into the tissue from these points of entry. To guide this process, a gradient from the center to the borders of the duct structures was introduced. CD4⁺ T cells moved against the gradient and into the tissue with a chemotactic strength set to $CTX_{duct} = 1$, which resulted in a homogeneous distribution of the CD4⁺ T cells in the grid. Larger values would result in strong borders between the acinar and ductal areas and inhomogeneous distribution of the CD4⁺ T cells over the grid.

CD4⁺ T cell motility within the SMG

Parameters to describe CD4⁺ T cell motility within the SMG were determined using data from two-photon intravital microscopy analyses on the dynamics of CD8+ T cells in the SMG during lymphocytic choriomeningitis virus infection (Stolp et al., 2020) assuming similar motility characteristics of both cell types. T cells were observed to move in the SMG with an average speed of 6.8 $\mu m/min$, a top speed of 18 $\mu m/min$ and were characterized with a low arrest coefficient (Stolp et al., 2020). Thus, these data indicate a fast motion with rare motility arrest and frequent direction changes.

2065 Cell motility of CD4$^+$ T cells was implemented in Morpheus using persistent motion, which is
2066 described by the persistence strength, s_T, and the decay time τ_T, defining the weight and the
2067 maintenance with which a cell pursues a specific target direction, respectively. The parameters
2068 were estimated using the FitMultiCell-pipeline (https://fitmulticell.gitlab.io) with simulations
2069 following 300 CD4$^+$ T cells over a time period of 1h. Best estimates revealed a persistence strength
2070 of s_T =180 and decay time of τ_T =8.9 min assuming no deviation by chemotactic gradients (CTX=0).
2071 With these parameters, simulated T cell motility dynamics showed similar mean velocities and
2072 distribution of arrest coefficients, but constrained maximal velocities and higher straightness than
2073 observed in the experimental data (**Figure S7f**). These deviations are affected by the chosen
2074 temporal and spatial discretization of the simulation environment. Decreasing the time step size
2075 of the model would improve parameter fitting but substantially affects computational run time of
2076 the model. However, given the level of detail aimed for in our analyses, CD4$^+$ T cell motility was
2077 sufficiently represented by the parameterization shown above.

2078

CD4$^+$ T cell stimulation, IFNγ dynamics and CXCL9/CXCL10 gradients

2080 Within the SMG, CD4$^+$ T cells can get stimulated to release IFNγ, which inhibits viral replication
2081 within infected cells. In our simulations we distinguish between two scenarios of CD4$^+$ T cells
2082 stimulation: (i) without and (ii) with the consideration of antigen presenting cells (APC). In a
2083 scenario without the consideration of APC, CD4$^+$ T cells are stimulated by the direct contact with
2084 antigen, i.e., infected cells. The probabilities of endogenous and M25 CD4$^+$ T cells to get
2085 stimulated, $p_{se} = 1 - \exp(-\lambda_{se})$ and $p_{sm} = 1 - \exp(-\lambda_{sm})$, respectively, were adjusted using
2086 previous observations from the literature(Verma et al., 2016). Assessing the percentage of IFNγ
2087 secreting CD4$^+$ T cells at 8 days post MCMV infection within various organs, Verma et al. (Verma
2088 et al., 2016) measured that 8 to 15% of CD4$^+$ T cells, and 15-30% of epitope-specific cells were
2089 IFNγ$^+$. To broadly reflect these dynamics, parameters λ_{se}= 0.05 h^{-1} and λ_{sm} =0.15 h^{-1} were chosen.
2090 With this parameterization, we observed that 14.4 ± 5.17 % and 29.1 ± 12.1 % (mean ± SD of 10
2091 replicates) of CD4$^+$ and M25 CD4$^+$ T cells, respectively, were IFNγ$^+$ within our simulations (e.g.
2092 Figure 7 in the main manuscript), which is at the upper end of the observed intervals.

2093 ***APC related activation:*** In the second scenario, we considered the additional effect of APC on
2094 CD4$^+$ T cell motility dynamics and stimulation. APCs are suggested to have a macrophage-like
2095 phenotype that present MCMV-antigen after phagocytosis of apoptotic remains of infected cells
2096 (Walton et al., 2011). Therefore, in our model APCs were simulated as an additional layer with
2097 grid sites APC_{ij} (**Figure S7a**). The death of infected cells can lead to local antigen presentation,
2098 i.e., APC_{ij} = 1, at the grid site corresponding to the location of the infected cell. As infected cells
2099 tend to be close to each other and one APC might take up signals from different infected cells in
2100 the surrounding, only one out of three infected cells would on average result in antigen
2101 presentation. To represent CXCR3 guided motion, APCs are assumed to produce a local gradient
2102 of CXCL9/CXCL10 signaling that attracts CD4$^+$ T cells. Different parameters were tested to define
2103 the chemotactic strength CTX_{APC} at which CD4$^+$ T cells will move along this gradient. With values
2104 of $CTX_{APC} = 10$ and $CTX_{APC} = 100$ resulting in rare or recruitment of almost all CD4$^+$ T cells to the
2105 specific APC, CTX_{APC} was set to 50. Upon contact with an APC, CD4$^+$ T cells are stimulated with
2106 the same probabilities p_{se} and p_{sm} as before.

2107　*IFNγ release:* As CD4⁺ T cell motility is observed to be temporarily reduced after contact to an
2108　antigen (Honda et al., 2014), CD4⁺ T cells will stop their movement upon stimulation for on average
2109　of ~42h, which corresponds to the lifetime of infected cells. The stopping time is therefore
2110　randomly determined by $\Gamma(k_l = 0.25, \theta_l = 170)$. During their immobility, cells will secrete IFNγ for a
2111　confined time period, which was set to 2.5 h according to previous observations (Gao et al., 2014).
2112　Similar as for the viral concentration and infection spread, the effective range of IFNγ is regulated
2113　by the diffusion coefficient for IFNγ D_{IFN}, the secretion rate ρ_{IFN}, as well as the clearance rate,
2114　c_{IFN} (Eq. (7)). Assessment of these parameters is difficult and previous reported estimates, as e.g.
2115　for ρ_{IFN}, vary substantially dependent on the method and system analyzed (Gao et al., 2014; Liao
2116　et al., 2014). We therefore used different parameter combinations of IFNγ production, diffusion
2117　and clearance to test the effect of varying locally confined IFNγ concentrations on the observed
2118　dynamics. Based on the values for production, degradation and diffusion, we can determine an
2119　effective IFNγ perimeter, $r_{IFN}(x)$, given by the radius around the cell membrane up to which an
2120　IFNγ concentration is achieved that would be at least as high as the ED_x, thus leading to a x%-
2121　chance of inhibiting MCMV replication within infected cells within this area (see Eq. (5) and (6)).
2122　The perimeter is determined using the steady-state of Eq. (7). Defining an effective diffusion
2123　coefficient for IFNγ of D_{IFN}^{eff} = 7.81 μm²/h, we adjusted the production and clearance rate to ρ_{IFN} =
2124　25 ng cell⁻¹h⁻¹ and c_{IFN} = 0.15 h⁻¹, respectively, to match our experimental observations **(Table A)**.
2125　With this parameterization, an individual CD4⁺ T cell would have an effective IFNγ perimeter with
2126　a radius of $r_{IFN}(50)$ =10.77 μm, $r_{IFN}(25)$ = 18.97 μm, and $r_{IFN}(10)$ = 29.53 μm for a 50%, 25%
2127　and 10% chance, respectively, in inhibiting MCMV replication. This would correspond to an area
2128　of 364.42 μm², 1130.97 μm² or 2739.47 μm² around the CD4⁺ T cell that would be protected by
2129　IFNγ concentrations that are at least as high as the required ED_{50}, ED_{25}, or ED_{10}, respectively. The
2130　impact of varying values of D_{IFN}^{eff}, ρ_{IFN} and c_{IFN} , and thus, varying effective radii for IFNγ release
2131　on the progression of infection and protection was investigated.

2132

2133　**Effect of IFNγ on viral replication**

2134　IFNγ is assumed to suppress MCMV replication in the infected cells by late gene inhibition and
2135　was previously reported to be dose-dependent and reversible (Kropp et al., 2011; Lucin et al.,
2136　1994; Presti et al., 1998). In our model, the probability to inhibit viral replication in infected cells
2137　depends on the dose response relationship, *g(IFN)*, given in Eq. (6). The individual parameters,
2138　i.e., the maximal efficiency replication inhibition per time step, y_{max}, the ED_{50}, and the Hill-
2139　coefficient *n* that characterize this dose-response relationship were determined using data from
2140　Lucin et al. (Lucin et al., 1994). In their experiments, Lucin et al. (Lucin et al., 1994) pretreated
2141　MEFs with different concentrations of IFNγ for 48h, and determined the percentage of inhibition of
2142　viral load measured in pfu at 4 dpi. Even low concentrations of IFNγ (<1 ng/ml) resulted in a
2143　reduction of replication of approximately 40%, and the effect quickly saturated with a maximum
2144　suppression of <60% at IFNγ concentrations of >5 ng/ml. We fitted

2145
$$f_{inh}(IFN) = 1 - \exp(-g(IFN)48) = 1 - \exp\left(\dfrac{y_{max}}{1 + \left(\dfrac{ED_{50}}{IFN + \epsilon}\right)^n}48\right) \quad (10)$$

2146 to these experimental data, with $f_{inh}(IFN)$ representing the percentage of inhibition dependent on
2147 the concentration of IFNγ, *IFN*, after 48h of treatment. Best fits and 95%-prediction intervals are
2148 shown in **Figure S7g** with best estimates given by y_{max}= 1.76×10^{-2} h^{-1} (1.61×10^{-2}, 2.0 ×10^{-2}),
2149 ED_{50}= 0.41 ng/ml (0.27, 0.77), and *n* = 0.64 (0.51, 0.77) with numbers in brackets indicating 95%-
2150 confidence intervals of parameter estimates (see also **Table A**).

2151

2152 **General system settings**

2153 The grid size, as well as simulated time step sizes had to be chosen in a trade-off between the
2154 required system size, level of detail and simulation duration. As mentioned above, our simulated
2155 grid size covered an area of 800×800 μm^2 with 1 pixel (=lattice site) representing 2 μm in real
2156 space (**Table A**). This increased scaling allows the simulation of areas that are that large while
2157 still being able to determine spatiotemporal dynamics on a cellular level with a reasonable
2158 resolution. In addition, we used periodic boundary conditions and von-Neumann neighborhoods.
2159 Simulations were run based on a time step size of 1 hour. The duration of a MonteCarlo-Simulation
2160 time step (,i.e., MCS-duration), which determines the frequency of copy attempts of the CPM per
2161 simulation time step, was chosen to allow for realistic CD4$^+$ T cell motility dynamics while retaining
2162 feasible simulations times. We used a MCS-duration of 0.0015, which resulted in > 600 MCS per
2163 time step (= 1 h). All simulations were run over 60 days with one run taking around 48 h on the
2164 high-performance computing cluster bwHPC MLS-WiSO. At the start of each simulation to initiate
2165 infection, two actively replicating MCMV infected cells were randomly placed within the simulated
2166 grid. In total, 7 different underlying duct structures were analyzed.

2167

2168 **Parameter fitting and estimation procedures**

2169 Parameter fitting for ODE-models describing the dynamics of intracellular viral replication, CD4$^+$ T
2170 cell influx, and IFNγ efficacy were performed using Maximum-Likelihood approaches based on the
2171 R-packages FME (Soetaert. K.; Petzoldt, 2019), deSolve, as well as the *nls*-function from the
2172 base-package. Parameter identifiability and 95%-confidence intervals of estimates were
2173 determined by profile likelihood analysis (Raue et al., 2009) using the R-package ProfilIroning
2174 (https://github.com/GabelHub/ProfileIroning), or the function *nls.profile* from the base-package
2175 (IFNγ-dose response).
2176 Parameter estimation for individual CD4$^+$ T cell velocity within the CPM was performed using the
2177 FitMultiCell pipeline (https://fitmulticell.gitlab.io), which is based on combining Morpheus with the
2178 computational parallelization and high-performance approach pyABC to automatically adjust
2179 stochastic multi-scale models to experimental data. The pyABC workflow tests multiple parameter
2180 sets in parallel by subsequently minimizing distance measurements between experimental and
2181 simulated data. To this end, each simulation is evaluated using the R-Motilitylab package
2182 (http://www.motilitylab.net) to calculate the mean square displacement, the velocity, straightness

2183 and arrest coefficient of each cell. To account for differences in the measurement scales of these
2184 variables, the coefficient of variance is considered within the fitting procedure by

2185
$$d_i = \frac{(\mu_i - u)^2}{\sigma_i{}^2} + \left(\frac{\sigma_i}{\mu_i} - \frac{s}{u}\right)^2$$

2186 defining the calculated distance for the respective quantity i. Hereby, μ_i and σ_i, are the mean and
2187 standard deviation of the experimental data, and u and s the corresponding values for the
2188 simulated data.
2189
2190
2191 **Data and Code availability**

2192 The individual codes and files describing the model structure to be run in Morpheus are made
2193 publicly available via GitHub (*Github-Link will be added here*).
2194
2195

2196 **Table A:** General systems settings for the cellular Potts models and parameterization of the
2197 individual processes of cellular turnover, intracellular viral replication, viral clearance and diffusion,
2198 as well as CD4$^+$ T cell dynamics and IFNγ-production as used within the different simulations.
2199 Numbers marked with (*), (#) or (†) indicate parameters that were estimated, adjusted or set,
2200 respectively, based on experimental observations and data from the literature. Sources are given
2201 within the text. (¶) indicates values that were determined based on data presented within this
2202 manuscript. Numbers in round-brackets indicate 95%-confidence intervals of estimates.

Parameter	Description	Unit	Value
General systems settings			
	Size of the grid	pixel^2	400 × 400 (1 px = 2 μm)
	Time step duration	h	1
	Duration of a MonteCarlo time step (MCS-duration)		0.0015 = 5.4 s
	Epithelial cell area (uninfected)	μm^2	120.8 (¶)
	Epithelial cell area (infected)	μm^2	241.6 (¶)
	T cell area	μm^2	50 (¶)
Epithelial cell dynamics			
λ	max. proliferation rate of epithelial cells	h^{-1}	0.204 (#)
N_{max}	max. number of epithelial cells	cells	2500 (¶)
p_d	Probability for cell death of uninfected cells		$\sim \Gamma(k_T =40, \theta_T =55)$ (†)
p_δ	Probability for cell death of infected cells		$\sim \Gamma(k_I =0.25, \theta_I =170)$ (†)
Intracellular viral replication			
α_R	viral net-replication rate	h^{-1}	0.41 (*) (0.38, 0.49)

R_{max}	max. carrying capacity of intracellular virus per cell	gen. copy equiv.	1060 [*] (1020,1260)
ρ_R	viral export rate	pfu/ gen. copy equiv. h^{-1}	0.03 [*] (0.02,0.11)
c_R	viral clearance rate (intracell.)	h^{-1}	0.45 [*] (0.20,1.65)
Extracellular viral concentration			
c	viral clearance rate (extracell.)	h^{-1}	0.45 [*] (0.20,1.65)
D_V^{eff}	effective viral diffusion coefficient for the simulations	$\mu m^2\ h^{-1}$	64 [#]
β	Cell-free transmission rate	$pfu^{-1}h^{-1}$	1.5×10^{-3} [#]
CD4$^+$ T cell dynamics			
$\sigma_{in,\ end}$	influx rate of endogen. CD4$^+$ T cells	$\times 10^{-2}\ h^{-1}$	0.17 [*,¶] (0.07, 0.31)
$\sigma_{out,\ end}$	loss rate of endogen. CD4$^+$ T cells	$\times 10^{-2}\ h^{-1}$	0.17 [*,¶] (0.07, 0.31)
$\sigma_{in,\ M25}$	influx rate of M25 CD4$^+$ T cells	$\times 10^{-2}\ h^{-1}$	0.9 [*,¶] (0.40, 0.31)
$\sigma_{out,\ M25}$	loss rate of M25 CD4$^+$ T cells	$\times 10^{-2}\ h^{-1}$	0.9 [*,¶] (0.40, 1.40)
$E_{0,\ end}$	Initial concentration of endogen. CD4$^+$ T cells	cells	960 [*,¶] (510, 2580)
$E_{0,\ M25}$	Initial concentration of M25 CD4$^+$ T cells	cells	20 [*,¶] (10, 460)
s_T	Persistence strength		180 [*]

τ_T	Decay time	min	8.9 [*]
CTX_{APC}	Chemotactic strength to follow CXCL9/CXCL10 gradients		50 [#]
λ_{se}	stimulation rate of end. CD4+ T cells	h^{-1}	0.05 [#]
λ_{sm}	stimulation rate of M25 CD4+ T cells	h^{-1}	0.15 [#]
IFNγ release and efficacy			
y_{max}	max. rate of replication inhibition by	$\times 10^{-2}\,h^{-1}$	1.76 [*] (1.61, 2.0)
ED_{50}	effective dose	ng/ml	0.41 [*] (0.27, 0.77)
n	Hill-coefficient for dose-response relationship		0.64 [*] (0.51, 0.77)
ρ_{IFN}	Production rate of IFNγ	ng h^{-1} cell^{-1}	25 [#]
c_{IFN}	Degradation rate of IFNγ	h^{-1}	0.15 [#]
D_{IFN}^{eff}	effective diffusion coefficient of IFNγ for standard parameterization	$\mu m^2\,h^{-1}$	7.81 [#]
CXCL9/CXCL10 dynamics			
$\rho_{CX9/10}$	Release rate of CXCL9/10	h^{-1}	0.05 [#]
$c_{CX9/10}$	Degradation rate of CXCL9/10	h^{-1}	0.04 [#]
$D_{CX9/10}$	Diffusion coefficient of CXCL9/10	$\mu m^2\,h^{-1}$	8.0 [#]

CTX_{APC}	Chemotactic strength of CD4$^+$ T cells following CXCL9/10 gradient		50 [#]

2203

2204 **Table B:** CD4$^+$ T cell dynamics based as observed on the cross sections of SMG. The observed
2205 cell numbers for endogenous and M25 CD4$^+$T cells at 8 dpi with the determined conversion factor
2206 for the simulated area of 800×800 μm^2, as well as the transformed cell counts at 0, 8, 14 and 30
2207 dpi are shown. The latter were used in the analysis for determining the net-influx and efflux rates
2208 based on Eq. (9) (see also **Figure S7e** and **Table A**). Observations were based on 4 cross
2209 sections with the mean ± SD shown.

Transformation factor of cell counts based on cross section image analyses (n=4) at 8 dpi		
	Endogen. CD4$^+$ T cells	**M25 CD4$^+$ T cells**
Mean cell count (1×1 cm^2)	509.88	10.54
Mean # cells (800×800 μm^2)	326.32	6.74
Mean # cells (SMG, extrapolation)	76501.06	30731.16
Transformation factor	234.43	4557.70
Transformed cell counts for 800×800 μm^2 sections		
Time (dpi)	**Endogen. CD4$^+$ T cells**	**M25 CD4$^+$ T cells**
0	63 (± 29.6)	0 (± 0)
8	223 (± 101.1)	6.4 (± 2.9)
14	386 (± 91.1)	3.48 (± 2.2)
30	357 (± 92.5)	0.3 (± 0.1)

2210
2211
2212
2213
2214
2215
2216
2217
2218
2219

REFERENCES

Aure, M.H., Konieczny, S.F., and Ovitt, C.E. (2015). Salivary gland homeostasis is maintained through acinar cell self-duplication. Dev Cell *33*, 231-237.

Berg, S., Kutra, D., Kroeger, T., Straehle, C.N., Kausler, B.X., Haubold, C., Schiegg, M., Ales, J., Beier, T., Rudy, M*., et al.* (2019). ilastik: interactive machine learning for (bio)image analysis. Nat Methods *16*, 1226-1232.

Dick, J.E., Hilterbrand, A.T., Boika, A., Upton, J.W., and Bard, A.J. (2015). Electrochemical detection of a single cytomegalovirus at an ultramicroelectrode and its antibody anchoring. Proc Natl Acad Sci U S A *112*, 5303-5308.

Fox, J.B., S.; Davisson, M.; Newcomer, C.; Quimby, F.; Smith, A. (2006). The Mouse in Biomedical Research Vol.2 - Diseases (San Diego, United States: Elsevier Science Publishing Co Inc.).

Gao, Y., Zhou, Q., Matharu, Z., Liu, Y., Kwa, T., and Revzin, A. (2014). A mathematical method for extracting cell secretion rate from affinity biosensors continuously monitoring cell activity. Biomicrofluidics *8*, 021501.

Glazier, J.A., and Graner, F. (1993). Simulation of the differential adhesion driven rearrangement of biological cells. Phys Rev E Stat Phys Plasmas Fluids Relat Interdiscip Topics *47*, 2128-2154.

Graner, F., and Glazier, J.A. (1992). Simulation of biological cell sorting using a two-dimensional extended Potts model. Phys Rev Lett *69*, 2013-2016.

Honda, T., Egen, J.G., Lämmermann, T., Kastenmüller, W., Torabi-Parizi, P., and Germain, R.N. (2014). Tuning of antigen sensitivity by T cell receptor-dependent negative feedback controls T cell effector function in inflamed tissues. Immunity *40*, 235-247.

Kropp, K.A., Robertson, K.A., Sing, G., Rodriguez-Martin, S., Blanc, M., Lacaze, P., Hassim, M.F., Khondoker, M.R., Busche, A., Dickinson, P*., et al.* (2011). Reversible inhibition of murine cytomegalovirus replication by gamma interferon (IFN-γ) in primary macrophages involves a primed type I IFN-signaling subnetwork for full establishment of an immediate-early antiviral state. J Virol *85*, 10286-10299.

Kwak, M., Alston, N., and Ghazizadeh, S. (2016). Identification of Stem Cells in the Secretory Complex of Salivary Glands. J Dent Res *95*, 776-783.

Liao, K.L., Bai, X.F., and Friedman, A. (2014). Mathematical modeling of interleukin-27 induction of anti-tumor T cells response. PLoS One *9*, e91844.

Lucin, P., Jonjić, S., Messerle, M., Polić, B., Hengel, H., and Koszinowski, U.H. (1994). Late phase inhibition of murine cytomegalovirus replication by synergistic action of interferon-gamma and tumour necrosis factor. J Gen Virol *75 (Pt 1)*, 101-110.

Marcinowski, L., Lidschreiber, M., Windhager, L., Rieder, M., Bosse, J.B., Rädle, B., Bonfert, T., Györy, I., de Graaf, M., Prazeres da Costa, O*., et al.* (2012). Real-time transcriptional profiling of cellular and viral gene expression during lytic cytomegalovirus infection. PLoS Pathog *8*, e1002908.

2259 Misra, V., Muller, M.T., and Hudson, J.B. (1977). The enumeration of viral genomes in murine
2260 cytomegalovirus-infected cells. Virology *83*, 458-461.

2261 Munger, J., Bajad, S.U., Coller, H.A., Shenk, T., and Rabinowitz, J.D. (2006). Dynamics of the
2262 cellular metabolome during human cytomegalovirus infection. PLoS Pathog *2*, e132.

2263 Presti, R.M., Pollock, J.L., Dal Canto, A.J., O'Guin, A.K., and Virgin, H.W.t. (1998). Interferon
2264 gamma regulates acute and latent murine cytomegalovirus infection and chronic disease of the
2265 great vessels. J Exp Med *188*, 577-588.

2266 Rand, U., Rinas, M., Schwerk, J., Nöhren, G., Linnes, M., Kröger, A., Flossdorf, M., Kály-Kullai,
2267 K., Hauser, H., Höfer, T., and Köster, M. (2012). Multi-layered stochasticity and paracrine signal
2268 propagation shape the type-I interferon response. Mol Syst Biol *8*, 584.

2269 Raue, A., Kreutz, C., Maiwald, T., Bachmann, J., Schilling, M., Klingmüller, U., and Timmer, J.
2270 (2009). Structural and practical identifiability analysis of partially observed dynamical models by
2271 exploiting the profile likelihood. Bioinformatics *25*, 1923-1929.

2272 Schwartz-Arad, D., Arber, L., Arber, N., Zajicek, G., and Michaeli, Y. (1988). The rat parotid
2273 gland--a renewing cell population. J Anat *161*, 143-151.

2274 Soetaert. K.; Petzoldt, T. (2019). FME. http://cran-r-project.org/web/packages/FME/FME.pdf.

2275 Starruss, J., De Back, W., Brusch, L., and Deutsch, A. (2014). Morpheus: a user-friendly
2276 modeling environment for multiscale and multicellular systems biology. Journal of Tissue
2277 Engineering and Regenerative Medicine *8*, 52-52.

2278 Stolp, B., Thelen, F., Ficht, X., Altenburger, L.M., Ruef, N., Inavalli, V., Germann, P., Page, N.,
2279 Moalli, F., Raimondi, A.*, et al.* (2020). Salivary gland macrophages and tissue-resident CD8(+) T
2280 cells cooperate for homeostatic organ surveillance. Sci Immunol *5*.

2281 Verma, S., Weiskopf, D., Gupta, A., McDonald, B., Peters, B., Sette, A., and Benedict, C.A.
2282 (2016). Cytomegalovirus-Specific CD4 T Cells Are Cytolytic and Mediate Vaccine Protection. J
2283 Virol *90*, 650-658.

2284 Walton, S.M., Mandaric, S., Torti, N., Zimmermann, A., Hengel, H., and Oxenius, A. (2011).
2285 Absence of cross-presenting cells in the salivary gland and viral immune evasion confine
2286 cytomegalovirus immune control to effector CD4 T cells. PLoS Pathog *7*, e1002214.

2287 Wirtz, N., Schader, S.I., Holtappels, R., Simon, C.O., Lemmermann, N.A., Reddehase, M.J., and
2288 Podlech, J. (2008). Polyclonal cytomegalovirus-specific antibodies not only prevent virus
2289 dissemination from the portal of entry but also inhibit focal virus spread within target tissues.
2290 Med Microbiol Immunol *197*, 151-158.

2291

2292